BLAST RESPONSE AND SENSITIVITY ANALYSIS OF SEGMENTAL TUNNEL

By

Sivalingam Koneshwaran

BSc Eng (Hons,1)

A THESIS SUBMITTED TO

FACULTY OF SCIENCE AND ENGINEERING FACULTY

QUEENSLAND UNIVERSITY OF TECHNOLOGY

IN PARTIAL

FULFILMENT OF THE REQUIREMENTS FOR THE DEGREE OF

DOCTOR OF PHILOSOPHY

November 2014

Dedicated to my parents, family and friends

Acknowledgements

I wish to express my deepest gratitude to my principal supervisor, Professor David Thambiratnam, for his excellent guidance, caring, patience, and rightful leniency throughout my doctoral studies. I also want to thank my associate supervisor Dr. Chaminda Gallage for taking the time to review my work and for providing me with valuable technical observations.

My sincere thanks also goes to Mr. Ashley Wright and other staff members at the High Performance Computer and Research Support Group for providing technical assistance with numerical simulations and data manipulation. I wish to extend my thanks to Dr. Luke Mosse, of Livermore Software Technology Corporation who provided immeasurable assistance on the working of the Finite element software LS-DYNA. I also wish to thanks to Associate Professor Anirban De, Manhattan College, USA and Dr. Arulmoli, Principal of Earth Mechanics, Inc., Canada for providing extensive experimental data set for validating the modelling techniques.

I gratefully acknowledge the financial support granted by Australian Postgraduate Award and Science and Engineering Faculty, Queensland University of Technology (QUT) to conduct the research. I am very grateful to my colleagues at QUT for sharing their knowledge, valuable guidance and encouragement in carrying out the research.

Finally, I am extremely grateful to my parents and wife who have been a source of encouragement and inspiration throughout my career.

Sivalingam Koneshwaran
Science and Engineering faculty,
Queensland University of Technology,
Brisbane, Australia.
November 2014

TABLE OF CONTENTS

LIST OF FIGURES

LIST OF TABLES

Abstract

Increasing threat of terrorism highlights the importance of enhancing the resilience of infrastructure to all types of hazards. A significant amount of studies have been carried out to scientifically develop appropriate protective measures for above ground structures such as buildings and bridges to mitigate the adverse effects of terrorist attacks. However, only a few studies have been carried out on underground transportation tunnels which are equally or even more important in the infrastructure. Bored tunnels driven by tunnel boring machines (TBM) are now common in many cities providing a quick and cost effective alternative to surface rails and roads. Although a few studies have been carried out on underground tunnels subjected to surface blasts, they do not cover bored tunnels which consist of prefabricated reinforced concrete segments placed together by bolted joints.

In this research field, full-scale tests are often impractical as it is extremely risky and expensive. Although few studies have been conducted using scale-down centrifuge tests to investigate the blast response of pipe structures, limitation in the centrifuge test makes it virtually impossible for investigating the blast response of bored tunnel with multiple bolted joints which are essential to resist the blast load by allowing the joints to rotate, slide and dissipate energy to achieve equilibrium before the segments are damaged. The possible alternative, therefore, is to use numerical techniques which can provide valuable data in a timely and cost effective manner to enable the development of mitigation measures.

This research develops and applies a fully coupled technique to study the response of bored tunnels to credible surface blasts using explicit dynamic nonlinear finite element software LS-DYNA. Appropriate material models were utilized with strain rate effects in the analyses. Damage states of tunnels were identified based on the displacements, drifting responses between segments and cracks in the segments. The influence of soil type, joint type and number of segments forming the tunnel ring has been investigated. Results show that the tunnel buried in saturated soil displayed severe damage compared to that buried in partially saturated or dry soils. For weaker blast loads, joint types influenced the tunnel response by allowing the segments to

rotate about the joints, whereas for higher blast loads, the segments were damaged before activating the flexibility of the joints. Although an increase in the number of segments increases the number of joints, beyond a certain limit, increase in the number of segments did not improve the blast performance of the tunnel. The tunnel is more vulnerable to surface explosions which occur directly above the centre of the tunnel than those that occur at any equivalent scale distances by moving the explosive away from the tunnel centre.

The finding from this research offer significant new information on the blast performance of segmented bored tunnels and will guide their future implementation in civil engineering applications.

Key words

Blast analysis, Surface explosion, Segments, Bored tunnel, Joints, Soil, Finite element method, Fully coupled analysis, Numerical simulation, Material models, cracks, Soil-Structure Interaction.

Publications

International Journal Papers

- Sivalingam, K., Thambiratnam, D. P., and Gallage, C (2014), "Numerical Performance of buried tunnels subjected to surface blast incorporating fluid structure interaction". *ASCE Journal of Performance of Constructed Facilities*. **Published**
- Sivalingam, K., Thambiratnam, D. P., and Gallage, C (2014), "Response of Segmented Bored Transit Tunnels to Surface Blast". *Engineering Structures, Elsevier*. **Submitted in July 2014**
- Sivalingam, K., Thambiratnam, D. P., and Gallage, C (2014), "Blast Response and Failure Analysis of Segmented Bored Tunnel using Coupled SPH-FE Method". *Computers and Structures, Elsevier*. **Under review**
- Sivalingam, K., Thambiratnam, D. P., and Gallage, C (2014), "Effects of Segments on the Blast Response of Buried Tunnels". *ASCE Journal of Structural Engineering*. **Under review**

International Conference Papers

- Sivalingam, K., Thambiratnam, D. P., and Gallage, C (2013), "Response of a Buried Tunnel to Surface Blast using Different Numerical Techniques". *Proceedings of the Fourteenth International Conference on Civil, Structural and Environmental Engineering Computing: Civil-Comp Press, Stirlingshire, UK*. **Published**

Statement of original authorship

The work contained in this thesis has not been previously submitted to meet requirements for an award at this or any other higher education institution. To the best of my knowledge and belief, the thesis contains no material previously published or written by another person except where due reference is made.

QUT Verified Signature

Koneshwaran Sivalingam

November 2014

Chapter 1: Introduction

1.1 BACKGROUND

Underground transit tunnel system provides a quick and cost effective alternative to laying surface rails and roads. This system plays an important role in addressing transportation needs in many cities. Terrorist attacks, such as the Belarus bombing in 2011, the Moscow metro bombing in 2004 and the London subway bombing in 2005, highlight that underground transit tunnels are vulnerable to potential terrorist attacks. According to University of Maryland Global Terrorism Database in Figure 1.1 the terrorist attacks on tunnels continue to increase and explosive is the main source for those attacks over the past four decades. The Department of Homeland Security of the United States also issued a statement that terrorists may attack New York subway system using explosive.

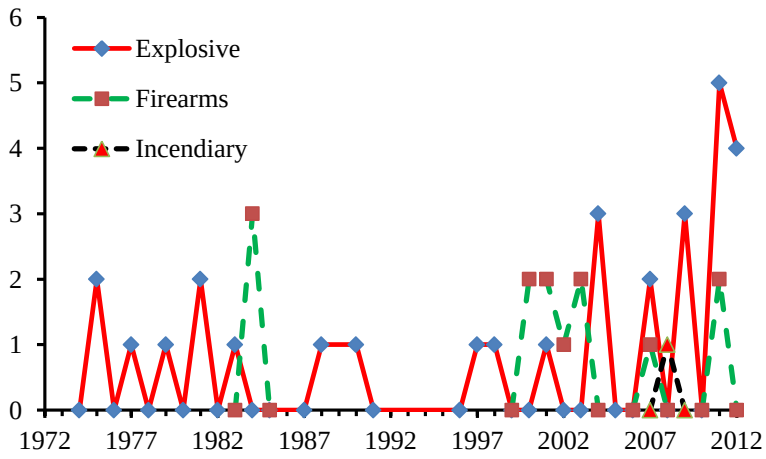

Figure 1.1: Comparison of types of terrorist attacks on tunnel (GTD, 2013)

Terrorist attacks on transportation tunnels must therefore be closely considered for two reasons; i) the importance and centrality of such infrastructure, and ii) the level of public use. The failure of such underground tunnels would not only cause delays and transport network interruptions, but also result in severe loss of lives with considerable financial implications.

The central part of a rapid transit network in cities is usually within tunnels. These tunnels are mostly bored tunnels constructed using tunnel boring machines (TBM) with the support of permanent linings. The principle of bored tunnel construction has been known for a long time. Tunnels constructed in the beginning of the nineteenth century are still in use in many cities. They have a direct relationship with the identity of the city as they illustrate its history, culture, and its economic, political and social states. Some tunnels are designed to resist natural disasters such as earthquakes and extreme events such as fires, but most are not designed to resist blast loading. This demands great attention for protecting such structures from terrorist attacks.

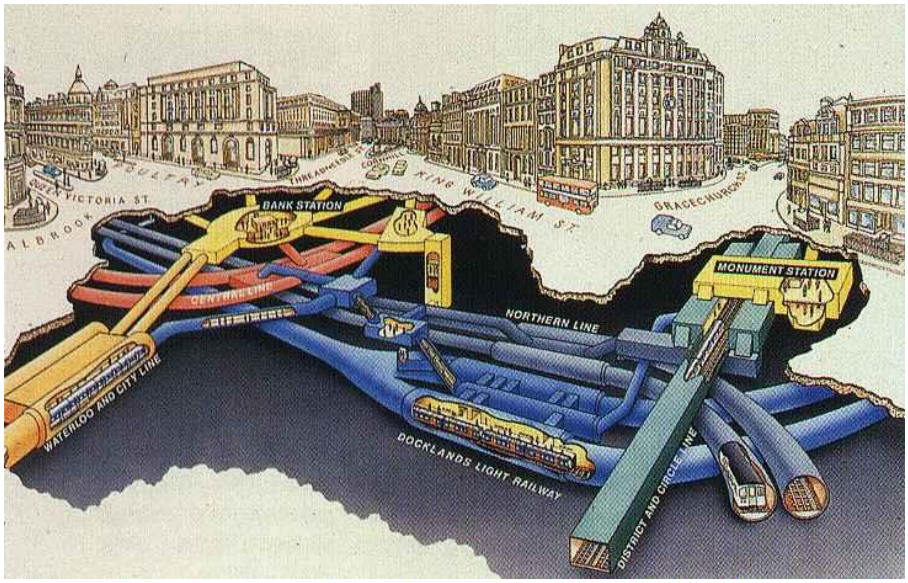

Figure 1.2: Schematic view of London underground transit tunnels (Skyscrapercity.com, 2013)

Tunnel structures may experience either internal or external blasts. Internal blasts are less likely to occur as it is difficult to place an explosive device within a tunnel as well as having a moving vehicle filled with explosives is not feasible in subway systems. Advanced security and surveillance systems installed in the subway can also easily detect such interior explosive devices. However, external blasts are unfortunately more likely and have the potential to cause most damage. For example, Figure 1.2 shows a schematic view of a part of London underground transit network. The congestion shown in this picture is indicative of the situation in many cities worldwide. The picture illustrates that the tunnels are shallow and such shallow tunnels are vulnerable to external explosion from a moving vehicle having potential sources of ignition.

Furthermore, the crowded nature of underground developments increase risk to both underground and above ground structures in the vicinity.

A Vehicle Borne Improvised Explosive Device (VBIED) is commonly used as a weapon of terrorism to damage constructed facilities. As shown in Table 1.1, VBIED can be carried in a wide range of vehicles such as cars, vans, containers and trailers to transport a large amount of explosive without attracting suspicion. As the VBIED is relatively close to the ground surface, the explosion from the VBIED generates air-blast pressure as well as ground shock.

Table 1.1: Weight of explosive (TNT equivalent) filling a vehicle (Conterterrorism 2014 Calendar, 2014)

Type of vehicles	Vehicle description	Explosives capacity TNT* Equivalent (kg)
	Sedan	227
	SUV/van	454
	Small delivery truck	1814
	Container/water truck	4536
	Semi-trailer	27216

* Section 2.2.2 describes TNT (Trinitrotoluene).

Ground shocks travel through both soil and rock. In soil, the tunnel structure resists most of the ground shock, whereas in rock, the medium itself carries a large amount of the ground shock. As the shock wave intercepts the geostatic soil structure interface between the tunnel structure and surrounding soil, the tunnel experiences an effect of inertia lasting for a few milliseconds. The surrounding medium significantly constrains the tunnel motion. However, the tunnel response to the shock wave is similar to

instantaneous vibration as damping from the surrounding medium is ineffective. The shock wave reaches the tunnel in a very short time before the damping activates itself (Shin et al., 2011). The tunnel can therefore exhibit excessive level of stress affecting the structural integrity. This leads to a localized failure and potential collapse of the tunnel with serious consequences.

Bored tunnels with segmented tunnel lining are more popular in underground railway systems. The tunnel lining is installed directly behind the TBM. The space between the bored soil/rock face and the lining is filled with annular concrete grout. The lining consists of prefabricated reinforced concrete segments placed together to complete one lining ring to span the circumference of the tunnel as shown in Figure 1.3. The segments are connected to adjacent segments at contact joints by bolts which create an interlocking system providing the tunnel with resistance against external pressure from the surrounding ground. The stiffness of the joints determines the load transmission throughout the ring. The joints in both radial and circumferential directions consist of grooves to accommodate the elastomeric gasket that provides water-resistance. The bolts help stabilise the ring during the grouting as well as ensure the water-resistance by compressing the gasket in the years of service after construction.

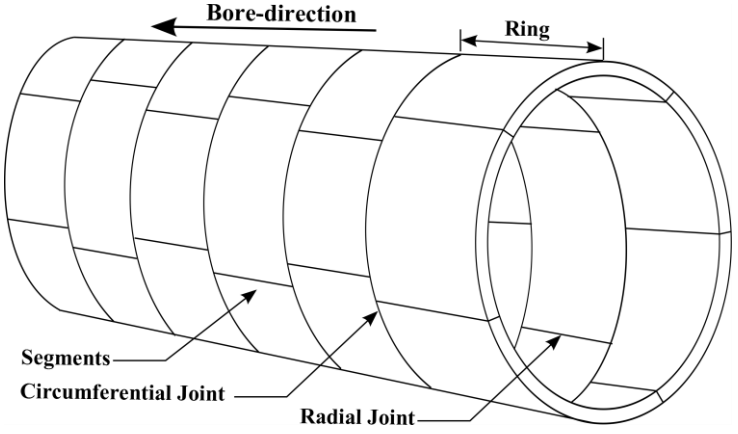

Figure 1.3: Schematic view of Precast Segmented Rings

In order to ensure the safety and stability of bored tunnels, it is necessary to consider the variability in the prediction of load carrying capacity during their service life. The four key factors which affect the tunnel response under blast loading are: (i) surrounding ground type (ii) explosive mass, (iii) standoff distance and (iv) lining stiffness. Though

the lining stiffness is the engineer's choice, it may be difficult to evaluate how the tunnel response is influenced by its stiffness. The response of the segmented tunnel lining to the blast loading is more complex than other loadings such as geo-static and earthquake loadings. Performance of the segmented tunnels under static and earthquake loads has been the subject of several studies. However, there is inadequate information on response of bored tunnels to blast loading. Munfah (2009) described that thin precast segmented tunnel linings are more vulnerable to blast loads than thick cast-in-place concrete tunnels. It is therefore of interest to investigate the vulnerability of segmented tunnels to credible blast loading.

In this research field, there are no records on full-scale prototype field experiments investigating the tunnel response to surface blast. Full-scale experiments are extremely risky and unattainable in civilian research as they involve the use of a large quantity of explosives. On the other hand, significant studies have been conducted using scaled-down centrifuge modelling techniques to treat the blast response of buried cylindrical structures. However, limitations in the centrifuge test makes it virtually impossible for investigating the blast response of bored tunnel with multiple bolted joints which are essential to resist the blast load by allowing the joints to rotate, slide and dissipate energy to achieve equilibrium before the segments are damaged. The possible alternative, therefore, is to use numerical techniques which can provide valuable data in a timely and cost effective manner to enable the development of mitigation measures.

1.2 RESEARCH PROBLEM

The primary load resisted by the tunnel is through the combination of circumferential (hoop) stress and bending stress induced by external pressure from the surrounding ground acting on the circumference of the tunnel. The external pressure is mostly a non-uniformly distributed pressure, and not a concentrated load. The VBIED-induced shockwave applying pressure on the tunnel surface is however more complex. Figure 1.4 illustrates how VBIED induced shockwave propagates through the soil surrounding a tunnel structure. When the expanding shockwave front strikes the tunnel surface as shown in Figure 1.4(b), it exerts a dynamic concentrated load. As the shockwave progresses, it applies a distributed load. Meanwhile, the shockwave is reflected from the tunnel surface and the reflected wave diminishes the intensity of oncoming incident

wave. If the tunnel is closer to the explosive, the reflected wave becomes more significant, and peak reflected pressure appears to be higher than the oncoming incident wave pressure. At this point, it generates a negative pressure on the tunnel surface.

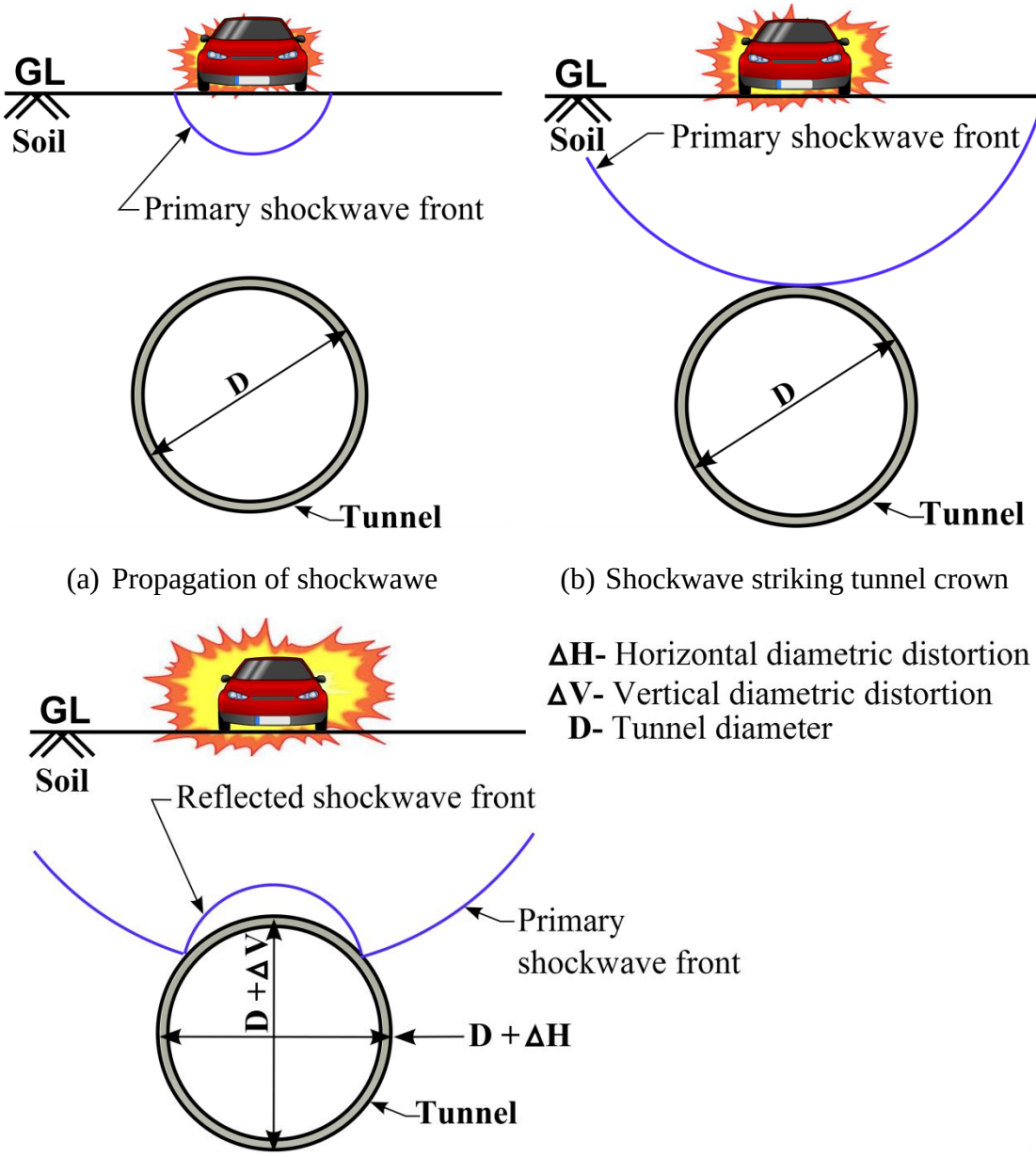

(a) Propagation of shockwawe (b) Shockwave striking tunnel crown

(c) Reflection of shockwave

Figure 1.4: Interaction of shockwave with the tunnel

As the surrounding pressure changes through a concentrated load, distributed positive and negative pressures, the tunnel lining experiences diametric distortions in all directions. In such situations, the tunnel lining applies its flexibility to deform and interact with the surrounding medium to resist the shockwave. The lining segments are

generally designed to resist the axial bearing loads and buckling from the TBM thrust loads as well as bending stresses from the surrounding soil pressure. Under geostatic loading, the segmental linings permit a degree of rotation at the joints without significant loss of load carrying capacity. However, the potential damage due to ground shock resulting from the blast has not received proper attention in the current practice of tunnel designing, particularly transit tunnels with very thin segmented linings and joints, which are at risk of terrorist attacks. Lack of knowledge on analysing the tunnel performance to blast load impedes the progress of the study in this area. This emphasises the need for research to evaluate the blast performance and vulnerability of the segmented bored tunnel.

1.3 AIMS AND OBJECTIVES

The main aim of this research is to study the response of bored tunnel (subway) to credible surface blast as well as to study the effects of controlling parameters. This research will examine the vulnerability of bored tunnel with precast segmented lining under different blast scenarios. In order to achieve this, the specific objectives of the present study are as follows:

- To develop fully coupled numerical models incorporating different material models to study the effects of bored tunnel with segments subjected to surface blast loading.
- To provide validation of the proposed modelling techniques using available experimental results.
- To conduct parametric studies on the influence of soil type, segment geometry, joint type and number of segments in a ring on the blast response.
- To provide mitigation measures to protect the tunnel from credible surface blasts.
- To develop design information that can be used as a reference to check the blast capacity and vulnerability of a tunnel.

1.4 SIGNIFICANCE OF THE RESEARCH

Terrorist attacks are not limited to government and military structures. Terrorists have expanded their attacks with an intention to cause heavy human casualties and economic losses to common and crowded public facilities such as transportation structures, shopping malls and office buildings. A significant number of appropriate protective measures have been put in place to protect above ground structures against blast loading. However, there is no design guidance available to mitigate the adverse blast effects on bored tunnels with segmented joints. This highlights a need to develop appropriate guidance and recommendation for design of newly built bored tunnels to provide safety to both passengers and structure. It is also expected that this research will develop design information for strengthening typical existing bored tunnels.

This research will develop and apply fully coupled numerical techniques incorporating Fluid Structure Interaction (FSI) and using Arbitrary Lagrangian-Eulerian (ALE) techniques. It provides new information on the influence of important parameters such as soil types, geometrical shape of segments, joint types and numbers of segments in a ring. The study is further extended to evaluate mitigation measures in order to reduce the blast impact on the tunnel response. In general, this research is intentionally carried out on a common single tube railway tunnel system subjected to credible surface blast from Vehicle Borne Improvised Explosive Device (VBIED).

1.5 THESIS OUTLINE

The present thesis on "Blast Response and Sensitivity Analysis of Segmental Tunnel" consists of eight chapters, including introduction (Chapter 1) and conclusion (Chapter 8). Each chapter covers one particular theme of study in the research. The outline of this thesis is organized as follows.

- In Chapter 2, a comprehensive literature review of blast loads and resulting wave propagation through soil, soil-structure interaction and tunnel response under blast loads are presented.
- Chapter 3 describes the basic principles of numerical techniques, including different types of spatial discretisation solvers, Arbitrary Lagrangian-Eulerian

(ALE) techniques and Smooth Particle Hydrodynamics (SPH) techniques as well as suitable material models adopted in this study.

- Chapter 4 discusses in detail the existing experimental records used to validate the numerical techniques used in this study. It then describes the validation of the fully coupled numerical models.
- The developed numerical techniques are applied in Chapter 4 to investigate the blast response of segmented bored tunnel by varying the geometry of segments in Chapter 5.
- Chapter 6 describes crucial parameters affecting the blast response of segmented tunnel in soft soils. The effect of soil properties on the tunnel response under surface explosion and the influence of tunnel flexibility by varying geometric properties of the tunnel lining are discussed in this chapter.
- Chapter 7 presents the results of a parametric study to evaluate the performance of a segmented tunnel by introducing different types of protective barriers, segment materials and energy absorbing pads between segments to mitigate the blast effects.
- Finally, Chapter 8 summarises and discusses the main findings of this research and presents practical implications, and recommendation for future work.

Chapter 2: Literature Review

2.1 INTRODUCTION

This chapter explores the current knowledge on explosion, shockwave propagation in soil, soil-structure interaction (SSI) and the response of buried tunnels to ground shock.

2.2 EXPLOSION AND RELATED PHENOMENON

An explosive is a chemical compound or a complex mixture that explodes due to either a rapid chemical reaction or electric sparks or flame. As a result, the surrounding environment experiences an increase in volume of the explosive gas and release of energy in an extreme manner. During the explosion in both the air and the ground, a shock wave composed of a high pressure wave front expands violently from the centre of the detonation with pressure intensity decaying with distance and time.

2.2.1 Explosives and TNT equivalent

The characteristics of blast loading are determined by many factors such as charge weight, stand-off distance and type of explosive. There are many types of explosive, but not all kinds of explosives release the same amount of blast energy. As a result, the TNT (Trinitrotoluene) equivalent is introduced as an "Explosive Bench Mark" for quantifying the energy released in explosions. The "a ton of TNT" is a unit of energy equal to 4.184GJ, which is nearly the amount of energy generated in the explosion of the one ton of TNT. Each explosive material has a unique TNT equivalent value which depends on several factors such as detonation rate, effectiveness, and amount of energy released. This definition is essential, for instance, when placing limits in blast load investigations. Table 2.1 illustrates the TNT equivalent of common explosives materials.

Table 2.1: TNT equivalent of common explosives materials (Jayasooriya et al., 2011)

Explosive	TNT Equivalent
ANFO	0.82
Composition A-3	1.09
Composition B	1.1-1.2
Composition C-4	1.37
Cyclotol (70/30)	1.14
HBX-1	1.17
HBX-3	1.14
HMX	1.3
H-6	1.38
Minol II	1.2
Nitro-glycerine	1.5
Octol(70/30)	1.06
PBX-9010	1.29
PETN	1.27
Pentolite	1.38-1.5
Picratol	0.9
RDX	1.2
Tetryt1	1.07
TNETB	1.36
TNT (Trinitrotoluene)	1
TRITONAL	1.07

2.2.2 Blast scaling laws

The Hopkinson-Cranz scaling law, or cube-root scaling, is the most common form of scaling to describe blast wave characteristics (Cooper & Kurowski, 1996). This states that similar explosive waves are generated at identical scaled distances when two explosive charges of similar geometry and type are detonated in the same atmosphere. In the Hopkinson-Cranz law, the scaled distance Z is described as a function of the charge weight of explosive in terms of TNT equivalent (W) and the distance R from the centre of the charge (stand-off distance) , given by Equation 2.1.

$$Z = \frac{R}{W^{\frac{1}{3}}}$$ Equation 2.1

The scaling factor *Z* allows a compact and efficient representation of shock wave data for a wide range of air-blast situations. De (2012) used the scaling law to investigate the response of buried tunnel subjected to surface explosion over dry sand. For buried explosion, Yankelevsky et al. (2011) found that a relatively loose sand with a considerable high volumetric strain potential well describes the scaling law, but saturated clays with a relatively low volumetric strain potential showed a large discrepancy in the results. Lee (2006) also describes the limitation of this approach for buried explosion in saturated soils as both water and soil transmit the shock wave at significantly greater rates with greater shock impedance and less compressibility than in air.

2.3 SHOCK WAVE PROPAGATION

A ground shock occurs due to the sudden release of energy from an explosion at or near the ground surface. The ground shock is produced in two primary ways, each of which sets the ground in motion. Firstly, air-induced ground shock occurs if the energy is transmitted through the air and it runs over the ground surface. Secondly, direct-induced ground shock results from the energy transmission process due to the direct coupling of blast energy around formation of crater.

The air-induced ground shock results from an explosion occurring in free-air high above ground surface where the blast waves propagate radially with a spherical wave front from the charge centre. The shock waves primarily compress the ground and transmit a stress pulse into the ground. The intensity of the motion is typically downward with a peak at the ground surface (Joint Departments of the Army, the Navy and the Air Force, 1990). Procházka et al. (2008) found that the contact explosions on the soil surface transfer up to 30% of the total blast energy into the ground.

Direct-induced ground shock resulting from the surface explosion creates a direct-induced motion as well as cratering-induced motion. The ground-induced ground shock is more important in underground engineering as the direct-induced shock has more

effect in terms of intensity and duration of the shock wave than the air-induced ground shock. The intensity and duration of the ground shock primarily depends on soil properties such as density and degree of water saturation (Zhongqi et al., 2004). However, the effect of atmospheric moisture in the air-blast pressure is considered to be small (Glasstone & Dolan, 1977). The blast orientation largely influences the degree of blast energy imparted to the ground during the direct-induced motion. The Alekseenko test described that the proportion of blast energy imparted to the air and the ground was around 53% and 47% respectively when an explosive was buried in such a way that its upper surface was at the same level as the ground surface (Yang et al., 2010). On the other hand, explosion from deep buried charges produce greater effects on the buried structures in magnitude and are much longer in duration than the corresponding blast in the air (Department of the Army, 1986).

The ground shock generally produces primary waves (P-waves), shear waves (S-waves) and surface waves. P-waves involve compression and dilation in the same direction as the waves progresses through the ground. They are rich in blast induced ground shock (Kramer, 1996). S-waves propagate through the ground by causing particles to move perpendicular to the direction of the waves. P-waves travel faster than the other wave types. Seismic velocities of S and P waves assist in the estimation and prediction of the properties of the subsurface soil materials. Kramer (1996) provides additional insights on the evaluation of soil properties based on the seismic velocities.

2.4 CRATER FORMATION

The mechanism of crater formation depends on the explosive mass and the height or depth of the detonation centre with respect to the ground surface. If the explosion is well above the surface, it creates a conical-shaped crater in the ground. For buried explosions, gravitational effects govern the crater mechanism. As the depth increases, larger amounts of overburden subsoil need to be disintegrated and ejected outwards. This result in increase of crater size to a certain depth, from which the crater size decreases, or in other word, no crater formation is observed on the ground (Bull & Woodford, 1998). This is where a cavity is formed.

The theory of the crater formation has been discussed in the literature (Ambrosini et al., 2004; Ambrosini & Luccioni, 2005; Kinney & Graham, 1985; Luccioni et al., 2009). Ambrosini and Luccioni (2005) conducted a series of experiments to derive empirical relationships between the depth and the diameter of the crater for surface explosions. It showed that an insignificant variation of 5% accounts for the differences between the soil properties. This suggests that the crater formation study may not be adequate to investigate and differentiate the blast effects on different types of soils.

2.5 SOIL-STRUCTURE INTERACTION (SSI)

The interaction between a structure and the surrounding soil has been of technical interest for many years. This aspect, however, is not a simple problem due to the complex effects on interaction between the soil and the structure. This indeterminacy arises from the process in which the response of the soil affects the structural motion as well as the structural motion affects the soil response. In other words, structural deformation influences the distribution and magnitude of the surrounding earth pressure at the soil-structure interface.

In the past, designers ignored the SSI effects in designing buried structures to dynamic loading with a conservative simplification that the SSI has a beneficial effect on the structural response. As a result, simplified free-field deformation methods have conventionally been considered (Wang, 1993). However, the assumption is not always true and the SSI causes detrimental effects on the structural response. With the introduction of advance numerical techniques, drawbacks associated with the free-field deformation methods are eliminated by considering the SSI effects (Xu & Liu, 2008).

The nature of the SSI effect on buried structures varies with the confining stress field. If the stress due to the surrounding load has a significant inertia effect, then the structural response would be transient. This is called dynamic SSI. The transient phase continues for a few milliseconds during an explosion-induced ground shock, but the duration is relatively long for earthquake excitation. Apart from the loading, factors such as (i) structural material, size and stiffness; (ii) surrounding soil, and (iii) construction method (example, bored tunnel, mined tunnel and cut-cover-tunnel), affect the SSI.

Krauthammer and Chen (1989) indicated that the introduction of interface model between the structure and the surrounding soil had a significant effect on the response of buried structures. Sandford (2000) further described that the buried structures cannot resist the external loads, including surrounding soil, without utilizing the strength of the soil in an extreme situation. Overall, the literature survey reveals that the SSI effect is an essential aspect in the tunnel-soil interaction under blast loads.

2.6 BLAST RESPONSE OF BURIED TUNNELS

In the past decades, a series of experiments and numerical simulations have been conducted to investigate the consequences of explosion on super structures, such as buildings and bridges. Nevertheless, blast response of buried transportation structures is still the subject of investigation. In this field, there are no records of information on field prototype experiments in the literature as full-scale field tests are limited by constraints of cost, risk and time. A few recent and current studies however used scaled-down centrifuge modelling techniques to investigate the blast response of tunnels.

2.6.1 Experimental approach

When reliable real-time field data are difficult to obtain, centrifuge modelling is beneficial for scale modelling of large-scale nonlinear problems in geotechnical engineering. A number of researchers (Davies, 1994; Davies & Williams, 1992; De, 2012; De et al., 2013; Kutter et al., 1988; Whittaker, 1987) have successfully implemented the centrifuge modelling to simulate the blast response of buried structures. De (2012) and De et al. (2013) conducted a series of centrifuge tests to study the surface blast effect on cylindrical structure buried in dry sand. These experiments provide quantitative information on the effects of surface explosion on the buried tunnels. Due to varying gravitational field in the test bucket, the centrifuge models are limited to smaller models which may not be adequate to predict the blast response of bolted joints in the segmental lining of bored tunnels. On a small scale, Hayes (1989) conducted a Conventional Weapon Effects Backfill (CONWEB) test series to investigate the blast response of buried reinforced concrete structures with differing backfills. This study used a small model of a reinforced concrete slab bolted to a reaction structure to study its blast response.

2.6.2 Numerical approach

Since the advent of super computers, explicit dynamic nonlinear finite element approaches provide an alternative technique to solve a broad range of blast problems. These techniques allow the quality and quantity of blast simulations to be increased in an affordable and time-efficient manner. Yang et al. (2010) conducted a numerical simulation of the blast response of a metro tunnel in Shanghai using an advanced general purpose multi-physics simulation software LS-DYNA (LSTC, 2007). They used Arbitrary Lagrangian-Eulerian (ALE) method where Eulerian meshes were used for air, soil and explosive while Lagrangian mesh was employed for the tunnel. Merged nodes at the interface of the two parts facilitated the stress transfer between the soil and the tunnel. Feldgun et al. (2008) investigated the soil-structure separation of a buried tunnel subjected to internal explosion. The comparison of analysis with and without soil-structural separation shows a significant variation in the tunnel response. Olarewaju (2012 (a), 2012 (b), 2013) describes a recent series of numerical studies that had been carried out on buried pipes to investigate the pipe response due to accidental explosions using the commercial Finite Element program ABAQUS. In this study, the interaction between the soil and pipe was simulated by perfectly bonded 'no slip' condition which may be appropriate for small pipe structures as the pipe deforms with soil, in which the separation and sliding effects of the interface are negligible. However, for larger tunnel structures, it is vital to incorporate the contact model that allows separation, recontact and sliding.

Olarewaju (2012 (a), 2012 (b), 2013) simplified the soil and pipe materials to be linear, homogeneous and isotropic. This assumption may be valid for far field blast and subsequent structural response, but the behaviour of soil and resistance of pipe material under blast loading are highly nonlinear. In addition, the material models should include strain rate effects.

Morris et al. (2004) studied the blast response of buried structures using distinct element method (DEM). This study simulated a rock excavated lined tunnel and compared the results with experimental data. Although the predicted peak velocities and dispalcements are reasonable, this study was unable to provide complete damage. Gui

and Chien (2006) investigated a bored tunnel passing beneath Taipei Shongsan airport under buried explosion. Their model employed the Finite Difference software FLAC^{2D} with a simplification of three dimensional (3D) blast wave into a two dimensional (2D) blast wave. It was a conservative approach, though it considerably minimized the computation cost. The model also simulated the soil-tunnel interface with static and dynamic frictions in order to permit sliding. Liu (2009; 2012) investigated the dynamic response of subway tunnels subjected to internal blast using the computer code ABAQUS, where the cast iron tunnel was modelled as a shell structure, assuming a triangular blast pressure on the internal surface of the tunnel. Although the focus of the study was on the SSI and stiffness of the lining, the simulation did not consider the important aspects of air-structure interaction, a 3D blast effect and direct heat effect from the internal blast. The heat effect may not be very important to the buried tunnels subjected to surface blast as the surrounding soil medium will act as a good heat insulation material. When an explosive detonates in contact with the ground, the blast waves propagate hemispherically in the ground and affect the performance of structures in all directions. This emphasizes the need for 3D analysis in order to simulate a more realistic problem (Higgins, 2011). The 3D analysis requires considerable computational time and large memory. Application of an effective modelling technique greatly reduces the computation time and memory.

Using the centrifuge test results, De (2012) validated his numerical model developed from AUTODYN. Eulerian meshes were used to model the air and explosive while the soil and the copper-tunnel were modelled with Lagrangian meshes. Penalty based interaction 'Lagrange-Lagrange' method simulated the interface between the soil and tunnel. He utilised a default sand model based on Laine and Sandvik (2001). The material model simulates the strain rate behaviour of sand (Higgins et al., 2012). Soil moisture content has a significant influence on the response of buried structures under blast loads. To date, no one has studied the effects of pore water pressure in the soil on the blast response of underground tunnels. De (2012) also highlighted the need for soil models to incorporate pore water effects.

The studies performed to date have ignored the important aspect of the tunnel joints. Munfah (2009) also indicated that the precast segmental lining is more vulnerable to blast than thick cast-in-place tunnels.

2.7 RESEARCH GAP

In recent years a number of researchers have performed analyses using various finite element hydrocodes with implementation of various constitutive material models to simulate a variety of blast related problems. Although blast performance of above ground structures like buildings and bridges has gained increasing interest, less attention has been paid to the blast performance of buried structures with a common belief that buried structures are much safer than aboveground structures. In fact, it is necessary to consider the critical factors, such as intensity of shockwave, flexibility of structure and the surrounding ground that influence the vulnerability of buried structures to blast loading.

An underground transit tunnel is a critical piece of infrastructure as a large number of people use it. Some of them are designed to resist natural disasters such as earthquakes and fires, but most tunnels are not designed to resist credible explosions. As stated previously, there are no records in the open literature regarding the blast performance of segmental tunnel lining (bored tunnel by TBM) with multiple bolted joints. These joints are semi-rigid joints assisting the segments to transfer loads to neighbouring segments by allowing rotation without reducing the load carrying capacity under geostatic loading. The influence of the joints on the tunnel response to surface blast is hence less understood. Since there is no comprehensive guidance to evaluate the performance of segmental tunnel subjected to surface blast, a detail investigation is required. This research will address the knowledge gaps identified above.

The literature review revealed that numerical modelling technique can be utilized to provide valuable data in a timely and cost effective manner to predict the blast performance of segmental tunnel. The next chapter describes the finite element modelling technique used in the present research.

Chapter 3: Numerical Modelling

3.1 INTRODUCTION

Hydrocodes are the computational tools that can be used to solve a wide range of non-linear problems in solid, fluid flow and explosions. There are several numerical techniques available in hydrocodes, but selection of an appropriate numerical technique is wholly dependent on the type of problem and computational cost. The numerical techniques described in this section evaluate the appropriate techniques and to expand the state of the art in surface blast response of underground tunnels. The general purpose finite element hydrocode LS-DYNA (LSTC, 2007) is employed for this numerical simulation. This chapter describes the theory behind the numerical technique and various constitutive material models used in this study.

The numerical simulations divide a system into finite elements, a process called discretisation. The discretisation takes place with respect to time (temporal) and space (spatial). In numerical simulations, temporal discretisation uses the explicit method which calculates the state of a system at a later time as a function of time step from the current state of the system. In order to capture any activity within an element, the time step should satisfy the Courant-Friedrich-Levy (CFL) condition for which the time step (Δt) is less than the duration for sound to cross the smallest element. Usually, it is advised to use a Safety Factor (SF) of 0.67 for blast loads in LS-DYNA, which could be different for other computer software. This condition can be generally expressed as below:

$$0 < \Delta t \leq N \frac{l}{c} \qquad \text{Equation 3.1}$$

where N is the safety factor, l is the least element size and c is the speed of sound through the element.

Different types of spatial discretisation solvers are available to model various materials and their conditions, utilising the suitable features of each solver. A Lagrangian solver is used in the finite element method, in which the elements move with the material

during deformation. There is no flow of material from one element to another element. This solver is more suitable for solid objects where the deformation is addressed by the distortion of the mesh. For large deformation problems, this solver undergoes severe element distortion which may result in very small time steps (Δt) and grid tangling. An Eulerian solver is used in the finite difference method and/or finite volume method, in which the mesh remains undeformed while the material flows freely from one to another element. This solver is most suitable for fluid materials such as a gas or a liquid. The Eulerian solver can also be used to model solid objects where larger deformation is inevitable, but this solver has difficulty dealing with the material boundary conditions involving surface slippage in contact (Wang et al., 2005).

3.2 ARBITRARY LAGRANGIAN EULERIAN

The Arbitrary Lagrangian Eulerian (ALE) technique is introduced by combining the best features of pure Lagrangian and Eulerian solvers, while reducing their respective weaknesses. In ALE, the nodes in the computational mesh may be moved with the continuum in a Lagrangian manner, or held fixed in an Eulerian manner, or moved in some arbitrarily specified way to give a continuous rezoning capability. With this feature of freedom to move the computational mesh, the ALE efficiently handles the problem with greater distortions of the mesh than the purely Lagrangian method. It also offers more resolution than the purely Eulerian method. The ALE technique allows modelling of fluid-structure interactions (FSI) with a fluid structure coupling algorithm which satisfies the governing equations describing the conservation of mass, momentum and energy (Hallquist, 2006).

FSI is a coupled multi-physics simulation process for solving highly non-linear problems in a single model. Examples of this type of simulation include surface explosions, where the air is Eulerian and the soil and the tunnel are Lagrangian, and buried explosions, where the soil is Eulerian and the target tunnel is Lagrangian. In all cases, the Lagrangian mesh moves through the Eulerian mesh. Figure 3.1 shows the overlapping of the Lagrangian boundary with the Eulerian mesh. The coupling algorithm first searches for the intersections of the Eulerian mesh with Lagrangian mesh. When the Lagrangian surface is detected inside the Eulerian mesh, the algorithm applies pressure boundary conditions on the Largrangian mesh from the Eulerian mesh,

causing displacement on the structure. In return, the Lagrangian mesh boundaries act as velocity boundary (geometric constraints) in the Eulerian mesh (McMaster, 1984).

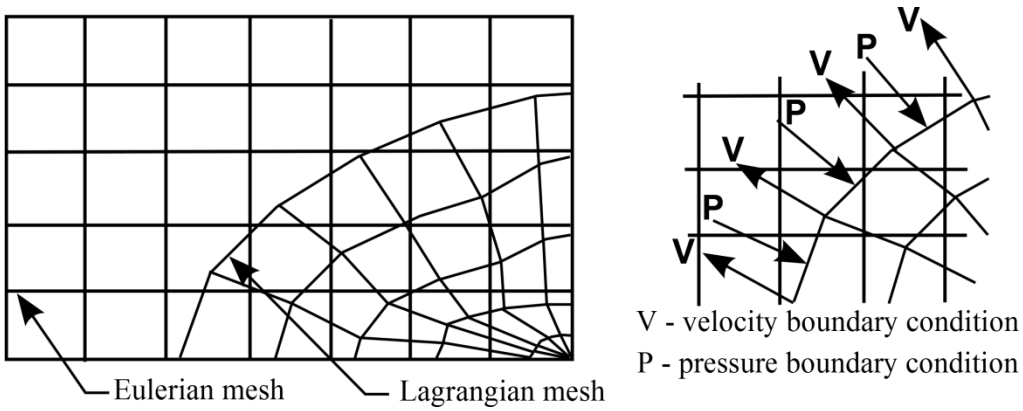

Figure 3.1: Lagrangian-Eulerian coupling

The simulation uses the ALE Multi-Material formulation to model a mixture of two or more different materials in each mesh (Alia & Souli, 2006). The explosive is prescribed into the surrounding (air or soil) using INITIAL_VOLUME_FRACTION option in LS-DYNA as a sphere or a cylinder or a cube. This allows the explosive substances to expand into the meshes initially occupied by the air or soil. The coupling between the Lagrangian meshes and Eulerian meshes is accomplished using CONSTRAINED_ LAGRANGE_IN_SOLID, where the penalty factor controls the penetration of the explosive-air volume fraction into the Lagragian mesh.

3.3 SMOOTH PARTICLE HYDRODYNAMICS

Smooth Particle Hydrodynamics (SPH) is a mesh-free computational Lagrangian hydrodynamic particle method. This method originated about three decades ago in astrophysical problems (Gingold & Monaghan, 1977; Lucy, 1977), where it dealt with the simulation of interacting fluid masses in vacuum without boundaries. It was then modified as a deterministic mesh-free particle method and implemented to continuum solid and fluid mechanics (Monaghan, 1992, 1994). SPH treats the solid mechanics problems in which large deformations and fragmentation occur. SPH is mathematically based on interpolation theory by utilizing kernel approximation of a function which is adequately smooth even for higher order derivatives and provides stable and accurate results. When SPH was initially implemented to fields other than astrophysics, it

suffered from the enforcing of finite boundary conditions. Modelling of finite element (FE) meshes as the boundaries for SPH particles offers a possible solution (Thiyahuddin et al., 2012).

SPH provides extensive ability as a numerical tool for modelling problems having large distortions and deformations. Unlike conventional Lagrangian meshes, SPH is free from mesh tangling and hourglassing effects. As such, SPH particles are used where large deformation or severe material failure occurs in near field domain and FE meshes are used where intermediate or small deformation is expected in far field domains.

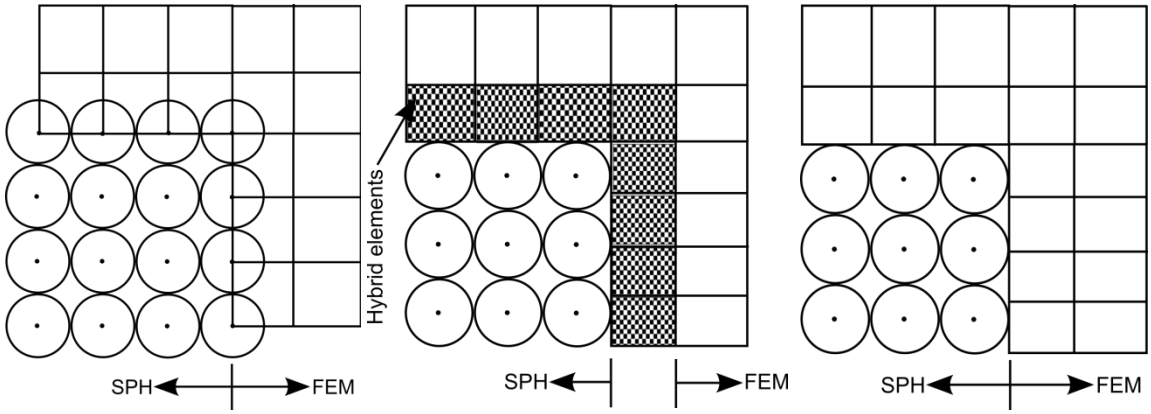

a) Tied interface b) Hybrid element coupling c) 'Nodes-to-surface' contact

Figure 3.2: Coupled SPH-FE Method

Although SPH is more expensive in terms of computation, the coupled SPH-FE approach reduces high computational demand. There are methods that allow the coupling interaction between SPH particles and FE meshes (Wang et al., 2005). A constraint interface ties SPH particles to the corresponding surfaces of FEM meshes as shown in Figure 3.2(a). This method requires due consideration in FEM mesh creation at the interface as it could cause unphysical penetration and system instability. Hybrid element coupling is a new feature in LS-DYNA. As shown in Figure 3.2(b), these elements constrain SPH particles and act as transit layers between SPH particles and FE meshes. The main advantage of this method is that no tied/contact interface is required. However, this method suffers from intruding SPH particles into FE mesh if hybrid elements are close to the explosive. The third method is a simple method where the interaction is achieved by the penalty based 'Nodes-to-surface' contact where solid elements as the master and SPH particles as the slave nodes as shown in Figure 3.2(c).

The 'Node-to-surface' coupling method is employed in the present study as SPH particles are close enough to achieve steady interface.

3.4 SIMULATION OF BLAST LOADING

Previous studies have shown that both ALE and SHP techniques are well suited to simulate the blast response of buried tunnels. The following sections describe the most significant key words used in the modelling of the problem.

3.4.1 Element selection

LS-DYNA provides several element formulation options for solids. Solid elements (Lagrangian elements) can be modelled using hexahedral-eight node fully integrated elements (ELFORM=2) or constant stress solid elements (ELFORM=1), which is the default formulation. Although ELFORM=2 is free from hourglass stabilization, it is computationally expensive for hi-fidelity models as well as too stiff, especially for poor aspect ratios. For most models, ELFORM=1 provides reliable results when suitable hourglass control is used. Although there are ALE element formulations (ELFORM=5, 6 and 12), the recommended ELFORM=11 is used for the multi-material ALE (Jayasinghe et al., 2013).

3.4.2 Boundary condition

As with the explosive charge centre, node displacements at the symmetry boundaries in the model can be restrained in their normal directions using symmetry boundary condition. The top surfaces of air and soil-air interface are considered as offering no constraints while the base of the model can be fixed in all directions to represent the bed rock. In SPH simulation, a special symmetry boundary BOUNDARY_SPH_ SYMMETRY_PLANE is used for the SPH particles at the symmetric boundaries. As reflection of shock waves at the far-field can affect the accuracy of the numerical simulation, non-reflecting boundary conditions (BOUNDARY_NON_REFLECTING) are placed to allow the shock wave to flow out the soil skeleton at the far-field infinite domain without reflection.

3.4.3 Contact interface

The SSI contact interface between tunnel and soil is a vital part of simulation involving penetration, sliding and separation. The selection of contact type depends on the interaction phenomenon between the SSI interfaces. LS-DYNA performs this operation by checking potential penetration of the slave set through a master set. Penetration algorithms conduct this check at each time step. AUTOMATIC contact option detects the penetration from both sides of contact. Therefore, orientations of slave set and master set are not important, making them more robust than non-automatic option. In this present study, the Soil-Structural Interaction (SSI) at the contact interface between the soil and the tunnel is described by CONTACT_AUTOMATIC_SURFACE_TO_SURFACE type contact. The most popular contact option CONTACT_AUTOMATIC_SINGLE_SURFACE is defined for self-contact between tunnel segments.

3.4.4 Reinforced concrete model

Precast tunnel segments are modelled using eight node hexahedral solid elements with Lagrangian processor while steel reinforcing bars are defined using two node Hughes-Liu beam elements with cross sectional integration. These reinforcing elements are simple, computationally efficient and compatible with most material types. The beam elements within the concrete segments can be modelled using the CONSTRAINED_LAGRANGE_IN_SOLID (CTYPE=2) coupling. This eliminates the burden of aligning the beam nodes to the solid element nodes. Minimum of three hexahedral elements are specified across its thickness to facilitate the non-linear stress distribution through the thickness.

3.4.5 Stress initialization

Stress initialisation is essential in geotechnical modelling to induce a steady state preload prior to the application of the transient load simulating the blast. In order to bring the model to a state of static equilibrium, a small amount of damping is incorporated and hence kinetic energy approaches zero. This can be achieved using time dependent mass damping option DAMPING_GLOBAL to impose near-critical damping until the preload is established in the model. The solution will be computed dynamically

until it converges to equilibrium. For optimal convergence, lowest mode of vibration frequency can be obtained from the damping constant D_S which is defined by:

$$D_S = \frac{2}{T} \qquad \text{Equation 3.2}$$

where T is the longest period of vibration for the model being computed from an undamped transient analysis.

The gravity load can be applied to the model using LOAD_BODY_Z option. The simulation used two curves: (i) gravity load curve includes a ramp load function and (ii) damping curve defines damping constant only during the stress initialization phase. For stability reasons, the stress initialization is normally conducted with a default time step SF of 0.90.

3.4.6 Data manipulation

LS-DYNA provides two formats of analysis data output such as binary files and ASCII. The binary data files contain the model's finite element response information (d3plot, d3thdt, d3dump, interface force file (intfor)). The binary file recording interval can be varied, for example, from 250μsec, 500μsec to 1000μsec, depending on how accurate peak measurements are required to capture the tunnel response during the explosion. LS-PrePost processes output from LS-DYNA to visualize the three-dimensional response. LS-PrePost reads results data files such as d3plot, intfor and all ASCII time history data files. The powerful animation and colour contour images on meshes produced by LS-PrePost include acceleration, velocity, displacement and element pressure time-history data. Furthermore, LS-PrePost computes a variety of strains, bending moments and reaction forces along the constrained boundaries. The binary d3dump files are automatically written at the end of normal termination can be used to restart the model by removing redundant elements in the model.

In addition, the Winfrith concrete model (LSTC, 2007) used in this study to simulate the blast response of reinforced concrete lining provides an attractive feature of monitoring crack propagation in the database. This database includes the information on crack

location, directions and widths. This crack database can be visualized on the deformed mesh output.

3.5 MATERIAL MODELS

The following section describes the material models considered for modelling air, high explosive, soil and reinforced concrete tunnel segments made of concrete and steel bars in the numerical simulation. They are:

3.5.1 Air model

The air is modelled as an ideal gas (LSTC, 2007) utilising MAT_NULL material model with a linear polynomial Equation of State (EOS). The null material model can effectively model fluids and hydrodynamic substances. The pressure is expressed by:

$$P = C_0 + C_1\mu + C_2\mu^2 + C_3\mu^3 + \left(C_4 + C_5\mu + C_6\mu^2\right)E \qquad \text{Equation 3.3}$$

where E is the internal energy per unit volume, C_0, C_1, C_2, C_3, C_4, C_5, and C_6 are constants and $\mu = \frac{\rho}{\rho_0} - 1$, where $\frac{\rho}{\rho_0}$ is the ratio of current density to initial density.

The linear polynomial equation represents an ideal gas with the gamma law EOS, in which C_0=C_1=C_2=C_3= C_6= 0 and C_4 = C_5= $\gamma - 1$, where γ is the ratio of specific heat at constant pressure per specified heat at constant volume. The pressure is then described by:

$$P = (\gamma - 1)\frac{\rho}{\rho_0} E_0 \qquad \text{Equation 3.4}$$

where:

$$E_0 = \rho_0 c_v \times T \qquad \text{Equation 3.5}$$

γ is an adiabatic constant for air behaving as an ideal gas (estimated value for γ =1.4), ρ is the density, c_v is the specific heat at constant volume and E_0 is the initial internal energy per unit volume. Table 3.1 shows the material parameters used for the air.

Table 3.1: Material properties for air (Yang et al. 2010)

Parameter	Value
ρ	1.29g/cm^3
C_0, C_1, C_2, C_3 and C_6	0
C_4 and C_5	0.4
E_0	0.25kJ/m^3

3.5.2 Explosive model

The Jone-Wilkin-Lee's EOS (LSTC, 2007) is used to describe the explosive as it is the most popular one and the easiest to calibrate. This EOS defines the pressure as below:

$$P = A\left(1-\frac{\omega}{R_1V}\right)e^{-R_1V} + B\left(1-\frac{\omega}{R_2V}\right)e^{-R_2V} + \frac{\omega E}{V} \qquad \text{Equation 3.6}$$

In the above equation V is the relative volume or the expansion of the explosive, E is the initial energy per volume, v_D is the detonation velocity, P_{CJ} is the pressure at the critical point, A, B, R_1, R_2 and ω are empirically derived constants for the explosive. This equation allows using a wide range of different high explosive parameters such as for TNT (Wang et al., 2005) and C-4 (Wang et al., 2001) explosives. Table 4.2 shows the material parameters for TNT and C-4 explosive charges.

Table 3.2: Material parameters for TNT explosive

Parameters	TNT	C-4
ρ (g/cm^3)	1.630	1.601
v_D (m/s)	6930	8193
P_{CJ} (GPa)	21	28
A (GPa)	373.77	609.97
B (GPa)	3.747	12.95
R_1	4.15	4.5
R_2	0.90	1.4
ω	0.35	0.25
V	1	1
E0 (kJ/m^3)	6.0e+06	9.0e+06

3.5.3 Soil model

Soils with different moisture contents give different responses to high strain-rate dynamic loading, such as direct impact and blast loading. This research uses an appropriate soil model that incorporates the various soil compositions, in particular, moisture content. By evaluating several material models in LS-DYNA, MAT_FHWA_SOIL model is identified as a suitable soil model that includes strain softening, kinematic hardening, strain rate effects, element deletion, excess pore water effects and stability with no soil confinement (Lewis, 2004; Saleh & Edwards, 2011). Furthermore, the model simulates an isotropic material behaviour with failure. The material model was developed by the Federal Highway Administration (FHWA) in 2004. The FHWA soil model is based on a modified Mohr-Coulomb yield criterion (Abbo & Sloan, 1995). The modified yield surface is a smooth hyperbolic surface which enables an accurate, robust, and a significant computational saving in numerical simulation.

There are a total of 25 material parameters in the FHWA soil model. Among those parameters, the material model requires main parameters such as, mass density, specific gravity, bulk modulus, shear modulus and moisture content. These soil parameters are generally determined through laboratory tests. Parameters required for defining strain softening, kinematic hardening, strain rate effects and pore water effects can be evaluated through laboratory tests and/or equations in the material manual (Lewis, 2004). By considering the pore-water effect, Sivalingam et al. (2014), Jayasinghe et al. (2013) and Ortman and Catherine (2008) and Lee (2006) successfully employed the model for studying the blast effect in fully saturated soil. If the soil is unsaturated or dry, the same model can be utilised by eliminating pore-water effects (Lee, 2006). Saleh and Saleh and Edwards (2011) also used this model for investigating the interaction of landmine explosion with protective structures by ignoring the pore-water effects. Values recommended by Lee (2006) were used in this study to include the strain softening, kinematic hardening and strain rate effects in the soil.

Shear and bulk moduli are two of the main parameters. Shear wave velocity (V_S) is a valuable indicator of the dynamic soil properties because of its relationship with the shear modulus (G) as given by Equation 3.7 (Kramer, 1996):

$$G = \rho V_S^2 \qquad \text{Equation 3.7}$$

where ρ is the soil density.

A wide variety of field and laboratory tests are available to evaluate the magnitude of primary wave (V_P) and shear wave (V_S) velocities. The velocities of V_P and V_S depend on the compressibility of the soil body through Equation 3.8 (Kramer, 1996):

$$\frac{V_P}{V_S} = \sqrt{\frac{2-2\nu}{1-2\nu}} \qquad \text{Equation 3.8}$$

where ν is the Poisson's ratio of soil.

This ratio is typically assumed to be constant in the studies of both dry and saturated soils of homogeneous and isotropic media. However, the Poisson's ratio varies with the degree of saturation. For a typical Poisson's ratio of 0.3 for dry sandy soil, the ratio V_P/V_S is 1.87. However, for low shear velocity materials such as saturated clay, the Poisson's ratio can be close enough to 0.5. When it approaches to 0.5, the ratio V_P/V_S is infinite.

The bulk modulus (K) is a degree of resistance against volumetric compression. The compressibility of the material is the reciprocal of the bulk modulus that relates the shear modulus (G) with the Poisson's ratio (ν), given by Equation 3.9:

$$K = \frac{2G(1+\nu)}{3(1-2\nu)} \qquad \text{Equation 3.9}$$

The soil skeleton has pores filled with air and/or water. The water filled in the pores creates pore water pressure. The MAT_FHWA_SOIL soil model handles pore water pressure build-up using the relationship between pore-water pressure (u) and volumetric compression strain (ε_v) as shown in Equation 3.10 (Lewis, 2004).

$$u = \frac{K_{sk}}{1 + K_{sk} D_2 n_{cur}} \varepsilon_v \qquad \text{Equation 3.10}$$

where K_{sk} = skeleton modulus, n_{cur} = current porosity due to air voids and D_2 = a function of Skempton's pore-water pressure.

Equation 3.11 defines the parameter D_2 from Skempton pore-water pressure parameter B, as shown below:

$$B = \frac{1}{1 + n\frac{K_{sk}}{K}}, \qquad D_2 = \frac{1 - B}{BK_{sk}[n(1 - S)]} \qquad \text{Equation 3.11}$$

where n = soil porosity and S = degree of saturation.

The parameter D_2 is constant for partially saturated soil. For fully saturated case, the constant D_2 has no effect on pore-water pressure (i.e $D_2 = 0$) (Lee, 2006). As described by Lee (2006), K_{sk} is the volumetric strain factor which varies between 5% and 20% of material bulk modulus.

The effects of excess pore-water pressure are defined in the material model using Equation 3.12 (Lewis, 2004).

$$K = \frac{K_i}{1 + K_i D_1 n_{cur}} \qquad \text{Equation 3.12}$$

where K_i = nonporous bulk modulus and D_1 = stiffness of the soil by adjusting the bulk modulus before the air voids are collapsed. For fully saturated case, Lee (2006) estimated D_1 to be 4.63GPa^{-1}.

Inclusion of water in soil changes the magnitude of shear and bulk moduli with degree of saturation. Water has very low compressibility (higher bulk modulus ≈ 2GPa) and negligible resistance to shear or distortional loads (negligible shear modulus). Naesgaard et al. (2007) reported that the shear wave velocity (V_S) is essentially independent of the Skempton parameter B. Therefore, the saturated shear modulus (G_{sat}) can be assumed to be the same as the dry shear modulus (G). If laboratory or field data are available, Equation 3.13 can be used to evaluate G_{sat}.

$$G_{sat} = \rho_{sat} V_{S-sat}^2 \qquad \text{Equation 3.13}$$

The bulk modulus of water has more influence over the soil-water mixture than the bulk modulus of solid soil particle. Therefore, the bulk modulus of the soil-water composite mixture should be within those of water and soil bulk moduli. Lee (2006) described additional insights of the evaluation of the saturated bulk modulus (K_{sat}). Alternatively, laboratory and field tests can help to evaluate the primary wave velocity (V_P) of saturated soil. The magnitude of the saturated bulk modulus (K_{sat}) can be evaluated from Equation 3.14.

$$K_{sat} = \rho_{sat} V_{P-sat}^2 - \frac{4}{3} G_{sat} \qquad \text{Equation 3.14}$$

where $V_{P\text{-}sat}$ is the primary wave velocity in saturated soil.

3.5.4 Concrete model

Dynamic performance of concrete structures subjected to blast effects is a complex nonlinear and rate-dependent process, in which the apparent concrete strength can increase significantly. LS-DYNA material library has several advanced constitutive material models developed to simulate the concrete material behaviour. However, in many circumstances, the necessary material parameters for the concrete cannot be found in the literature. This study utilized a common material model MAT_WINFRITH_ CONCRETE (LSTC, 2007) which has the automatic generation capability of concrete law parameters. This material model originated in the nuclear industry to simulate the response of reinforced concrete structures subjected to blast and impact loading.

This model is based on the shear failure surface proposed by Ottosen (1977) and includes the strain rate effects and strain softening in tension by incorporating crack opening width or fracture energy. The shear failure surface is expressed by a quadratic equation given as:

$$F(I_1, J_{2,} \cos 3\theta) = a \frac{J_2}{(f_c^{'})^2} + \lambda \frac{\sqrt{J_2}}{f_c^{'}} + b \frac{I_1}{f_c^{'}} - 1 \qquad \text{Equation 3.15}$$

where I_1 is the first invariant of stress component representing volumetric responses and J_2 is the second invariant of the deviatoric stress component which accounts for deviatoric response. The constants a and b control the meridional shape of the shear failure surface. These parameters are internally generated in the Winfrith concrete model based on input parameters such as unconfined tensile and compressive strengths.

$$\lambda = \begin{cases} k_1 \cos\left[\dfrac{\cos^{-1}(k_2 \cos 3\theta)}{3}\right], & \text{for } \cos 3\theta \geq 0 \\ k_1 \cos\left[\dfrac{\pi}{3} - \dfrac{\cos^{-1}(-k_2 \cos 3\theta)}{3}\right], & \text{for } \cos 3\theta < 0 \end{cases} \qquad \text{Equation 3.16}$$

where k_1 and k_2 are functions of the ratio of the unconfined tensile to compressive strength (f_t / f_c'). They define the shape of the shear failure surface in the octahedral plane.

$$\cos 3\theta = \frac{3\sqrt{3}}{2} \frac{J_3}{J_2^{1.5}} \qquad \text{Equation 3.17}$$

where J_2 and J_3 are the deviatoric stress components and the angle θ is referred to as the Lode Angle.

This is a simple input concrete model which requires the unconfined compressive strength and tensile strength. For known concrete weight and unconfined concrete compressive strength, Young's modulus (E) is calculated from an equation recommended by ACI Committee 318 as below:

$$E = 33 w^{1.5} \sqrt{f_c'} \qquad \text{Equation 3.18}$$

where w is the concrete weight in lb/ft^3 and f_c' is the compressive strength of normal strength concrete in psi.

3.5.5 Reinforcement model

In the present study, material model MAT_PLASTIC_KINEMATIC is employed to model the steel reinforcement. This model is more efficient in terms of the computational demand. The steel is an isotropic elastic-plastic material with the same initial yield stress for both uniaxial tension and compression. It uses Von-Mises yield criterion to define the yield function of the steel, as given by:

$$\begin{aligned} F(J_2) &= 0 \\ \sqrt{3J_2} - \sigma_y &= 0 \\ \sigma_y &= \sqrt{\frac{3}{2} s_{ij} s_{ji}} \end{aligned} \qquad \text{Equation 3.19}$$

where J_2 is the second invariant of the deviatoric stresses s_{ij}.

The strain rate effect is incorporated by using the Cowper Symonds strain rate relationship given by Equation 3.20.

$$\sigma_y = \left[1 + \left(\frac{\dot{\epsilon}}{C} \right)^{\frac{1}{P}} \right] \left(\sigma_0 + \beta E_P \epsilon_{eff}^{P} \right) \qquad \text{Equation 3.20}$$

where, σ_y is the dynamic flow stress at a uniaxial plastic strain rate $\dot{\epsilon}$, σ_0 is the associated flow stress, E_P is the plastic modulus and ϵ_{eff}^{P} is the effective plastic strain of the material. This equation computes the strain rate dependent factors to scale the yield stress. Parameter β is included to differentiate the type of plastic hardening in the material model. For elastic perfectly-plastic material with kinematic hardening ($\beta = 0$) and hence the surplus stress of the plastic hardening part $\beta E_P \epsilon_{eff}^{P}$ is omitted. C and P are strain rate Cowper-Symonds coefficients which were evaluated based on best fitting of the Dynamic Increased Factor (DIF) of steel reinforcement as described by Malvar and Crawford (1998). This model also includes failure upon reaching a predefined value of failure strain.

3.6 CHAPTER SUMMARY

This chapter focused on the theory behind the numerical techniques and constitutive material models for simulation of buried tunnel structure subjected to surface explosion. Two different numerical approaches, Arbitrary Lagrangian-Eulerian (ALE) and Smooth Particle Hydrodynamics (SPH), for fluid-structure interaction in blast problems were described. The general purpose finite element hydrocode LS-DYNA will be used to perform those techniques, incorporating the fully coupled numerical simulation and different material models utilising strain rate effects.

In the present study, atmospheric air surrounding explosive is modelled using null material model with a linear polynomial equation of state while the explosion process is modeled using the Jones-Wilkens-Lee (JWL) equation of state with high burn material model. FHWA material model is used for the soil to incorporate the strain softening, kinematic hardening, strain rate effects, element deletion, and excess pore water effects. The Winfrith concrete model is chosen to simulate the concrete, in which the reinforcement is separately modelled as an isotropic elastic-plastic material by 'Constrained Lagrange In Solid' coupling. Gravity preload is incorporated using time dependent mass damping. Self-contact surfaces are used to define joint interfaces of segments using the CONTACT_AUTOMATIC_SINGLE_SURFACE type contact. The contact interface between the tunnel exterior surface and soil is simulated using the CONTACT_AUTOMATIC_ SURFACE_TO_SURFACE type contact.

Chapter 4: Validation of Numerical Models

4.1 INTRODUCTION

Model verification and validation are essential for the development of numerical models that can be used to make engineering predictions with quantified confidence. This chapter presents the validation of the two numerical approaches reported in the previous chapter:

1. Coupled FSI in ALE (ALE method).
2. Coupled SPH-FE (SPH method).

For the validation purpose, two experiments from the literature are considered. These are: (1) a series of tests conducted by De (2012) and De et al. (2013) that study the surface blast effect on a buried copper pipe in dry sand and (2) Conventional Weapon Effects Backfill (CONWEB) test series carried out by Hayes (1989) to investigate the underground blast response of a buried Reinforced Concrete (RC) structure in various backfill soil conditions. Figure 4.1 shows the flowchart of the validation process of numerical techniques and relevant material models.

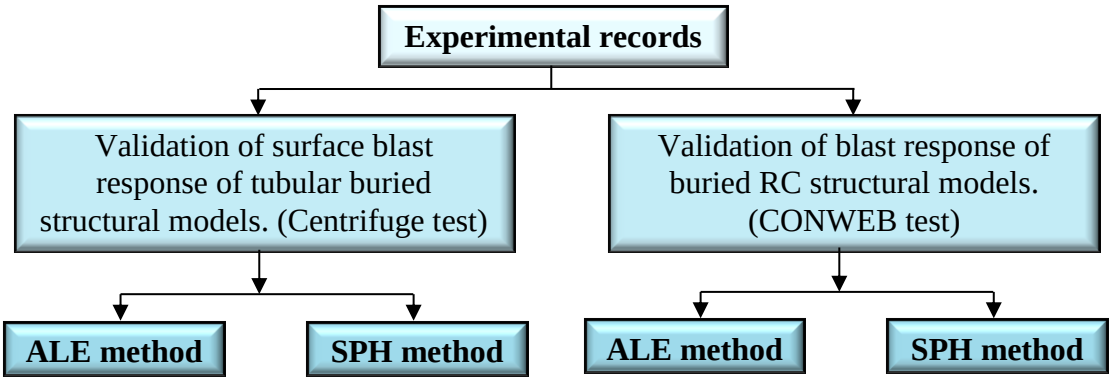

Figure 4.1: Flowchart used for validation of numerical techniques and material models

4.2 VALIDATION OF ALE SIMULATIONS USING CENTRIFUGE TEST RESULTS

The study first simulated and validated the experiment conducted by De (2012) who used a 70g centrifuge testing machine, where g is the gravitational acceleration. De (2012) investigated the blast response of a tubular tunnel structure using the centrifuge models.

4.2.1 Description of centrifuge test

The scaled-down model composed of a tubular copper tunnel buried in dry Nevada sand (relative density (D_r) = 60%) at a depth of 3.6m equivalent to prototype scale as shown in Figure 4.2. A spherical shape explosive was symmetrically placed above the midspan, directly over the centreline of the copper tunnel, such that the ground surface was tangent to the spherical surface of the explosive.

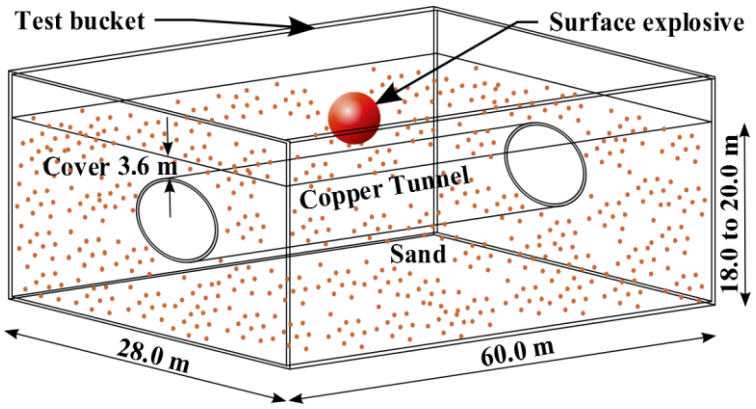

Figure 4.2: Setup of experimental model (All dimensions are in prototype scale) (De & Zimmie, 2011)

The copper tunnel was instrumented with 19 strain gauges to monitor axial, circumferential and shear strains at different locations on the tunnel. For comparison purposes, three gauge readings reported by De (2012) and De & Zimmie (2011) were considered. Figure 4.3 describes these gauge locations in the prototype scale.

Centrifuge scaling factors show how a field model and its dynamic events are correlated in the centrifuge test, in which the scaled model is sufficiently raised to N times the gravitational acceleration. Scaling factors for different parameters are shown in Table 4.1.

Based on the centrifuge scaling laws, Table 4.2 lists the corresponding prototype model dimensions for the numerical simulation.

Table 4.1: Scaling law (Kramer, 1996)

Type of event	Parameter	Model dimension / Prototype dimension
All events	Stress	1
	Strain	1
	Length	1/N
	Mass	$1/N^3$
	Density	1
	Force	$1/N^2$
	Gravity	N
Dynamic events	Time	1/N
	Velocity	1
	Acceleration	N

Table 4.2: Conversion to prototype model (De, 2012)

Parameters	Model dimension	Prototype dimension
Copper tunnel diameter	76mm	5.32m
Copper tunnel thickness	2.5mm	175mm
Explosive weight of TNT	2.6g	888kg

4.2.2 Development of numerical model

Symmetric modelling capabilities play an important role in this numerical simulation to reduce the computational cost by considering a quarter symmetry-geometrical prototype models with a size of 20m x 16m x 15m as shown in Figure 4.3. This prototype model was used to represent the Lagrangian structure which is composed of only two major parts: copper tunnel and soil.

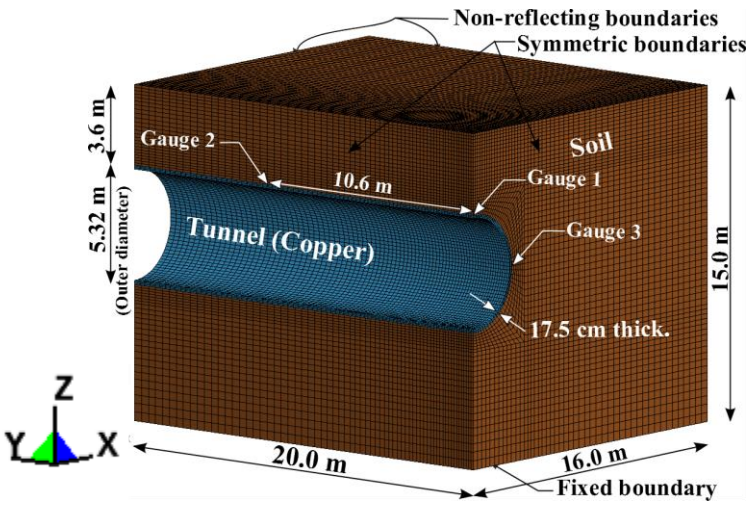

Figure 4.3: A quarter symmetrical prototype model (Lagrangian structure)

Eight-node solid elements were used with different spatial discretisation solvers. Lagrangian meshes were used to model the soil and copper tunnel while ALE meshes (background mesh) were used separately to model the surrounding air and explosive. A mesh consistency condition was achieved through a series of cases with different meshes to capture the analytical solution in the limit of a mesh refinement process. The Lagrangian soil structure used smaller element size of 12.5cm x 12.5cm x 12.5cm in the region adjacent to the explosive and larger element size of 40cm x 40cm x 40cm for far field region.

The copper tunnel was modelled with due consideration for a greater mesh refinement of curved surfaces. Peaks and valleys on the curved surface of copper tunnel interlock with the interface of soil elements and the element interlocking can cause initial penetration and crossed edges. Therefore, nodes on the soil interface were modelled to be coincident with those of the tunnel interface to minimize the element interlocking. The tunnel used three elements across its thickness to facilitate a nonlinear stress distribution through the thickness. The tunnel was further refined with a gradual increase in element size in both axial and circumferential directions away from the incident blast. The size of the smallest element in the tunnel was 10.25cm x 12.5cm x 5.83cm.

The spherical shape explosive was defined into the background mesh by using INITIAL_ VOLUME_FRACTION_GEOMETRY, by specifying its radius and detonation point. The contact interface simulation between the soil and the tunnel surfaces is crucial to an accurate analysis of tunnel response. The contact interface was modelled using CONTACT_

AUTOMATIC_SURFACE_TO_SURFACE type contact. The translational displacements of symmetry boundaries XZ and YZ planes are constrained in their normal directions. The non-reflecting boundary condition was applied to the infinite domain of both the Eulerian and the Lagrangian meshes while the base was fixed in all directions to represent the bed rock.

4.2.3 Material models and parameters

The material models and relevant material properties for the air and explosive described in Chapter 3.5 were employed in the simulation. The copper tunnel was modelled using MAT_PLASTICIY_KINEMATIC material model which incorporated both non-linear material behaviour and high strain rate effects due to the ground shock. Material parameters for copper (Matuska, 1984; Peroni et al., 2009) are described in Table 4.3. The main parameters include mass density (ρ), Young's modulus (E_s), Poisson's ratio (ν), yield stress (σ_y), tangent modulus (E_{tan}), hardening parameter (β) and strain rate parameters (C) & (P) for Cowper Symonds strain rate model.

Table 4.3: Material parameters for copper.

ρ g/cm^3	E_s GPa	ν	σ MPa	E_{tan} MPa	β	C s^{-1}	P
8.93	117	0.35	400	100	0	1.346e+06	5.286

For the Civil and Mechanical Systems Program of the National Science Foundation (NSF), Nevada sand (at a relative density (Dr) of 60%) was used for centrifuge tests by De (2012). Arulmoli et al. (1992) conducted an extensive laboratory test for the Nevada sand with different D_r values including: 40% and 60% in the VELACS (Verification of Liquefaction Analyses by Centrifuge Studies) Program. From Cyclic Triaxial Test data for Nevada sand at Dr = 60% (Arulmoli et al., 1992), the main soil parameters such as mass density (ρ), specific gravity (G_s) and moisture content were reported.

Based on initial void ratio, porosity of the sand was derived as 0.4. De (2012) presented data for density (ρ) versus sound speed (c) that was used for back-calculation of shear modulus (G). For Nevada sand ν = 0.33 (De, 2012), the ratio V_P/V_S is 1.985. Using this ratio of

V_P/V_S, the shear wave velocity (V_S) can be calculated using Equation 4.1 for known initial sound speed (c) at initial mass density of 1.6g/cm^3.

$$V_S = \sqrt{\frac{3(V_P^2 - c^2)}{4}} \qquad \text{Equation 4.1}$$

Equation 3.7 was used to compute the shear modulus (G), which is consistent with the shear modulus evaluated from resonant column test for dry Nevada sand at D_r = 60% (Arulmoli et al., 1992). The Bulk modulus (K) was derived using Equation 3.9. Table 4.4 shows the material parameters for the Nevada dry sand.

Table 4.4: Material parameters for soil

Parameters	Dry Nevada sand
Density (g/cm^3)	1.60
Specific gravity	2.67
Shear modulus (MPa)	56.0
Bulk modulus (MPa)	146.0
Cohesion (MPa)	6.20e-03
Friction angle	35^o
Moisture content (%)	0
PWD_1 (MPa^{-1})	0
PWD_2 (MPa^{-1})	0

4.2.4 Description of three stage simulation

In order to minimise the computational cost, the numerical modelling technique was divided into a time-ordered sequence of interrelated phases which described the entire simulation. LS-DYNA's restart feature enables the entire simulation to be broken into three stages such as stress initialization, ALE/Lagrangian coupling and deletion of ALE background mesh.

The model was first preloaded quasi-statically in the form of a ramped load curve with DAMPING_GLOBAL option which removed the unwanted oscillations in the model. Figure 4.4 shows the Kinetic Energy (KE) vs. time plot during the stress initialization, where the KE converged to zero at 150ms.

In addition, three gauge points such as on tunnel crown, springline and invert of the tunnel cross section at midspan verified the initialization process by using vertical displacement vs. time plots as shown in Figure 4.5.

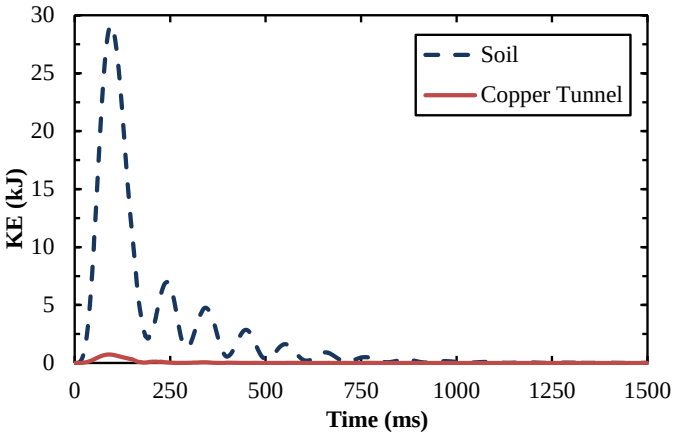

Figure 4.4: Kinetic energy vs. time during the initialization

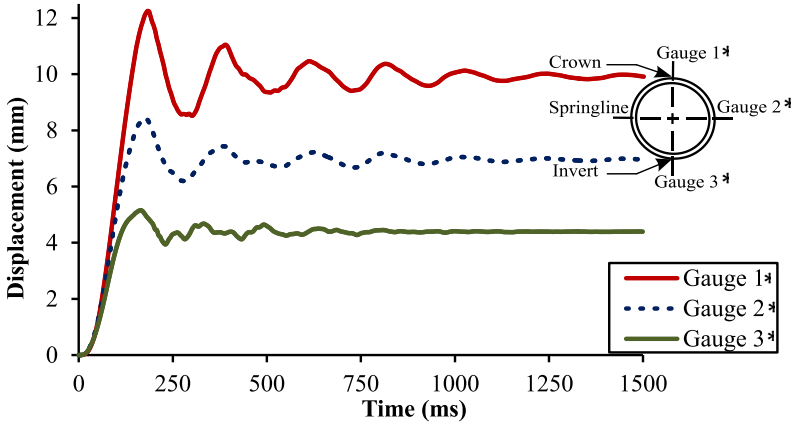

Figure 4.5: Displacement vs. time for three gauges

Figure 4.6 describes the background (ALE) mesh insertion into the preloaded Lagrangian model. The option CONSTRAINED_LAGRANGE_IN_SOLID enabled the

coupling of the Eulerian meshes across the Lagrangian meshes during load transfer. Degree of accuracy in ALE/Lagrangian coupling depends on the appropriate refinement of Eulerian mesh inside the Lagrangian mesh. Smaller Eulerian mesh size increases computational cost. Therefore, for adequate solution, at least 10 elements in the Eulerian mesh flow passage were modelled to be nearly the same size as the Lagrangian mesh.

The ALE/Lagrangian coupling phase is more expensive than the other two phases as it deals with FSI which is complex to solve analytically. However, the duration for the blast load transfer from ALE domain to Lagrangian parts is considerably small as evident from Figure 4.7. It can be observed that the KE of ALE background mesh is sufficiently reduced to zero in about 180ms. This highlights that ALE background mesh is only necessary for duration of the load transfer and is ineffective beyond that time (even if the analysis continues without removing it).

LS-DYNA's restart features DELETE_PART and DELETE_FSI were used to remove the redundant ALE background mesh and ALE/Lagrangian coupling respectively. Deletion of redundant elements from the model reduced the computational time considerably.

4.2.5 Shockwave propagation

Immediately after the detonation (at t_0 = 1500 ms), spherical shock waves propagated in the air from the charge epicentre which was 50.5cm above the ground. The shock waves travelled into the ground in the form of hemispherical waves while forming a crater in the ground, as shown in Figure 4.8. The area of the wave front expanded with the wave propagation. A set of fringe range on the right side of Figure 4.8 illustrate that the variation of shock wave pressure in Mbar between positive and negatives values. The wave front reached the tunnel surface after 7ms of explosion.

Without the tunnel structure, a free field numerical model, as shown in Figure 4.9(a), was considered to monitor the shock wave propagation in soil. Figure 4.9(b) illustrates the arrangement of measuring gauges at 3m spacing along two grid directions. Grid 1 is vertically below the explosive while Grid 2 is inclined by 45^0 to the ground surface.

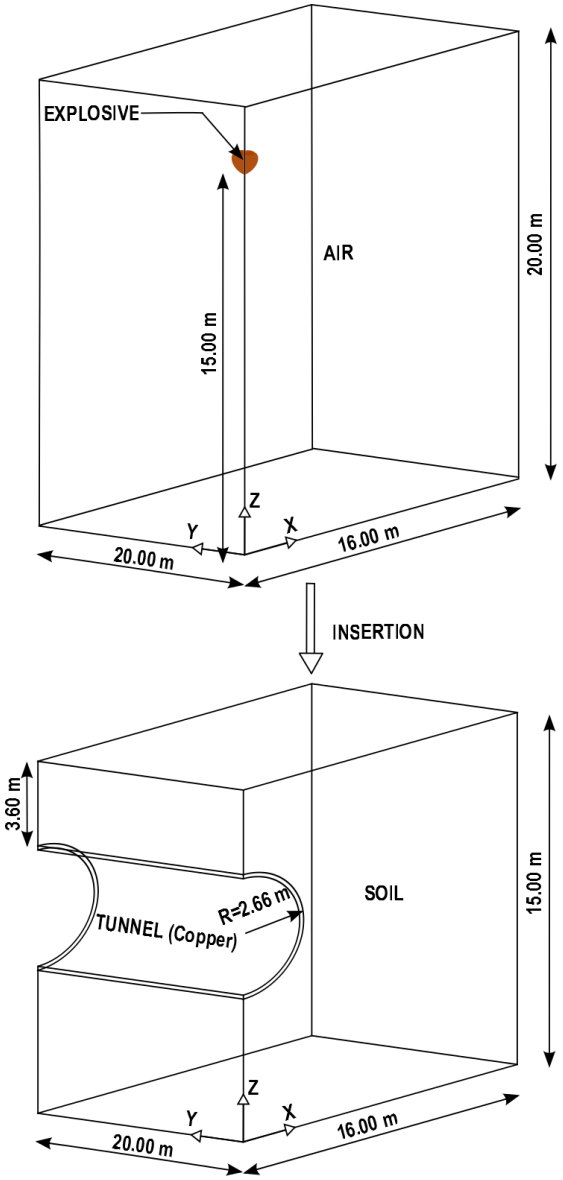

Figure 4.6: Insertion of ALE background mesh into Lagrangian structure

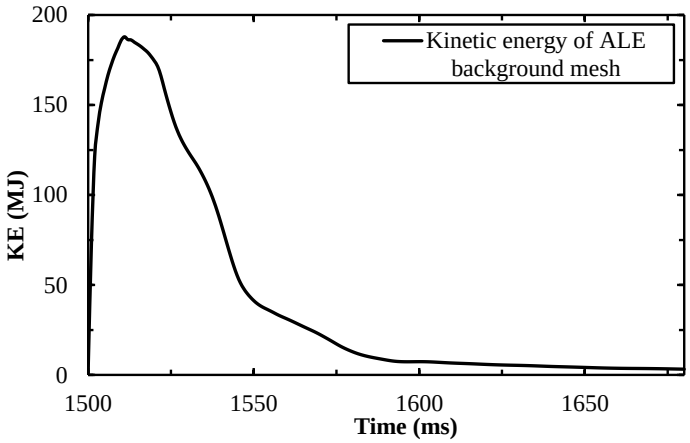

Figure 4.7: Kinetic energy vs. time plot of ALE background mesh

Gauges in Grid 1 are located in the central zone (Yang et al., 2010) to capture the intensity of shock wave which is mainly due to the compressive waves in the soil. Gauges in Grid 2 are located at the interface between the central and surface zones (Yang et al., 2010). Figure 4.10 shows the peak pressure variation with respect to the equivalent scaled distance of $R/W^{1/3}$ of the explosive. The propagation and attenuation of the shock waves in soil are clearly demonstrated by the two plots in Grid 1 and Grid 2. By comparing readings in Grid 1 and Grid 2, it is evident that gauges in Grid 1 experienced slightly higher peak pressures than the corresponding gauges in Grid 2. This could be due to the fact that the corresponding gauges in Grid 2 are shallower and located at the interface between the central and surface zones.

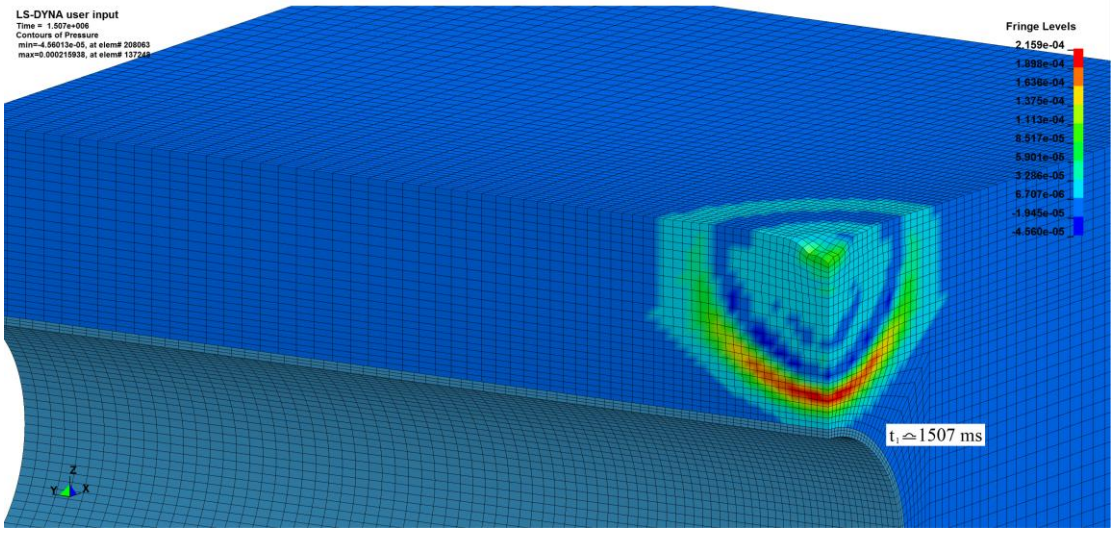

Figure 4.8: Propagation of shock wave in dry sand

Empirical equations of the power law in the technical manual TM5-855-1 (Department of the Army, 1986) can be used to estimate the peak pressure range. In order to derive equations for the type of soil considered in the simulation, the more appropriate soil properties of acoustic impedance (*pc*) and attenuation coefficient (*n*) are selected as 51.41kPa/ms^{-1} and 2.625±0.125 (Department of the Army, 1986) respectively, for a known seismic speed. The following two empirical equations are derived by substituting the upper and lower limits of *n* in the TM5-855-1 empirical equations for free field pressure. These two equations are plotted on a logarithmic scale as two straight lines shown in Figure 4.10. The slopes of a straight line represent the attenuation coefficients.

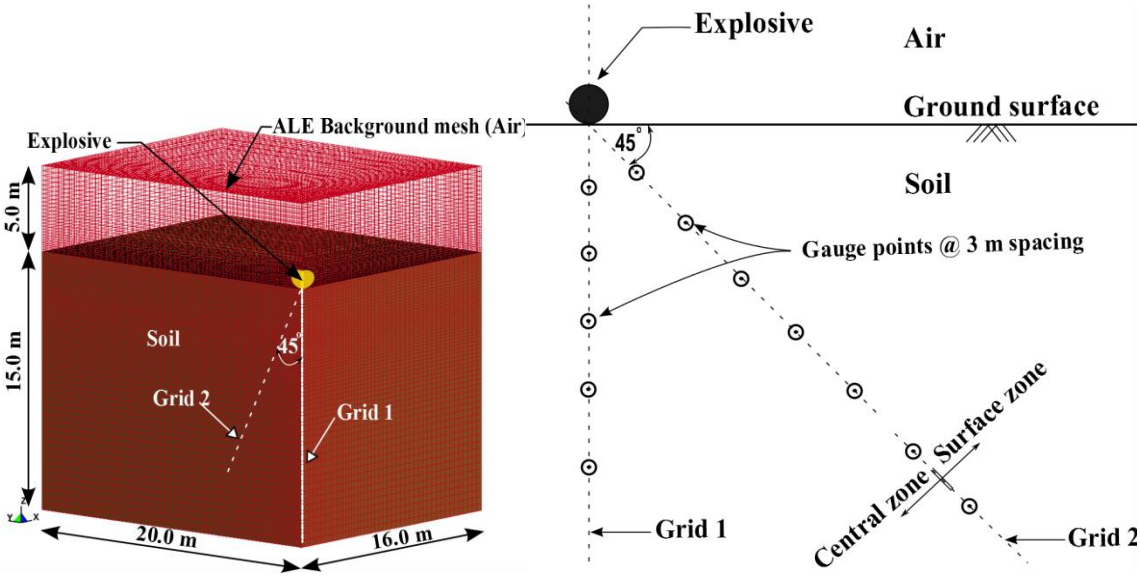

a) Free filed numerical model b) Measuring gauge points

Figure 4.9: Free field numerical model for wave propagation study

$$P_0 = f \cdot 22 \cdot \left(\frac{R}{\sqrt[3]{W}} \right)^{-2.75} ; \quad n = 2.75 \qquad \text{Equation 4.2}$$

$$P_0 = f \cdot 27 \cdot \left(\frac{R}{\sqrt[3]{W}} \right)^{-2.50} ; \quad n = 2.50 \qquad \text{Equation 4.3}$$

where P_0 is the peak pressure in MPa, f is the coupling factor which has a recommended constant value of f = 0.14 for explosion in air, R is the distance to the explosive in m, and W is the explosive weight in kg.

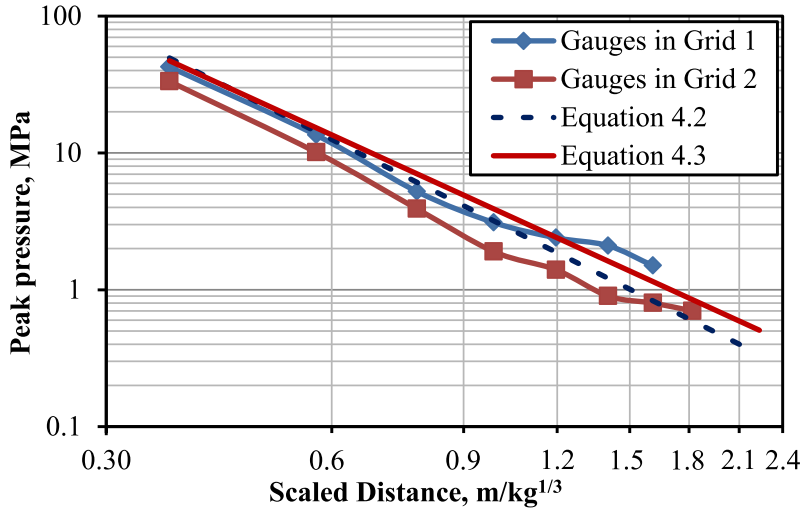

Figure 4.10: Comparison of peak pressure distributions along Grid 1 and Grid 2

Gauge readings along Grid 1 agreed reasonably well with the estimated peak pressure values from Equation 4.3. Shallower depth readings along Grid 2 slightly deviated from both straight lines, but they fell into the straight lines as the depth increased beyond the scale distance of 1.60m/kg$^{1/3}$. This discrepancy may be the result of the limitation of power law for a certain distance range (Yankelevsky et al., 2011). According to Yankelevsky et al. (2011) some types of soils may not be represented by a linear relationship on a logarithmic scale, but need to be described by either bi-linear or tri-linear relationships.

4.2.6 Tunnel response

The tunnel started to respond to the blast when the shock wave hit the tunnel and the response continued until the shock wave completely attenuated in the soil. Figure 4.11 shows the time history of kinetic energy (KE) of the tunnel response after the explosion. The tunnel response commenced at t_1 = 1507ms by imparting inertia load to the tunnel from the surrounding soil and the response reached its peak within 4.5ms. The tunnel dissipated 90% of its KE within 23ms of initial response period.

The process of the pressure wave propagation through the tunnel is presented in Figure 4.12 at different time intervals of the tunnel response. While the pressure wave travelled along both the longitudinal and the circumferential directions of the tunnel, positive and negative phases of pressure contours changed with time.

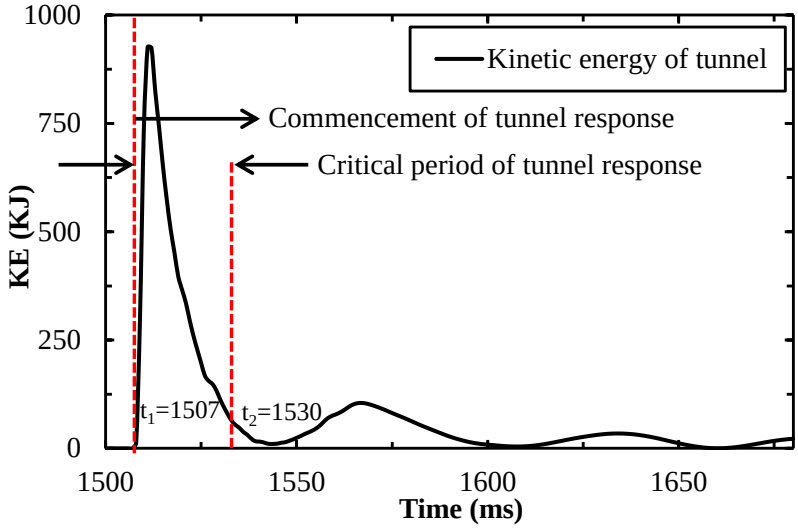

Figure 4.11: Kinetic energy vs. time plot for tunnel

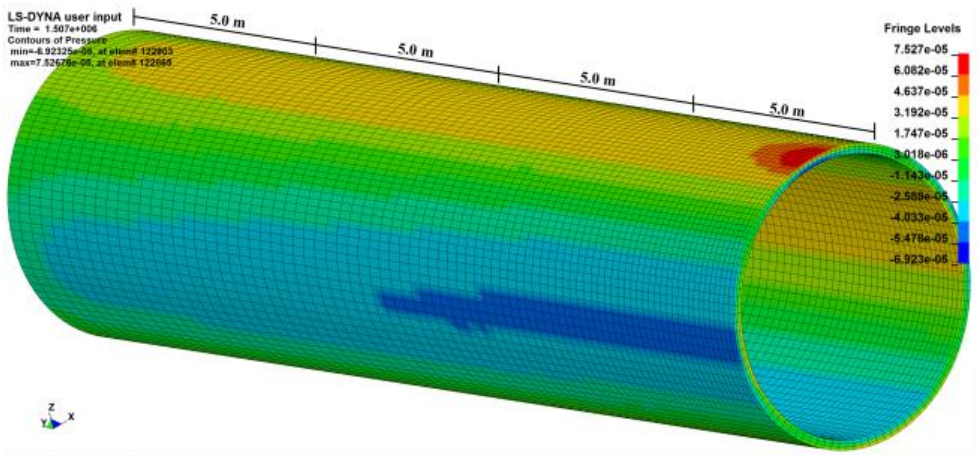

(a) 1507 ms

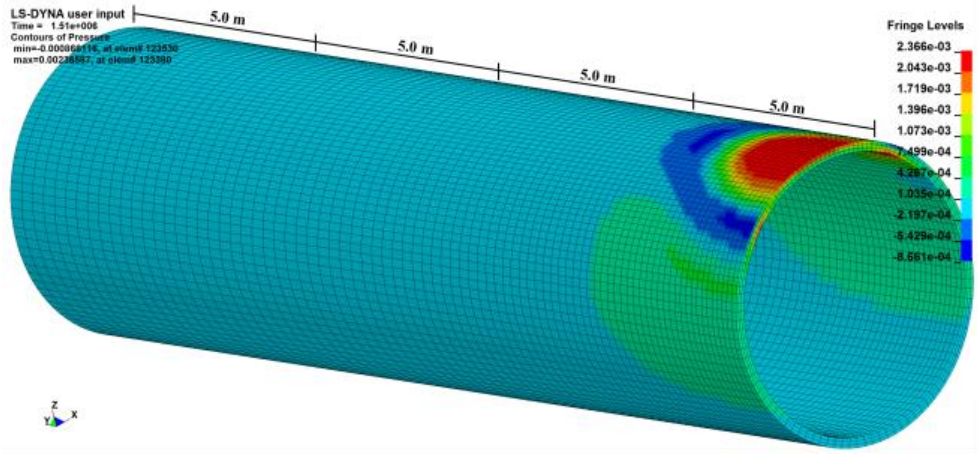

(b) 1510 ms

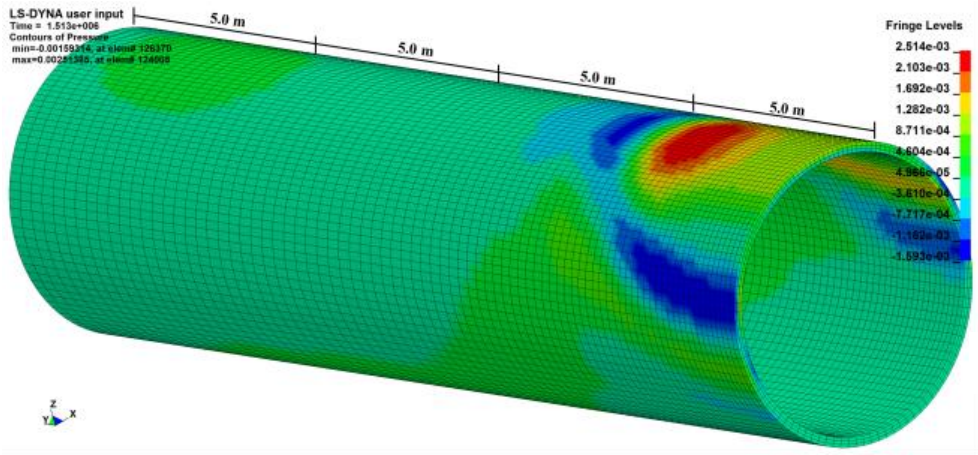

(c) 1513 ms

Figure 4.12: Pressure wave propagation through the tunnel

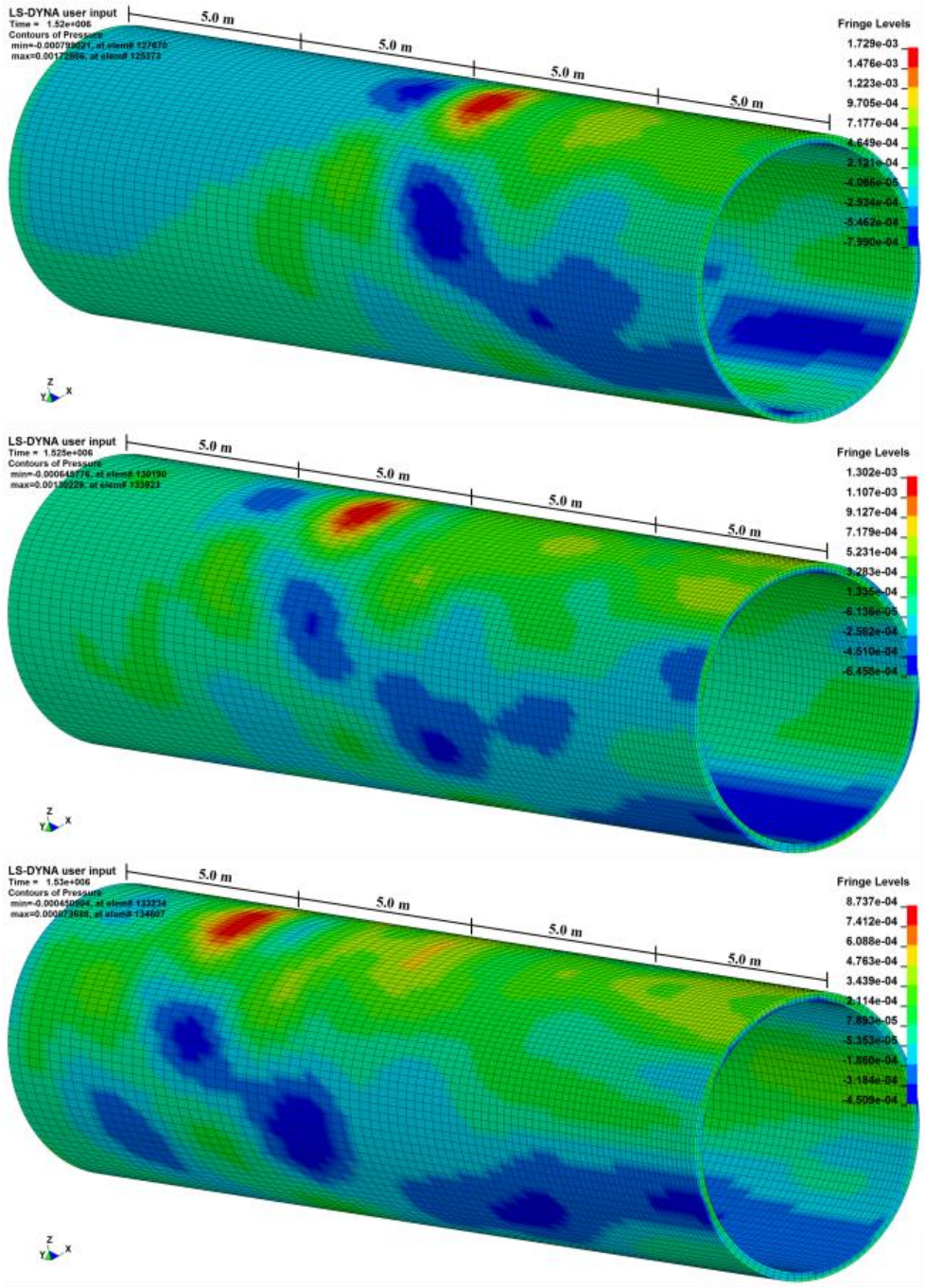

(d)1520 ms

(e)1525 ms

(f) 1530 ms

Figure 4.12: Pressure wave propagation through the tunnel

Two gauges Gauge 1 and Gauge 2 were introduced along the surface of tunnel crown to record the axial and circumferential strains in the numerical analysis. Gauge 1 was located directly below the explosive center on the tunnel surface while Gauge 2 was placed 10.6m away from Gauge 1 as shown in Figure 4.13. Gauge 3 was placed on the springline of the midspan to monitor the circumferential strain in the numerical simulation.

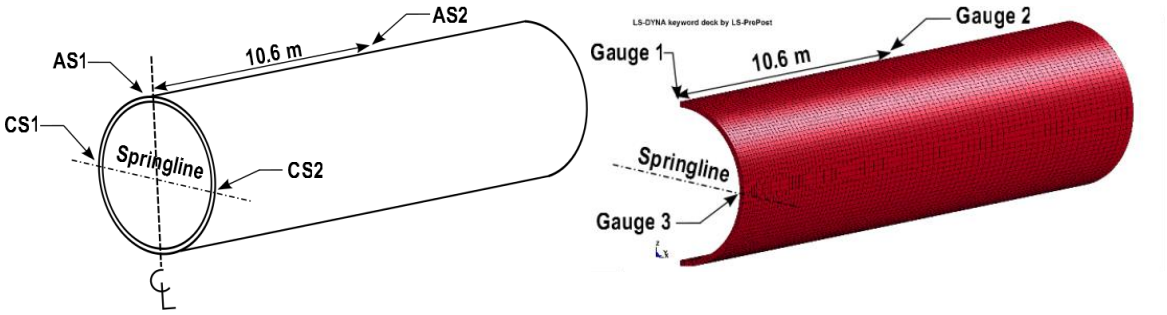

(a) A half-symmetrical prototype tunnel. (b) A quarter-symmetrical numerical model.

Figure 4.13: Arrangement of measuring gauges on the tunnel exterior surface

Studies were performed initially without considering the mesh alignment on the curved contact interface between the soil and tunnel. Interlocking due to peaks and valleys on the interface governed the tunnel response rather than the frictional forces. Interlocking of contact surfaces constrained the tunnel response in circumferential direction as in a perfectly bonded interface. Results reported are not presented here, but the important finding has been used in this numerical simulation to avoid the interlocking of elements. Figure 4.14 shows the time histories of the axial and circumferential strains at the above mentioned Gauge positions. Both plots show that the tunnel response decreases with increase in distance from the explosive, in both axial and circumferential directions, as the intensity of shock wave decays along the tunnel. The plots further indicate that all deformations at gauge points travelled through a peak response cycle over a period of 23ms (1507ms - 1530ms). In this period, the tunnel lost about 90% of peak KE. Therefore, it would be appropriate to say that, this might be the critical period of tunnel response.

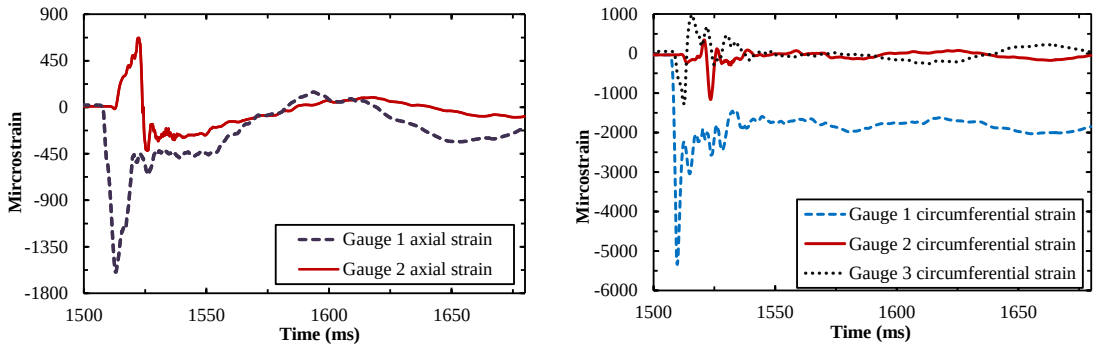

(a) Axial strains (b) Circumferential strains

Figure 4.14: Axial and circumferential strain histories

Furthermore, it is observed in Figure 4.14(a) that most of the axial deformation is recoverable although the response continued with a noticeable fluctuation in axial strain. It is also evident that the circumferential deformation, obtained from gauges 2 & 3, recovered as shown in Figure 4.14(b). However, from the circumferential residual strain at Gauge 1, it is clear that the tunnel suffered permanent deformation due to the surface explosion. This state of strains is reasonable because the tunnel has an infinite surface area in the longitudinal direction which constrained its movement due to the grip in the contact surface between the tunnel and the soil. In the transverse direction, excessive compressive stress from the blast load changed its deformation mode to a horizontal ovalisation. The deformation mode depends on degree of flexibility of the tunnel structure. Due to this, some researchers (Gui & Chien, 2006; Shin et al., 2011) have treated the tunnel response using two dimensional plane-strain analysis by omitting the axial deformation.

The higher value of the circumferential strain at Gauge 1 compared to that at Gauge 3 highlight that the upper part of tunnel above the springline is vulnerable to the explosion. This suggests possible blast mitigation of the tunnel by providing a protective cover on the top half of the tunnel and if tension is evident providing appropriate tensile reinforcement (where necessary) for non-metallic tunnels. Figure 4.15(a) demonstrates how the axial strain varies along the surface of the tunnel crown when Gauge 1 responded to the peak axial strain (deformation) at 1513ms. During this time, as illustrated in Figure 4.12(c), the shock wave front was slightly less than 5.0m away from the midspan of the tunnel. These two figures show that Gauge 1 exhibited the peak axial tensile strain after the shock wave travelled through the target. Propagating shock wave compressed the portion of the tunnel ahead of the shock wave. Furthermore, it displayed a decrease of the axial compressive strain followed by a peak axial compressive strain at 5.0m from the midspan. The compressive zone extended over 5.0m, beyond which there were no significant effect in axial strain. Similarly, Figure 4.15(b) describes the distribution of the circumferential strain along the arc distance away from the top of the tunnel mid-span when the same target was subjected to peak deformation at 1510ms. In this time, propagating shock waves were within an angle of 45^0 from the crown, which can be seen from Figure 4.12(b). The circumferential tensile strain rapidly decreased to a small magnitude at a position of

32.5^0. Due to the globalized vertical in-plane response, the circumferential strain was in tension ahead of the shock wave and it extended even below the springline. Although most surfaces were in tension, the region close to the invert level was slightly in compression.

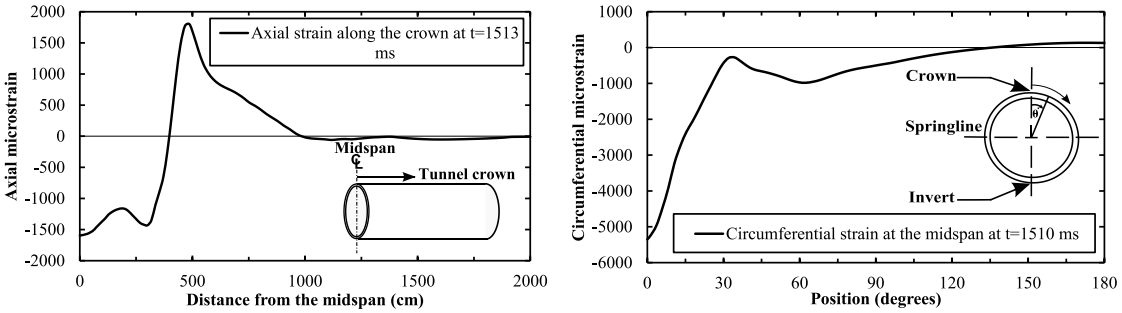

(a) Axial strain distribution along the crown at t=1513ms

(b) Circumferential strain distribution along the arc angle at t=1510ms

Figure 4.15: Deformation of the tunnel during the peak response

Comparisons of the tunnel response with available experimental results of a centrifuge test (De, 2012; De & Zimmie, 2011) were carried out. Figure 4.16 compares the numerical strain history at Gauge 2 with that from the centrifuge test (De & Zimmie, 2011). The proximity of the two curves, with closely matching peaks, indicates a reasonably good correlation between the numerical and the experimental results and provides adequate confidence in the present modelling techniques. Furthermore, in Figure 4.17, magnitudes of peak axial and circumferential strains at Gauge 1 and Gauge 3 respectively, are plotted against the equivalent scaled distance by varying the explosive weight and the soil cover. These strains obtained from the LS-DYNA analysis are compared with those from the centrifuge test (De, 2012) (measured for a specific value of the scaled distance). There is a small discrepancy in the axial strains in Figure 4.17(a), as was also observed in the numerical simulations reported in (De, 2012). This could be due to the uncertainties in the end condition of the pipe and the limitations in its movement in the experiment. A real buried tunnel in a soil medium has no movement restrictions, but the experimental model had restrictions from the four sides of the test-bucket containing the soil. These constrained boundaries may restrict the combined motion of soil and the pipe.

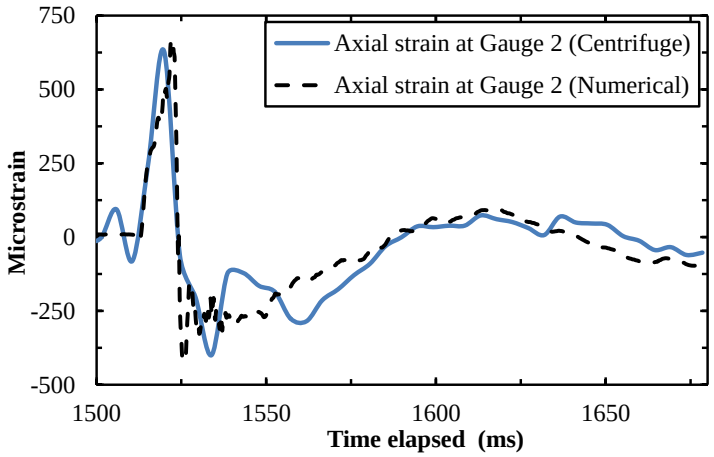

Figure 4.16: Comparison of numerical and experimental axial strains

The circumferential strains at Gauge 3 obtained from the numerical simulations were compared with the experimental results at the two points CS1 & CS2 as illustrated in Figure 4.17(b). These two points are symmetrically located on either side of the springline at the midspan in the experimental setup. The comparisons show that the numerical best-fit line lies between the experimental values at CS1 & CS2. Under symmetric condition of blast loading and the symmetric locations of gauges CS1 & CS2, the peak strains measured in the experiment should be the same at both locations. However, this was not the case and a variation of 280 microstrain was noted. This lack of symmetry and variation in results at CS1 & CS2 could be due to possible movement of the explosive from its initial position inside the test-bucket before the blast occurred or due to a rotation of the copper pipe about its axis during the placement and sand filling into the test-bucket. In centrifuge tests, controlling measures are very difficult to implement, particularly, in blast loading.

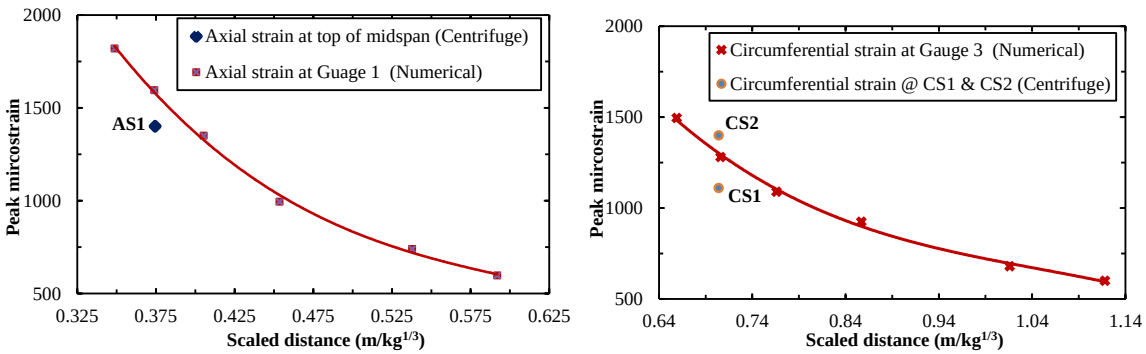

(a) Peak axial strains (b) Peak circumferential strains

Figure 4.17: Comparison of peak axial and circumferential strains

These observations of different circumferential strains at two initially symmetric locations demonstrate the possible movement of the tunnel or explosive during testing and resulting in the actual value of the peak axial strain (at the top of the tunnel at midspan) to be more than the value measured in the experiment. This justifies the higher value of the numerical axial strain compared to the measured value.

4.2.7 Summary

Coupled FSI in ALE technique and material models to analyse the tunnel response to surface blast were validated using previous experimental data of centrifuge test. The main finding of this study can be summarised as follows:

- The axial and circumferential deformations decrease with increasing distance from the explosive, as expected.
- The circumferential strain histories indicate that the upper part of tunnel above the spring-line is more vulnerable to the explosion than the lower part.
- The validated numerical results provide confidence in the modelling techniques used in this study and allow developing rational procedures for predicting the blast response of buried cylindrical structures in dry sand.

4.3 VALIDATION OF SPH SIMULATIONS USING CENTRIFUGE TEST RESULTS

The experiment described in Section 4.2.1 was further simulated using the coupled SPH-FE approach using the same material models as described in the earlier section.

4.3.1 Development of numerical model

As shown in Figure 4.18(b), a portion of the soil experiencing large deformations and the explosive were modelled with SPH particles while the rest of the geometry was modelled with Lagrangian meshes. No attempt was made to model the interior volume of the tunnel. The surrounding outside space of the explosive was assumed to be a vacuum which ignored the later interaction process between the explosion-produced gas and surrounding atmosphere.

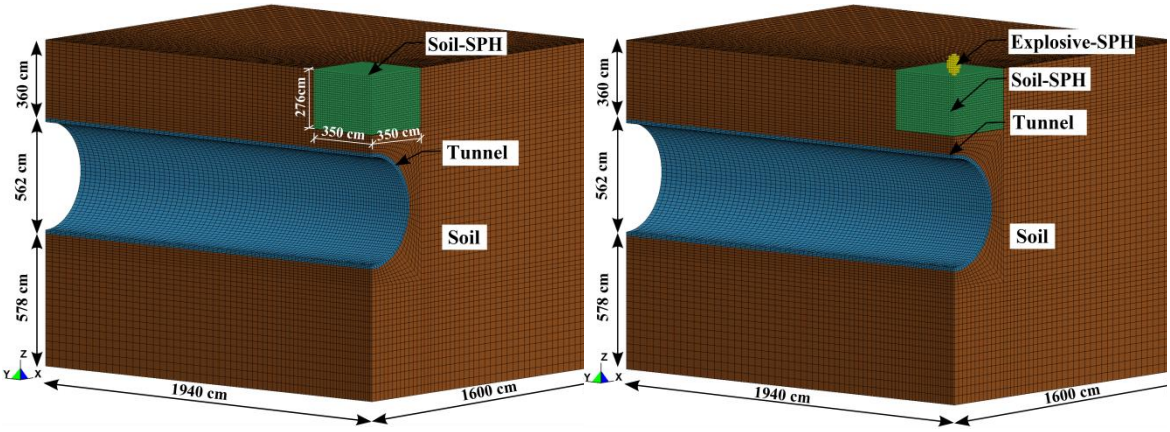

(a) A quarter symmetrical model. (b) Insertion of explosive.

Figure 4.18: Coupled SPH-FE method.

First, a number of models were developed to determine the optimal size of a box filled with SPH soil particles. For a quarter symmetric model, the optimum size of the box was determined as 350cm x 350cm x 276cm. The SPH particles were 10cm in diameter with equal inter-particle distance of 10cm. Beyond the SPH region, the soil and the tunnel were replicated with the same mesh resolution as described in the ALE simulation.

The coupling interaction between the SPH and Lagrange FEM is formed by the penalty based contact CONTACT_AUTOMATIC_NODES_TO_SURFACE. Though the boundary conditions were identical to the ALE model, a special symmetry boundary BOUNDARY_SPH_SYMMETRY_PLANE was applied to those SPH particles at the symmetry planes. The simulation was considered in two stages, stress initialization and blast analysis. The model shown in Figure 4.18(a) was used for stress initialization with a time-dependent mass damping. Upon initializing the model, as illustrated in Figure 4.18(b), the explosive SPH particles were added into the preloaded model for the blast analysis.

4.3.2 Shockwave propagation

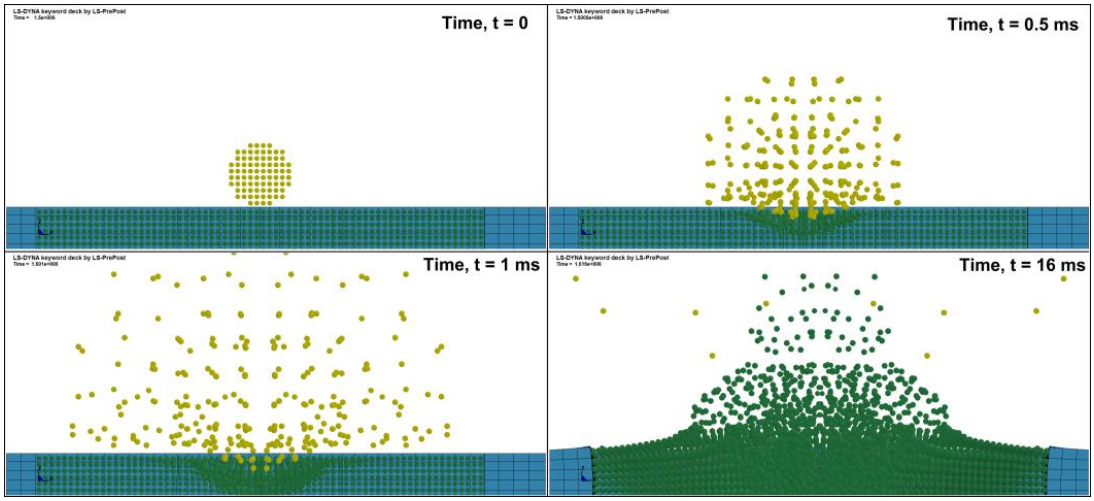

Figure 4.19: Explosive-soil interaction

As illustrated in Figure 4.19, during the explosion process, the quick interaction of the explosive with the neighbouring soil SPH particles implies distortion, where those explosive SPH particles are dispersed by the flow of the expanding explosion. The blast produced shock waves transmitted hemispherically through the soil and propagate at a higher rate than the crater formation as shown in Figure 4.20. The shock waves reached the tunnel crown after 7 ms of the detonation. When SPH particles interacted with solid elements, the SPH-FE coupling enabled the stress transfer at the interface without penetration of SPH particles.

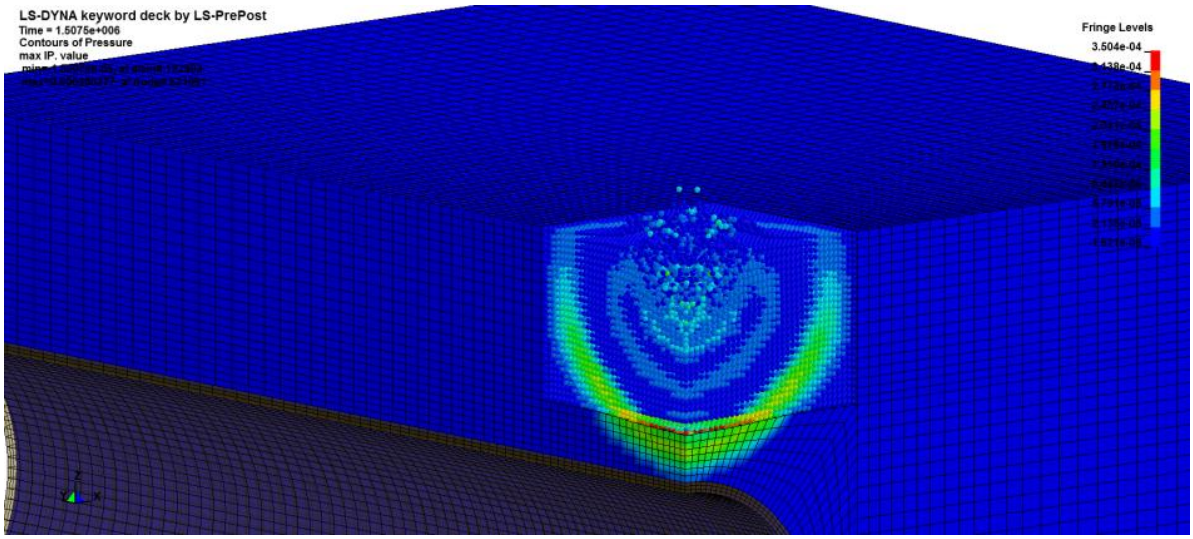

Figure 4.20: Shock wave propagation in soil

4.3.3 Tunnel response

The tunnel response commenced when the shock wave struck the tunnel surface. Figure 4.21 illustrates the interface pressure variation along the tunnel, as the shock waves progress through the soil-structure interface. The interface between the structure and the surrounding soil was simulated using thin-layer elements. Four elements were considered along the crown of the tunnel interface and Figure 4.22 illustrates corresponding interface pressure distributions. The peak interface pressures are high in the immediate area of the explosive. The element EL#32 experienced the highest peak pressure which is more than 600 times the geo-static stress due to the overburden soil. The peak pressure line in Figure 4.22 illustrates that the peak pressure drop is very high in the immediate region whereas the drop is insignificant beyond the region of element EL# 895 which is 4.0m from the mid-span.

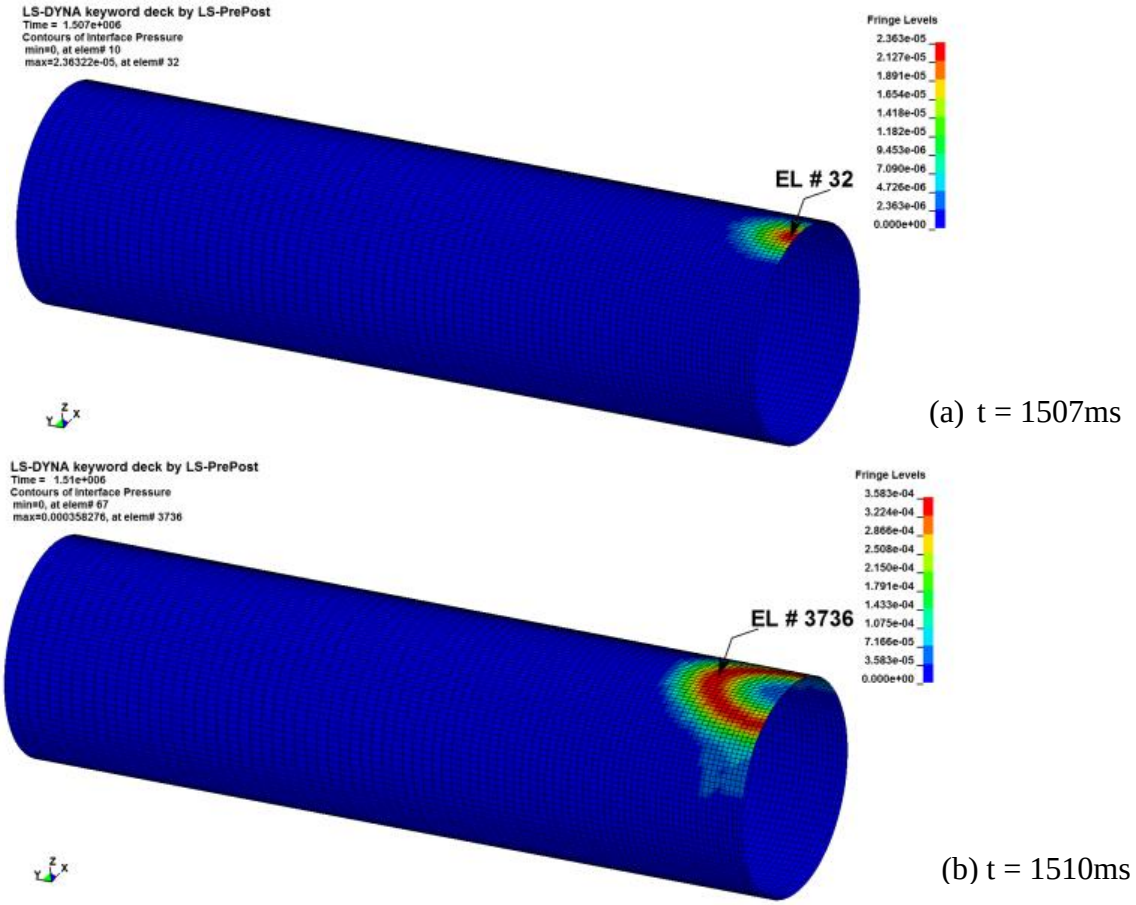

Figure 4.21: Interface pressure contours

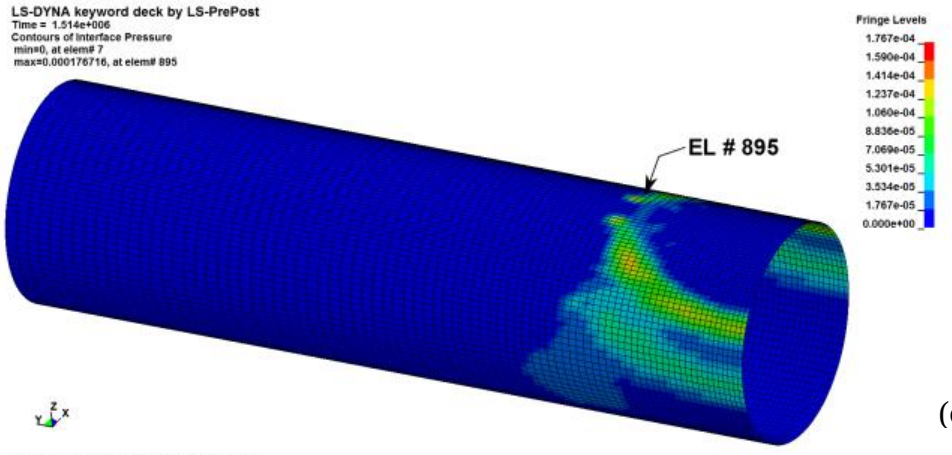

(c) t = 1514ms

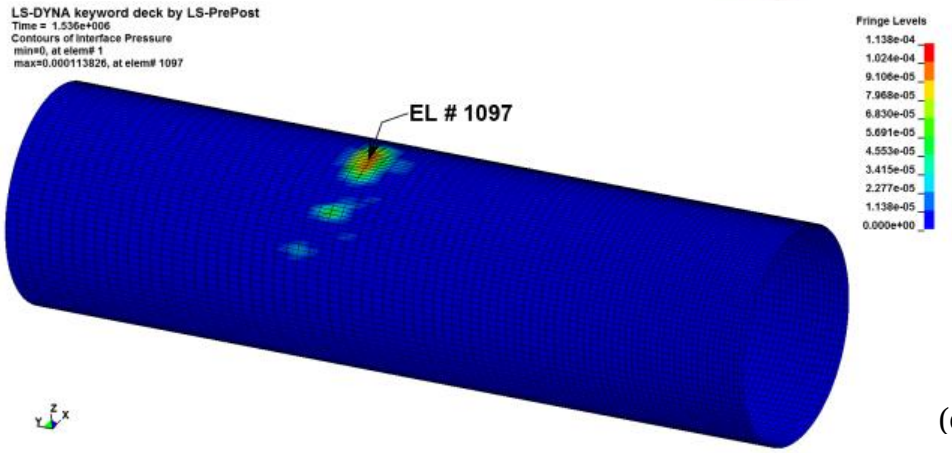

(d) t = 1536ms

Figure 4.21: Interface pressure contours

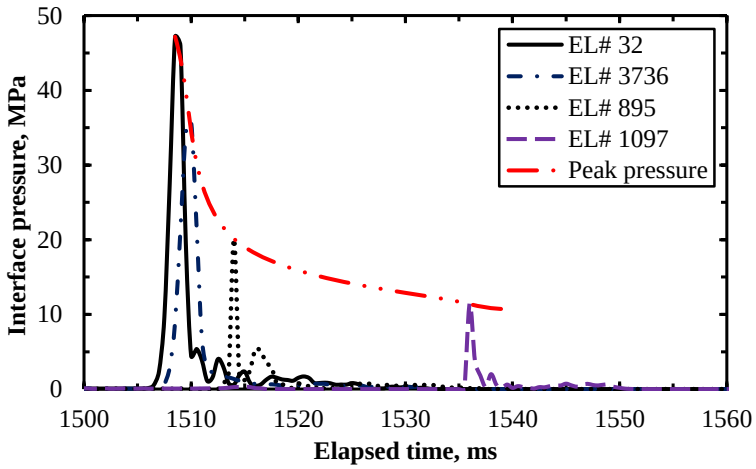

Figure 4.22: Interface pressure vs. time

4.3.4 Comparison of strain output

Figure 4.23 shows a comparison of axial and circumferential strain histories at two locations (Gauge 1 and Gauge 3) obtained from ALE and SPH methods. Figure 4.23(a)

shows that the peak axial strain in the SPH simulation is about 7 per cent more than that in the ALE simulation. General trend of circumferential strain histories are similar as shown in Figure 4.23(b). However, the peak values from the SPH simulations are slightly more than those from the ALE simulations in both the positive and negative phases. After the first peak, there were inconsistent peaks and valleys in the positive phase. This could have resulted from the existing air background mesh in the ALE simulation. Both curves display some fluctuations in strains after 1575ms. Repeated reflection of shock waves caused this fluctuation which continued until the shock waves completely attenuated in the soil.

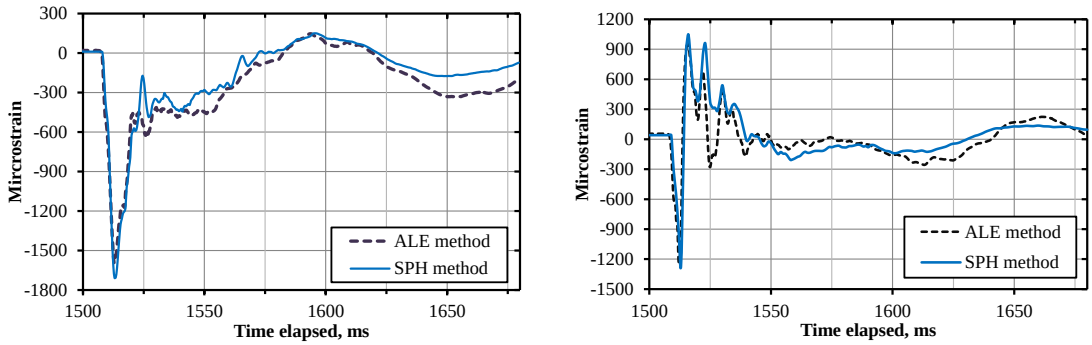

(a) Axial strain at Gauge 1 (b) Circumferential strain at Gauge 3

Figure 4.23: Comparison of axial and circumferential strains.

Figure 4.24 shows the comparison of the numerical strain histories at Gauge 2 with the results from the centrifuge test. The ALE predictions are closer to the experimental results compared to the SPH predictions which were somewhat conservative across most parts of the duration. This could be due to the assumption in the SPH simulation that the surrounding medium of the explosive SPH particles was considered to be a vacuum. This assumption ignored the importance of the interaction of the SPH explosive particles with the air and hence the energy imparted from the explosive into the soil was significantly larger in the SPH simulations than that in the ALE simulations.

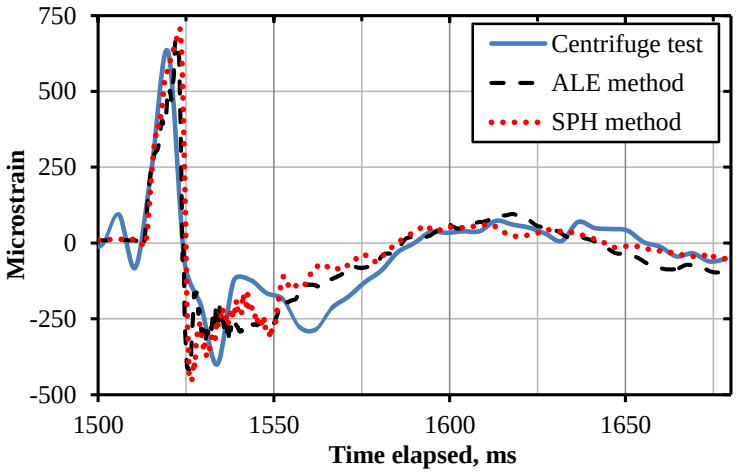

Figure 4.24: Comparison of axial strain from Gauge 2 between simulation and experiment.

Figure 4.25 compares the magnitudes of peak axial strains at Gauge 1 and the peak circumferential strain at Gauge 3 with respect to the equivalent scaled distance of $R/W^{1/3}$ of the explosive. Results for these strains obtained from both ALE and SPH simulations are compared with those from the test data and overall the results from both simulations agree reasonably well with each other and with the test result. Figure 4.25(a) shows that the SPH prediction is slightly (about 7%) higher than the ALE prediction which is closer to the test data. There is however a small discrepancy in the peak axial strain between the test data and the ALE simulation due to the confinement of soil in the test-bucket.

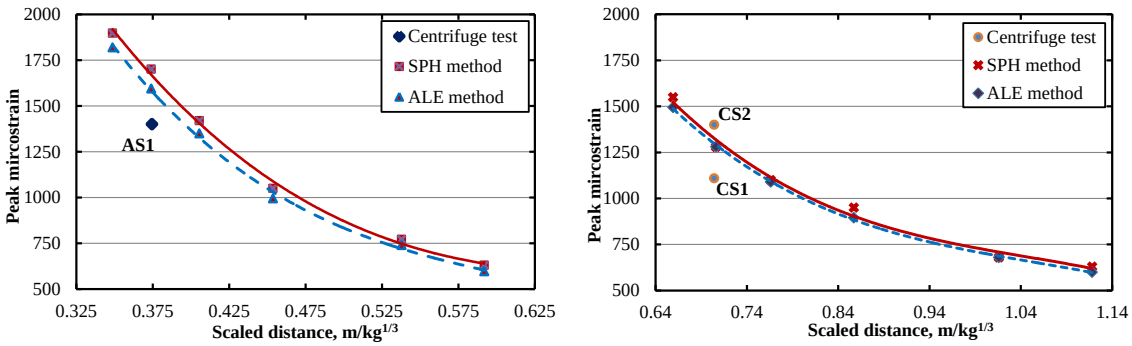

(a) Comparison of peak axial strains (b) Comparison of peak circumferential strains

Figure 4.25: Comparison of peak axial and circumferential strains.

The circumferential strains at Gauge 3 obtained from the numerical simulations are compared with the test data, as illustrated in Figure 4.25(b). The comparisons show that

both numerical best-fit lines are very near and they fall within the range of test data at CS1 and CS2. The test data CS1 and CS2 should be the same for this case with symmetry, but the magnitude of CS2 is 25% more than that of CS1. This could also be another factor that affected the experimental peak axial strain at gauge AS2.

4.3.5 Comparison of computational efficiency

Computer simulations were conducted using nine parallel processors on a standard high performance workstation. Each simulation involved two stages of stress initialization and blast analysis. Table 4.5 shows the comparison of the number of elements and the computational time of both ALE and SPH simulations. The ALE simulation is much faster for the stress initialization than the SPH as the ALE simulation used the Lagrangian structural mesh alone. For agreed mesh resolution, the ALE simulation took slightly more CPU time than the SPH to simulate the blast problem for a period of 180ms.

Table 4.5: Comparison of computational efficiency

	ALE simulation		SPH simulation	
	Initialization	Blast-analysis	Initialization	Blast-analysis
Nos. of Lagrangian elements	220255	220255	213472	213472
Nos. of Eulerian elements	-	307530	-	-
Nos. of SPH particles	-	-	34300	34438
Simulation duration (ms)	1500	180	1500	180
Timestep (μs)	1.06e+01	5.89e+00	1.06e+01	4.72e+00
Total CPU time (hr:min:sec)	10:51:51	164:10:11	96:31:49	142:54:41

4.3.6 Summary

In this section, coupled SPH-FE techniques have been developed and validated for treating the blast response of underground tunnel subjected to surface blast. The coupled

FSI in ALE technique was compared with the coupled SPH-FE technique using the same centrifuge test data. The comparison shows that, in terms of accuracy and computational efficiency, the coupled FSI in ALE outweighed the coupled SPH-FE technique for dealing with above ground explosion problems. The coupled FSI in ALE provides a comprehensive solution in a more efficient manner by handling the numerical model through two different phases which are stress initialization and blast analysis.

4.4 VALIDATION OF ALE SIMULATIONS USING CONWEB TEST RESULTS

This section describes simulations that replicate the CONWEB test (Hayes, 1989) using ALE method in order to validate the response of reinforced concrete slab bolted to the reaction structure.

4.4.1 Description of CONWEB test

A test described in the CONWEB test series (Hayes, 1989) was simulated using the coupled FSI approach in ALE formulation. In this test series, Hayes (1989) considered two low seismic velocity backfill soil materials: a low shear strength reconstituted clay and a high shear strength compacted concrete sand. This simulation utilizes a test with the reconstituted clay which is nearly saturated.

As illustrated in Figure 4.26, the specimen was prepared with a reusable reaction structure which was first placed in an excavated test pit (6.1m x 6.1m x 2.7m). A test slab was bolted to the reaction structure by means of bolts with 22.86 cm spacing along the base and the roof of the reaction structure. The reconstituted clay was backfilled into the pit with a great attention to ensure the consistency of soil properties throughout the backfilling. During the backfilling, a series of interface pressure gauges were fixed on the right side of the charge to monitor the free-field motion of the soil as shown in Figure 4.26. The test slab was also instrumented with interface stress gauges on the exterior face to monitor the interface pressure as well as accelerometers on the interior face to measure horizontal motion. A 7kg C-4 cased cylindrical explosive was placed 152.4cm away from the center of the test slab at a depth of 152.4cm.

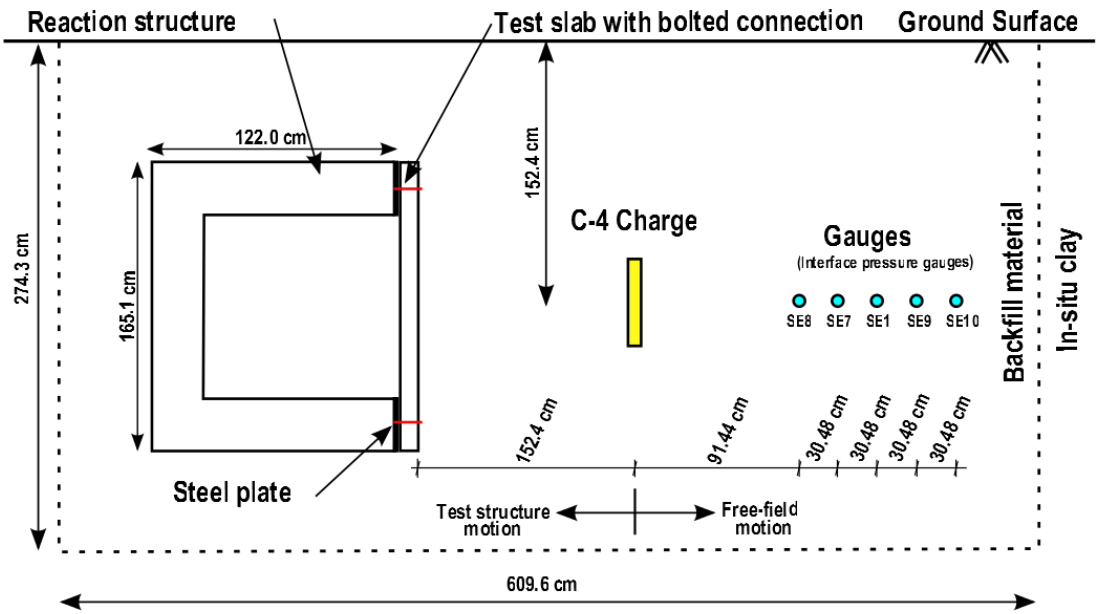

Figure 4.26: Experimental setup of CONWEB test (elevation) (Hayes, 1989)

The test slab was 4.57m in length, 1.65m high and 10.9cm thick, reinforced in both vertical and horizontal directions with adequate shear links. The reinforcement and concrete cover details can be found in Hayes (1989). The density and average unconfined compressive strength of the test slab concrete were 2.24g/cm^3 and 42.0MPa respectively. The reaction structure was a 28cm thick heavily reinforced concrete box open on one side to mount the test slab. The exposed surface of the reaction structure was cast with a 16mm thick steel plate which provided a hard smooth bearing interface and performed as a protective layer against the blast impact.

4.4.2 Development of numerical model

The numerical model composed of mainly four components consisting of a buried explosive, soil, air and the test structure. Symmetric modelling capabilities played important roles in this simulation by reducing the computational demand in terms of the problem size. Therefore, a quarter of each of the soil and explosive and a half the structure were modelled as shown in Figure 4.27.

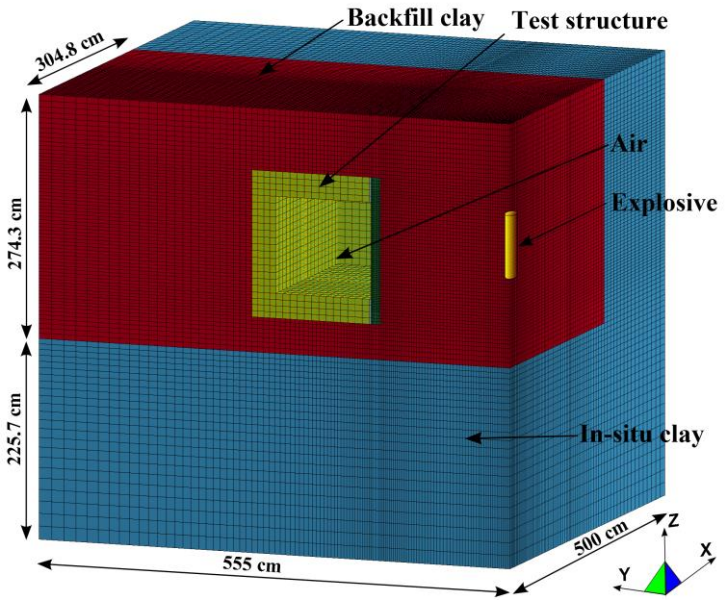

Figure 4.27: A half symmetry numerical model for ALE simulation

The reaction structure and the test slab were modelled using the eight-node hexagonal solid elements with Lagrangian meshes. The soil and air within the interior volume of the structure were modelled using the eight-node hexagonal solid elements with Eulerian meshes. The cylindrical explosive was defined into the soil mesh using INITIAL_VOLUME_FRACTION_GEOMETRY by specifying its radius, height and detonation point. A series of mesh sensitivity studies provided an appropriate mesh refinement to capture the detonation process and subsequent response of the structure. The soil was refined with a gradual increase in mesh size in both X and Y directions from the explosive center. The size of the smallest element in the central part of the explosive was 2.25cm x 2.25cm x 3.0cm. The interface between the backfill soil and the in-situ clay were modelled with merged nodes. Since material properties were not available for the in-situ clay, it was assumed to be the same as the backfill material.

In the simulation, a fully coupled FSI approach combining both Lagrangian and Eulerian solvers was adopted to allow for the incorporation of the essential processes using CONSTRAINED_LAGRANGE_IN_SOLID. Nodes in the symmetry boundaries of XZ and YZ planes were constrained in their normal directions. The bottom of the mesh was modelled as fixed in all directions. Along the infinite boundary of the entire computational domain, non-reflecting boundaries were set as a flow out boundary to avoid shock wave reflection.

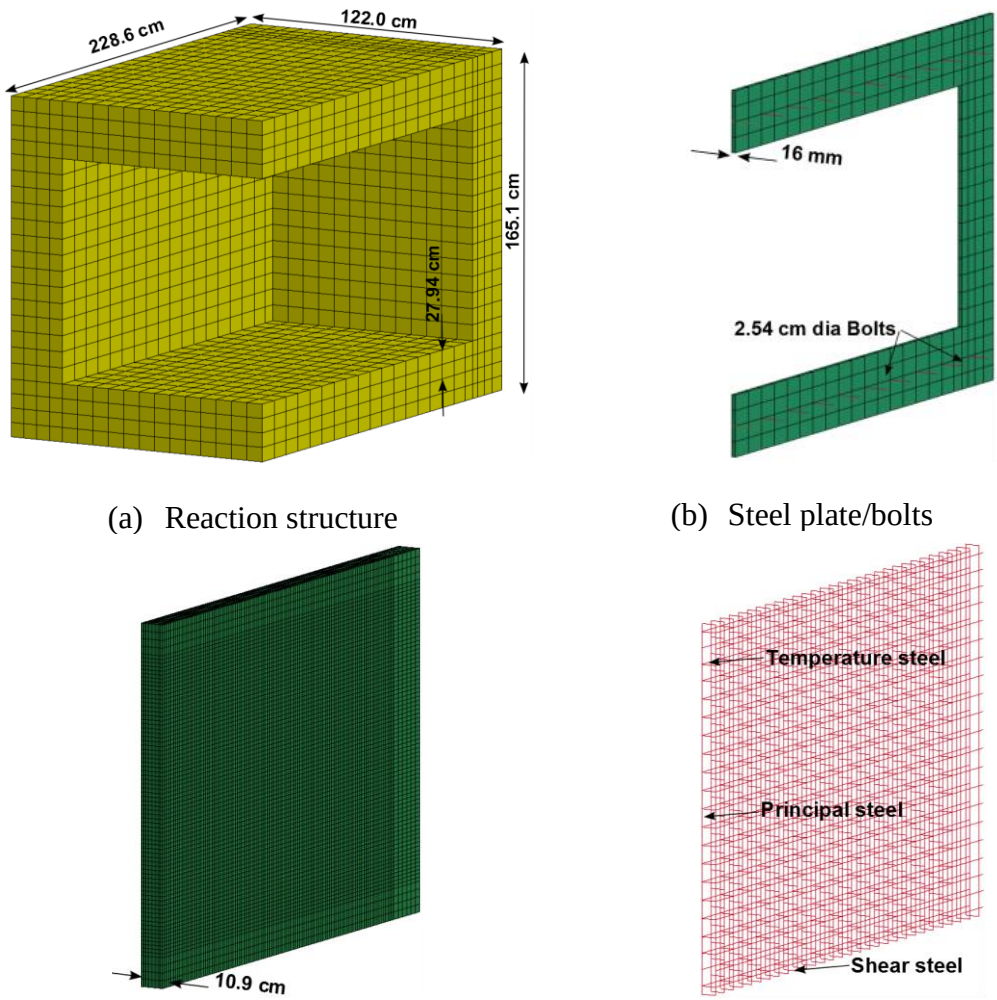

(a) Reaction structure (b) Steel plate/bolts

(c) Test slab (d) Reinforcement

Figure 4.28: Test structure components

Figure 4.28 illustrates half the test structure components which were modelled with appropriate boundary conditions at the symmetry planes. The reinforcement details described in the CONWEB test (Hayes, 1989) was simulated in the model. The reinforcement steel and bolts were modelled using Hughes-Liu beam elements (LSTC, 2007) with cross sectional integration. The test slab was modelled with a very fine mesh to achieve adequate accuracy in the deflection. A minimum of two hexahedral elements were specified for the reinforcement cover. There were 72960 solid elements in the test slab attached to the steel plate with 20 bolts. The simulation was free from pretension in bolts. In the test slab, reinforcing beam elements and bolts were modelled as discrete elements immersed in the slab meshes using the CONSTRAINED_LAGRANGE_IN _ SOLID coupling. In the steel plate, the same nodes were shared for a perfect bond

between the steel plate and bolts. The CONTACT_AUTOMATIC_SINGLE_ SURFACE contact was also used to define the interface between the test slab and the steel plate.

As the steel plate was cast integrally together with the reaction structure, the perfectly bonded 'no slip' condition was simulated between the steel plate and reaction structure. The material properties for the steel plate were specified by Bessette (2004) and the steel was modelled with MAT_PLASTIC_KINEMATIC material model. The reaction structure was a heavily reinforced thick concrete structure (Hayes, 1989). Since there were no reinforcement details available, for simplicity, the reaction structure was modelled as a smeared concrete as also adopted by others (Yang et al., 2010).

4.4.3 Material models and parameters

The material models and relevant material properties for the air and explosive were described in Chapter 3.5. The soil properties such as density, specific gravity and water content are shown in Table 4.6. The shear and bulk moduli were evaluated based on the density, seismic velocity and Poisson's ratio (Bessette, 2004). The cohesion and friction angle were selected based on the modified material properties described by Baylor (1992). Magnitudes of PWD_1 were estimated based on best fit material analysis using the free-field blast simulation reported in CONWEB test series.

Table 4.6: Material properties of backfill materials

Parameters	Reconstituted clay	Compacted concrete sand
Density (g/cm^3)	1.96	1.865
Specific gravity	2.71	2.70
Shear modulus (MPa)	20.0	70.2
Bulk modulus (MPa)	193.3	117.0
Cohesion (MPa)	2.275e-02	3.723e-02
Friction angle	22^o	40^o
Moisture content (%)	23.3	5.0
PWD_1 (MPa^{-1})	4.810e-03	2.520e-02
PWD_2 (MPa^{-1})	4.974e-02	1.152e-02

Table 4.7 shows the material parameters of concrete adopted in the simulation of CONWEB tests. The fracture energy for the concrete containing limestone aggregate, used in the experiment, was considered as 70N/m (Darwin et al., 2001). The material properties of the steel are described in Table 4.8.

Table 4.7: Material properties of concrete

Parameter	Test slab (Test with clay)	Test slab (Test with sand)
Density (g/cm^3)	2.24	2.24
Unconfined compressive strength (MPa)	42.0	40.4
Poisson's ratio	0.19	0.19
Maximum aggregate size (mm)	9.5	9.5

Table 4.8: Material properties of steel reinforcement

	Density (gcm^{-3})	Es (GPa)	ν	σ (MPa)	E_{tan} (GPa)	β	C (S^{-1})	P
Principal steel	7.85	200	0.3	465	2.0	0	1080	5.48
Temperature steel	7.85	200	0.3	563	2.0	0	9650	5.50
Shear steel	7.85	200	0.3	505	2.0	0	2150	5.49

4.4.4 Free-field simulation

Figure 4.29 compares the peak pressure attenuations obtained from the free-field simulation with those from the CONWEB free-field test (Hayes, 1989) for saturated reconstituted clay. For a magnitude of PWD_1 (= $6.30GPa^{-1}$), numerical results are only marginally lower than those from the experiment in the immediate vicinity of the charge (152.4cm away from the charge center). As distance increases form the charge, the numerical values become slightly higher than the experimental values. This could be due to the confinement effect of the charge. The casing of the charge was not considered in the simulation which used a bare charge. The proximity of the two curves, however, demonstrates a reasonable agreement between the present numerical results and the measured free-field peak pressures. It can be seen that the shock pressure attenuation for the reconstituted clay was not aligned with a linear power law on a logarithmic scale. As

highlighted by Yankelevsky et al. (2011), behaviour of some types of soil may be represented by either bi-linear or tri-linear trend lines. As the numerically obtained free-field response reasonably agreed with that from the experiment, it provided a means to evaluate the best fit PWD_1 constant for the saturated reconstituted clay as $6.30GPa^{-1}$.

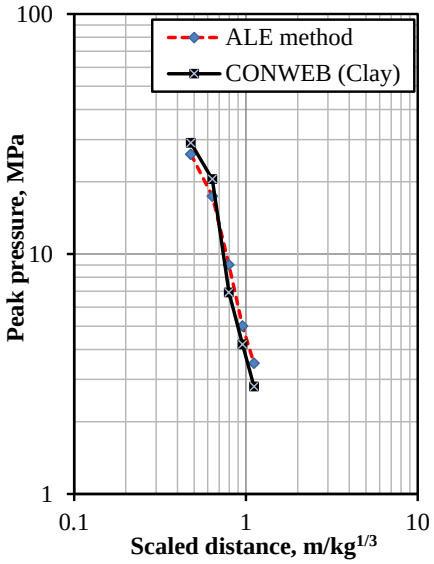

Figure 4.29: Comparison of peak pressures

4.4.5 Test slab response

The response of the test slab under buried blast was investigated. Figure 4.30 shows the progress of the slab deformation as the shock wave travels through the structure over 20ms of duration. After igniting the explosive at 300ms, blast induced shock waves travelled through the soil and compressed the test slab surface. The shock wave front impacted the exterior surface of the slab at 303.1ms.

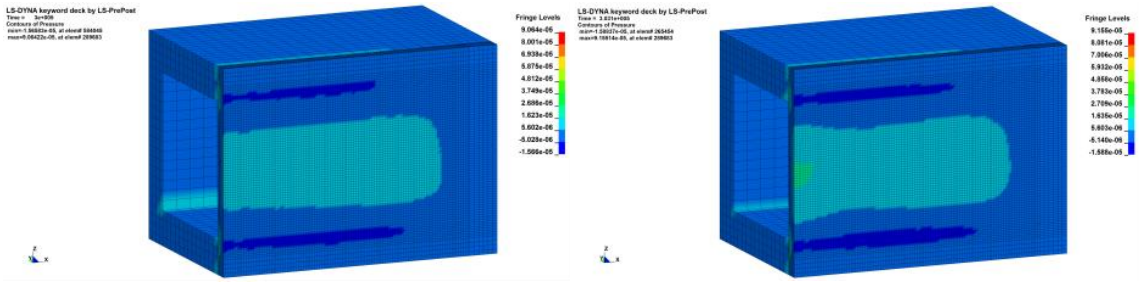

(a) t = 300ms (b) t = 303.1ms

Figure 4.30: Progress of test slab deformation

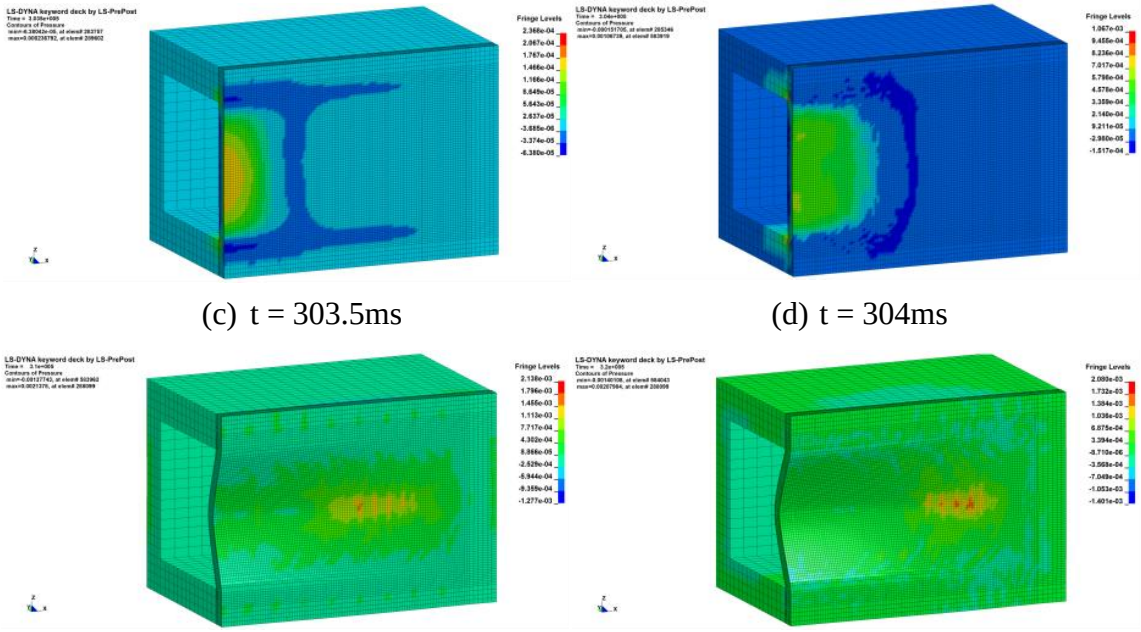

(c) t = 303.5ms (d) t = 304ms

(e) t = 310ms (f) t = 320ms

Figure 4.30: Progress of test slab deformation

The slab displayed some kind of breaching failure at the center and the failure extended away from the center, as the shock wave progressed through the slab. Before the reinforcement bars near the center of the slab failed, those at the top and bottom support edges broke due to both tensile failure and shear failure mechanisms. Figure 4.31 displays the broken reinforcement at the end of the simulation. The observed damages in the reinforcement are similar to the experiment as described by Hayes (1989). Along the exterior edges of the support, there was a series of separation between the slab and steel plate due to both localized rotation and deformation of bolts.

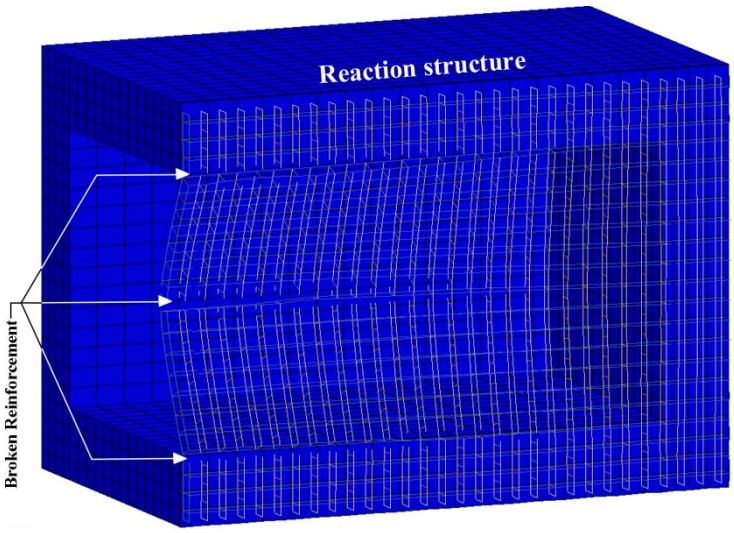

Figure 4.31: Broken slab reinforcement

Crack opening capabilities in the concrete material model illustrate the failure or damage in the slab. Cracks first appeared in both interior and exterior surfaces after 4ms of the explosion as shown in Figures 4.32(a) and 4.32(d). These figures show that most of the damage of the test slab resulted within a very short period of time from the excessive impact of blast pressure. During the early stages of the simulation, cracks were vertical and parallel to the principal steel. Later on a number of diagonal cracks initiated on the interior slab surface. At later stages, large number of diagonal cracks emanated from the bolt points which act as a stress initiating points from the deformation mechanism. The interior and exterior views of the slab damages, cracks patterns and deformed shapes at the end of the simulation are similar to those observed in the CONWEB test (Hayes, 1989).

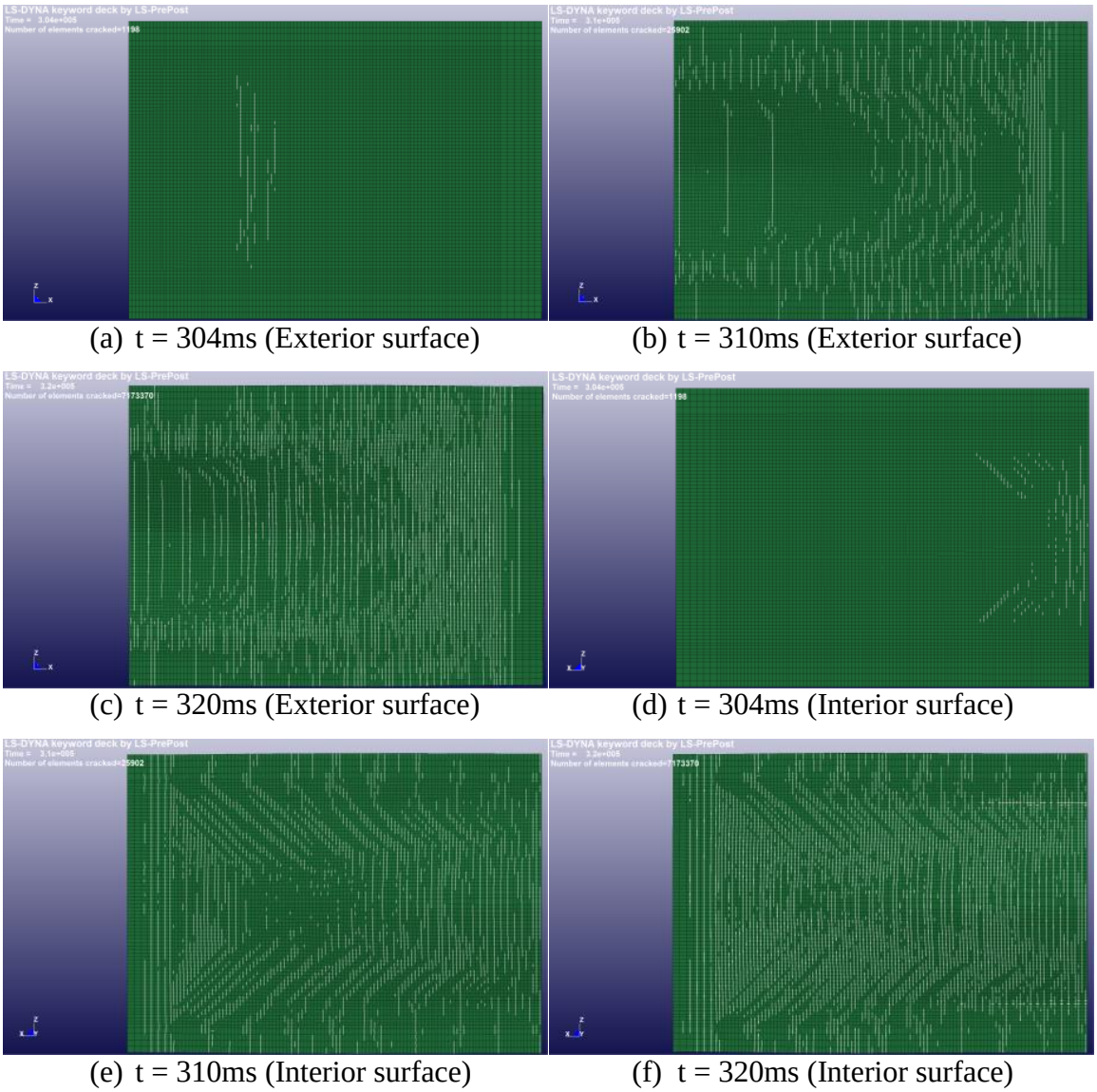

(a) t = 304ms (Exterior surface) (b) t = 310ms (Exterior surface)

(c) t = 320ms (Exterior surface) (d) t = 304ms (Interior surface)

(e) t = 310ms (Interior surface) (f) t = 320ms (Interior surface)

Figure 4.32: Propagation of cracks on test slab surfaces

In order to compare the displacement history of the slab with the results from the CONWEB test, six gauges mounted on the slab surface are considered. Figure 4.33 describes the interior view of the slab and gauges. Gauge AHS-2 is close to the center of the slab and gauges AHS-1, AHS-0 and AHS-3 are vertically aligned with ASH-2 on the center line of the slab. Gauges AHS-1, AHS-5 and AHS-6 are on a horizontal line which is about 19cm below the slab center.

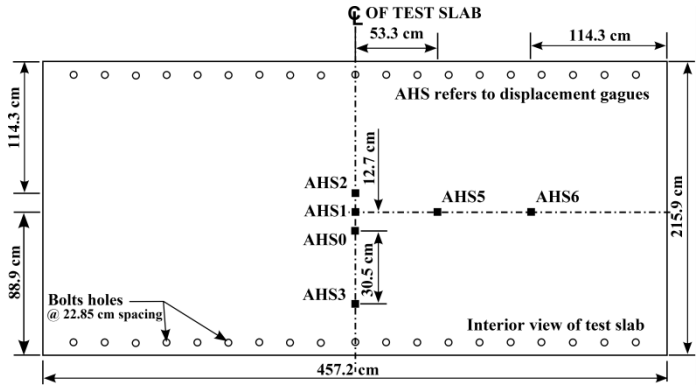

Figure 4.33: Instrumentation plan of test slab (Hayes, 1989).

Figure 4.34 compares the present results for displacement histories at the six gauges with those from the CONWEB test (Hayes, 1989). It shows that the numerical simulations of the displacements compared well with the corresponding experimental displacements and are within the deviation limits with few exceptions. At first, a small lag in the time of arrival of shock wave was observed in the simulation. This could be due to the small deviation in soil material properties evaluated based on several assumptions and empirical formulae. Secondly, comparisons clearly show that displacement-time responses are slightly steeper during the first half of the simulation. The displacement-time response is dependent on the Young's modulus of the concrete used in the CONWEB test (Hayes, 1989) where the concrete was made with a limestone aggregate. Since there are no records of stress-strain relationship available for the concrete containing limestone aggregate, Young's modulus used in the present simulation was evaluated based on Equation 3.17. As highlighted by Oluokun et al. (1991), this equation predicts less accurate values of the Young's modulus.

Along the transverse direction at gauges AHS-1 and AHS-5 numerical predictions are reasonably close to the experimental values, but at AHS-6 they seem to diverge with

time. The reason for this discrepancy is unclear and it was also observed in the numerical simulation reported by Bessette (2004). Numerical predictions are also reasonably close to the experimental values along the vertical center line of the slab, except at AHS-2 where there is over-prediction of the results. This was also observed by Bessette (2004). By comparing experimental displacements from surrounding gauges, this variation at AHS-2 could be due to possible disturbance of the gauge caused by excessive cracking near the center of the slab. Overall, the numerical displacements are reasonably close to the experimental values at many locations. The numerical results of reinforcement bar failure, crack patterns in the slab and slab deflections agree reasonably well with those from the experiment and provide adequate confidence in the present modelling techniques.

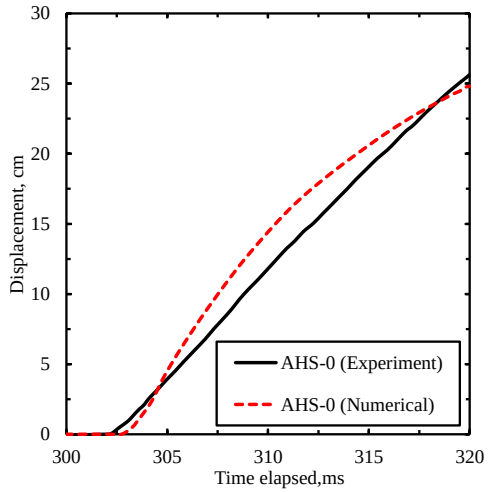

(a) AHS-0

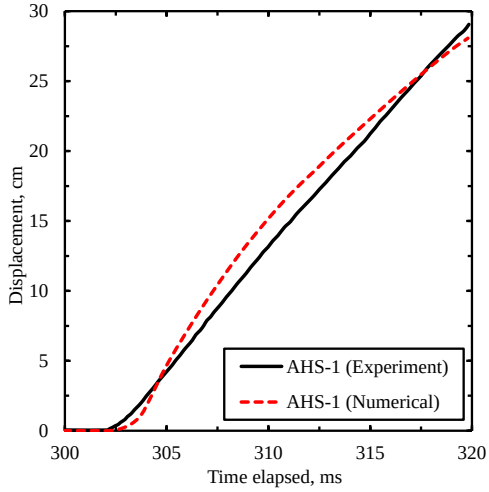

(b) AHS- 1

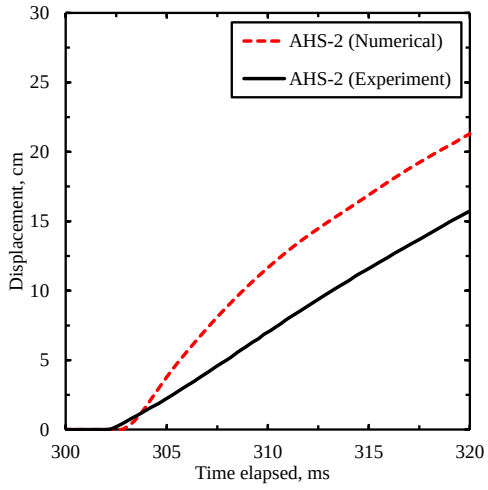

(c) AHS-2

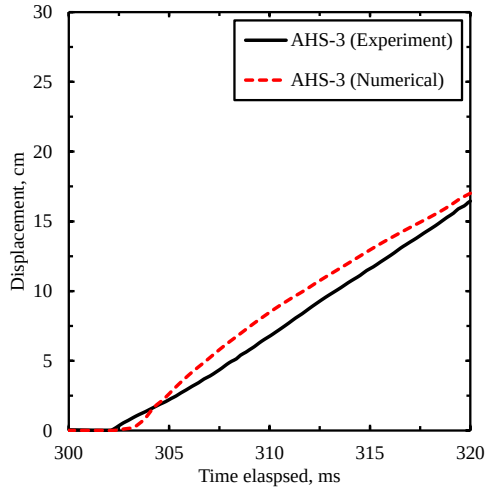

(d) AHS-3

Figure 4.34: Comparison of displacements

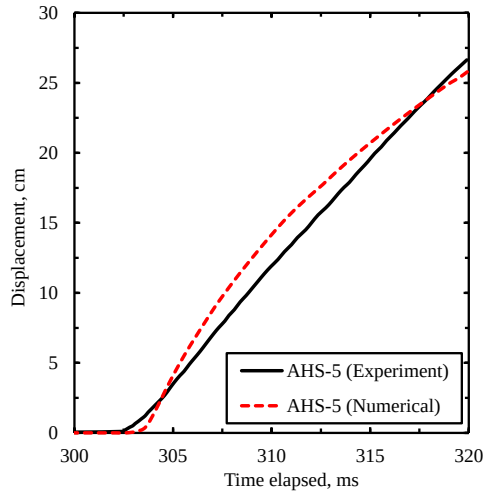

(e) AHS-5

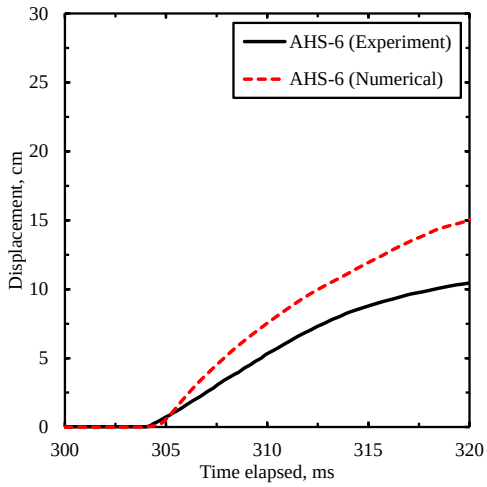

(f) AHS-6

Figure 4.34: Comparison of displacements

4.4.6 Summary

In this section, the coupled FSI in ALE technique and material models to analyse the underground structural response to belowground explosion was validated using CONWEB test. The result shows that the simulation agreed reasonably well with the experiment in the aspects of reinforcement bar failure, crack patterns in the slab and slab deflections.

4.5 VALIDATION OF SPH SIMULATIONS USING CONWEB TEST RESULTS

This section simulated CONWEB test (Hayes, 1989) using SPH method in order to validate the response of the same reinforced concrete structure buried in partially saturated sand.

4.5.1 Development of numerical model

Similar to the model in Section 4.4.2, a quarter symmetric model was utilised as shown in Figure 4.35. The explosive and near field soil media were modelled using SPH particles while the far field soil and the test structure were modelled using the eight-node hexagonal solid Lagrangian elements.

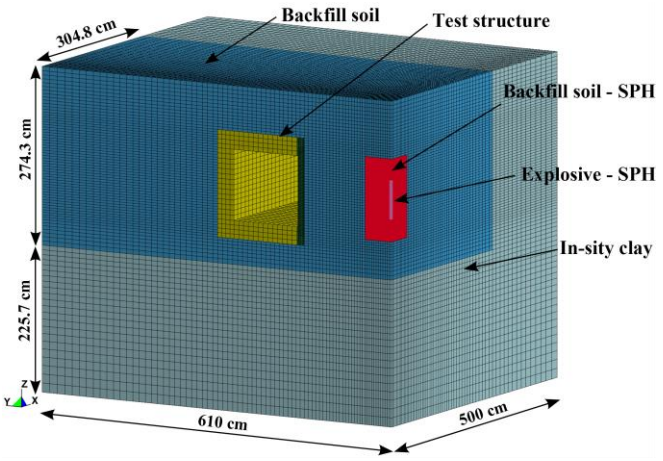

Figure 4.35: A half symmetrical numerical model for SPH simulation

All SPH particles within a box of 46.5cm x 46.5cm x 127.5cm were modelled with an equal inter-particle distance of 1.5cm. A series of mesh sensitivity studies provided an appropriate mesh refinement to capture the detonation process and subsequent response of the structure. The soil was refined with a gradual increase in mesh size in both X and Y directions beyond the SPH region. The size of the smallest element adjoining the SPH region was 3.7cm cube. Backfill soil elements were merged with the in-situ clay soil elements at the interface. Since material properties were not available for the in-situ clay, it was considered to be the same as the backfill reconstituted clay. This will avoid any problems with the wave refraction/reflection at the interface as both backfill materials have the same seismic velocity.

The same modelling procedure as described in Section 4.4.2 was used to model the test structure. The interface between the test structure and the backfill soil was modelled using CONTACT_AUTOMATIC_SURFACE_TO_SURFACE contact. Section 4.4.3 described the soil properties for the backfill compacted sand used in this simulation.

4.5.2 Free-field simulation

Free-field analysis was performed to evaluate a best fit material parameter of PWD_1. In this numerical simulation, the charge was modelled using SPH particles without the casing as SPH is incapable of modelling shell elements. Figure 4.36 shows the comparison of peak pressure from the present numerical study with those from the CONWEB free-field test (Hayes, 1989) for partially saturated sand. It can be seen that

the best fit line of the sand has a perfect match with the measured free-field peak pressure and it also complies with a linear power law on a logarithmic scale. Hence the free-field simulation agreed reasonably well with the test results and provides a means to evaluate the best fit PWD_1 parameter for the partially saturated sand as $25.0GPa^{-1}$.

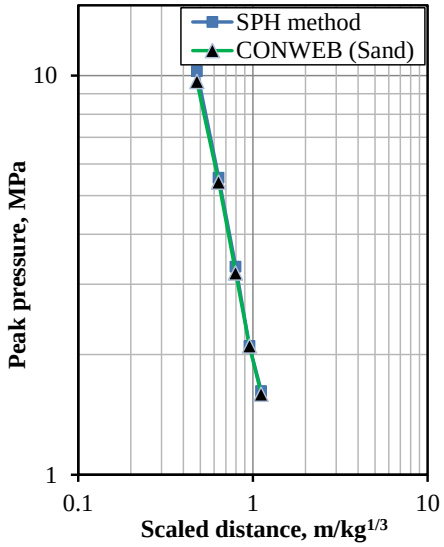

Figure 4.36: Comparison of peak pressures

4.5.3 Test slab response

The structure began to respond when the shock waves reached the soil structure interface. Figure 4.37 illustrates the variation of interface pressure contours at the interface of the soil structure.

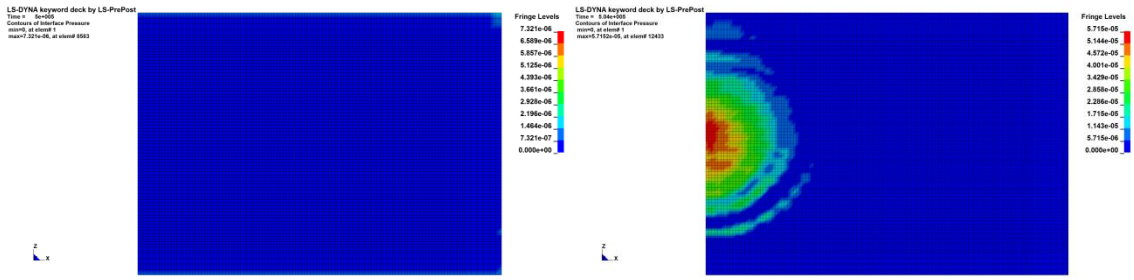

(a) t = 500ms (b) t = 504ms

Figure4.37: Interface pressure contours

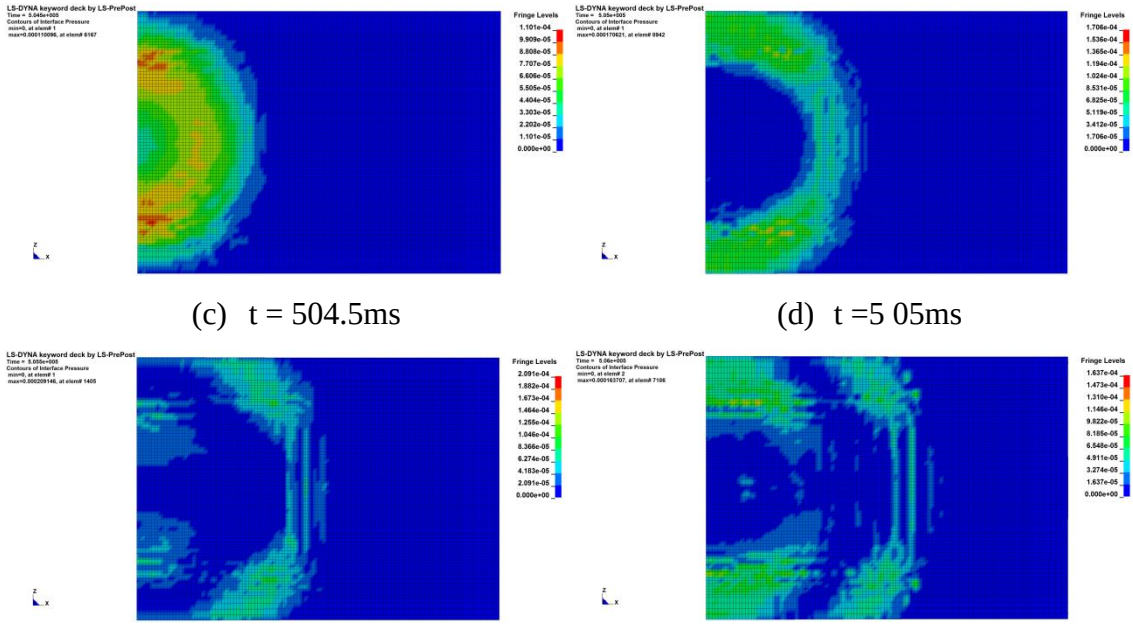

(c) t = 504.5ms (d) t =5 05ms

(e) t = 505.5ms (f) t = 506ms

Figure 4.37: Interface pressure contours

The peak pressure which results from the interaction of the structure and the surrounding soil is the dominant parameter that influences the response of the test slab. This peak interface pressure was therefore considered in the present study. Figure 4.38 compares the peak interface pressures with those obtained from the CONWEB test. The peak pressures evaluated by using the Winfrith concrete model agree better with those from the experiment at many locations.

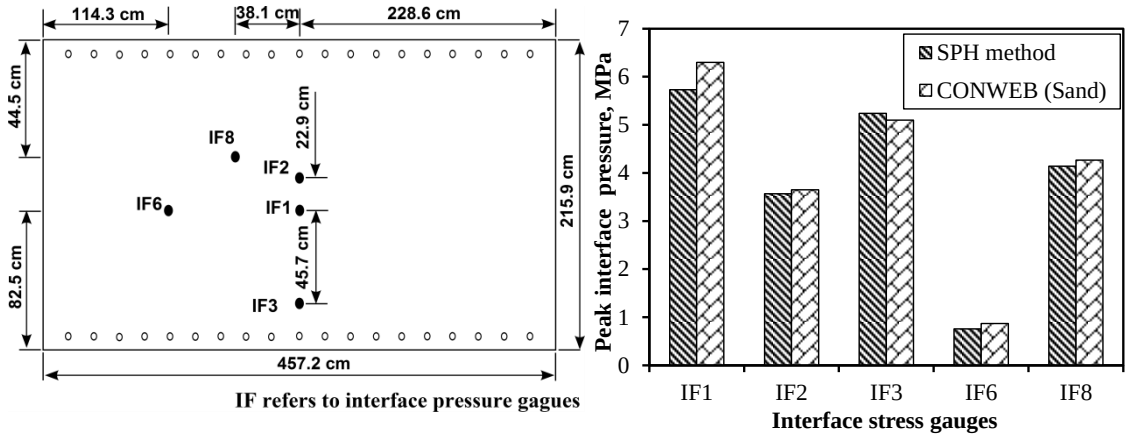

(a) Exterior surface of test slab (b) Interface peak pressure

Figure 4.38: Comparison of peak interface pressures

The response the test slab under blast load was investigated. The simulation showed a kind of breaching failure at the center of the test slab and the failure extended away from the center. Shear failure was observed at the end support along the floor and roof edges of the reaction structure. A separation between the test slab and steel plate was also observed due to both localized rotation along the support edges and straining of bolts. Figure 4.39 illustrates the formation of cracks in the test slab. During early stages of the simulation, cracks were vertical and parallel to the principal steel. At later stages of the simulation, number of diagonal cracks emanated from the bolt locations. Comparisons of the interior view of the test slab damage (Hayes, 1989) and numerical simulations illustrate that the damage patterns at the interior face of the slab are similar in terms of qualitative assessment.

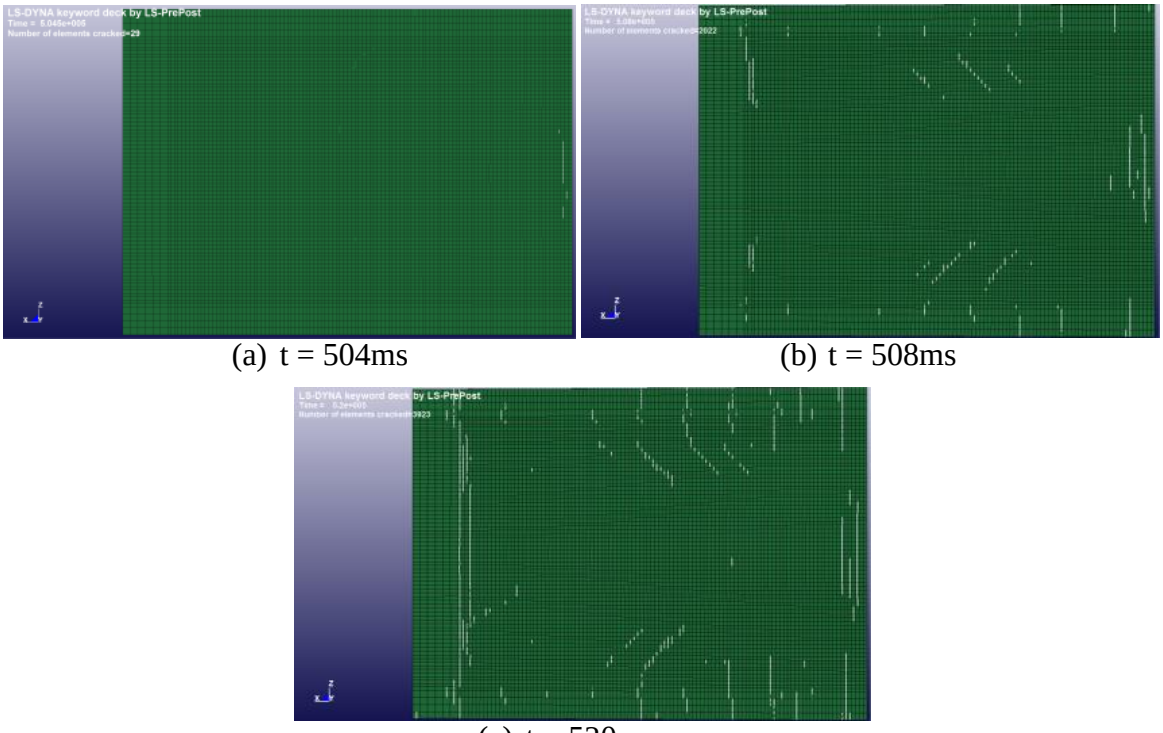

(a) t = 504ms (b) t = 508ms

(c) t = 520ms

Figure 4.39: Propagation of cracks on interior surface

Finally, the displacement histories of six gauges are compared as shown in Figure 4.40. The slight lags in the time-of-arrival are similar to those observed in the earlier simulation. Though the deflections obtained from the simulation were less than those observed in the experiment, the predictions of final displacements were closer to the experimental results at many locations. Overall, the experimental results such as the

interface pressure, crack propagation and deflection obtained from for this configuration agrees well with the chosen concrete model.

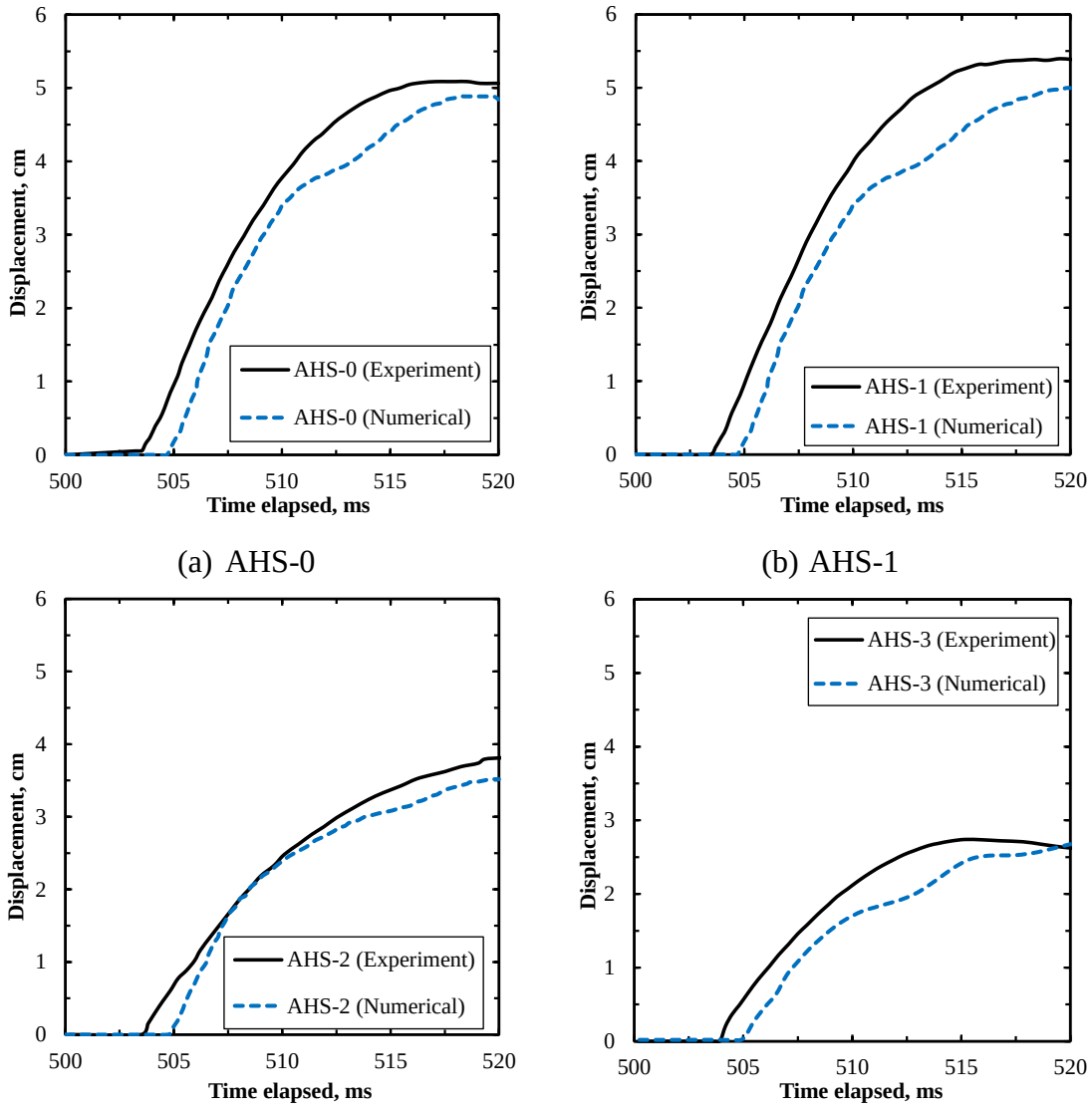

(a) AHS-0 (b) AHS-1

(c) AHS-2 (d) AHS-3

Figure 4.40: Comparison of displacements

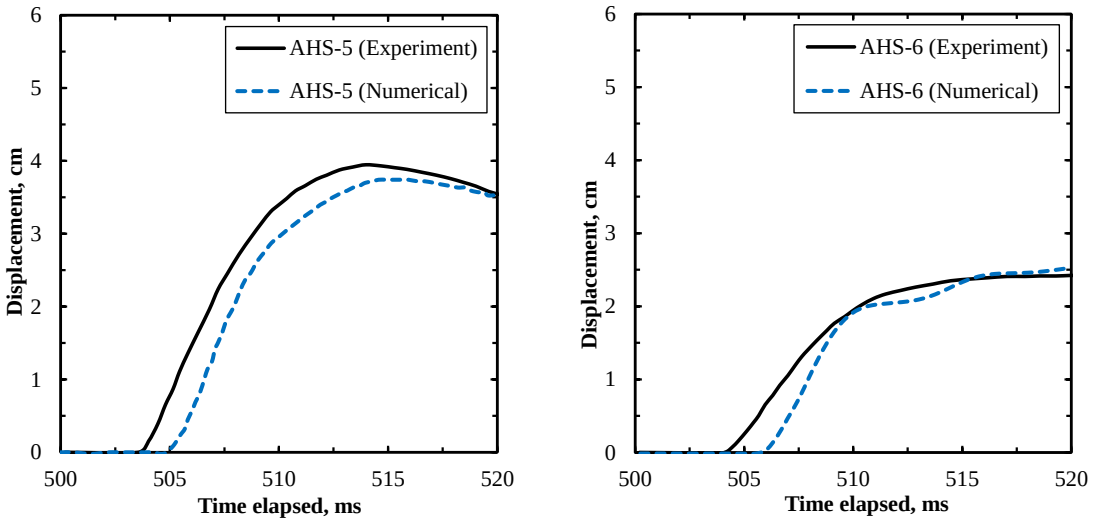

(e) AHS-5 (f) AHS-6

Figure 4.40: Comparison of displacements

4.5.4 Summary

In this section, the coupled SPH-FE technique and material models to analyse the underground structural response to belowground explosion were validated using the CONWEB test. The results show that the simulation agreed reasonably well with the experiment in the aspects of interface peak pressure and crack patterns in the slab, although the simulation slightly under-predicted the displacement response at few locations.

4.6 CHAPTER SUMMARY

This chapter demonstrates the applicability of the state of the art of numerical techniques to accurately predict the blast-induced buried structure response. The validation of numerical techniques for the prediction of the tunnel response to aboveground (surface) and belowground explosions has been presented in this chapter. Two different numerical techniques (i) coupled FSI in ALE and (ii) coupled SPH-FE techniques have been developed and applied for treating the blast response of buried structures using the software LS-DYNA. The modelling techniques were compared for the surface-blast induced tunnel response in dry soil and validated using results from the centrifuge test (De, 2012; De et al., 2013). For aboveground surface explosion and subsequent response of buried tunnels, the coupled FSI in ALE outweighed the coupled SPH-FE technique in terms of accuracy and computational efficiency. Validation of

reinforced concrete model and contact between two structural elements connected by bolts was performed using CONWEB tests (Hayes, 1989) in both numerical techniques.

The results confirmed the validity of the ALE modelling techniques, reliability in employing material models and their applicability to extend the study to treat the blast response of segmental buried tunnels. The remaining chapters of the thesis employed the ALE modelling techniques to investigate the influence of important parameters on the blast response of segmental tunnels.

Chapter 5: Effect of segments on the blast response of buried tunnels

5.1 INTRODUCTION

Numerical techniques validated in the previous chapter provide confidence in investigating the response of segmented bored tunnels subjected to surface blast. The previous chapter revealed that ALE modelling technique in LS-DYNA is a suitable platform for the modelling of the surface blast response of buried structures. A common single tube railway tunnel system with six identical rectangular segments (RS) spanning the circumference of the tunnel is simulated by using fully coupled ALE modelling techniques as described in Chapter 4. Two types of segments, hexagonal segments (HS) and interlocking segments (IS), are considered to study their effects on the dynamic response of bored tunnels subjected to surface blast. The effect of explosive weight on the blast response is also considered. The chapter first describes the simulations and the set-up, followed by a comparison of results.

5.2 BLAST RESPONSE OF SEGMENTED BORED TUNNELS WITH RECTAGULAR SEGMENTS

Bored tunnels run through densely populated city centres where the tunnels come to the ground surface via tunnel portals and/or underground stations. In this area, the tunnels appear to be shallow. The required minimum depth of the tunnel is determined by the demand of TBM that requires a certain amount of soil (overburden) above the tunnel in order to drive the TBM and the vertical stability (under effect of buoyancy) of the tunnel after construction. As a "rule of thumb", a minimum depth of cover is considered as 1D where D is the outer diameter of the tunnel. The tunnel linings consist of precast reinforced concrete segments connected by bolts at their interface.

5.2.1 Description of segmented tunnel

As far as urban rapid transit railway tunnels are concerned single tube (single track) tunnels with inner diameter between 5.40m and 6.40m are common. Figure 5.1 describes the details of a single tube transit tunnel. The tunnel has an inner diameter of 5.80m and an outer

diameter of 6.35m. A lining ring (width of 1.4m) consists of six similar precast reinforced concrete segments spanning the circumference of the tunnel. The reinforcement provides resistance against varying earth pressure due to both static and dynamic situations. The segments are reinforced concrete (grade 60-Appendix B) with a concrete cover of 40mm. The segments are rotated from ring to ring by 30^o in order not to line up along the longitudinal direction. Every single segment is attached to its neighbouring segments by bolts in both radial and circumferential directions, in which joints are considered as flat surfaces, as described in Figure 5.1. The bolts are M24 grade 8.8 curved bolts.

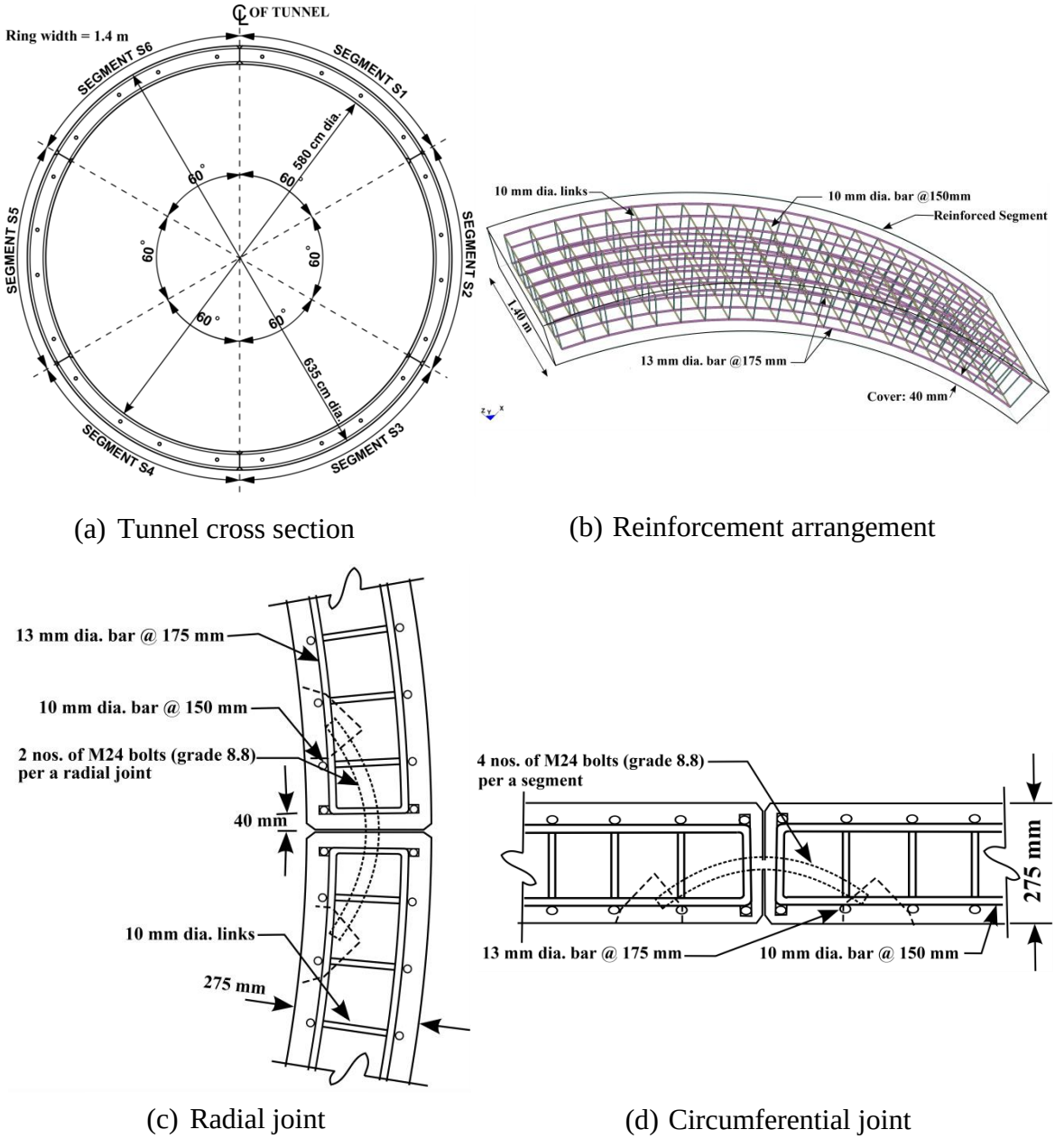

(a) Tunnel cross section (b) Reinforcement arrangement

(c) Radial joint (d) Circumferential joint

Figure 5.1: Rectangular Segments (RS)

5.2.2 Description of numerical model

The problem was modelled using the ALE modelling technique and material models discussed in Chapter 3. As the lining has no-uniform properties about its periphery because of such joints, a half symmetric model was considered. As shown in Figure 5.2, the model involved a half of the air domain, soil domain, explosive and tunnel structure with appropriate boundary conditions. The surrounding soil represented the dry Nevada sand discussed in Chapter 4. The CONTACT_AUTOMATIC_SINGLE_SURFACE contact was used to define the interface between the segments. The curved bolts were simulated as a chain of four numbers of straight beam elements making the curvature. Reinforcing beam elements and bolts were modelled as discrete elements immersed in the segments meshes using the CONSTRAINED_LAGRANGE_IN_SOLID coupling.

Cylindrical disk type explosives were placed on the ground surface directly above the tunnel crown. In order to examine the effect of explosive weight, five load cases were considered by varying the explosive weight from 250 to 1250kg of TNT, by equal amount of 250kg as shown in Table 5.1, for the minimum tunnel depth of 6.35m.

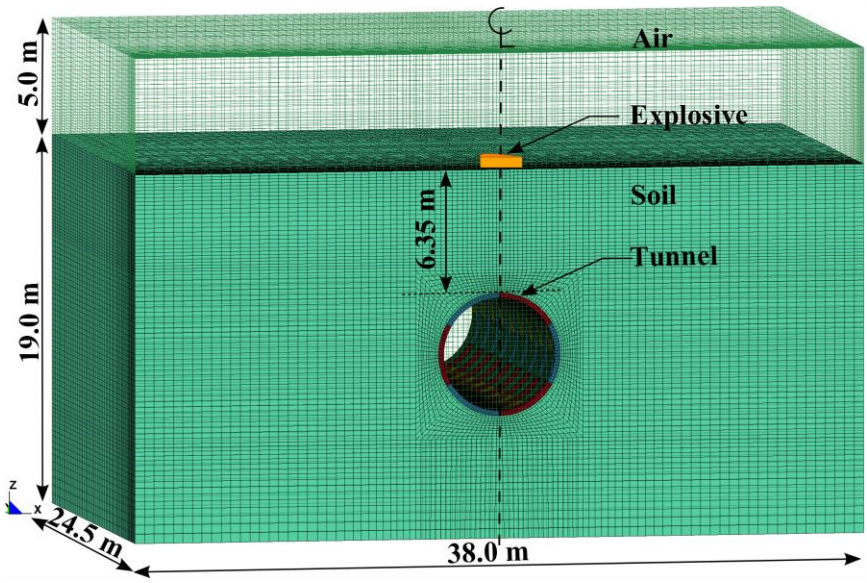

Figure 5.2: Configuration of the coupled numerical model.

Table 5.1: Load cases

Case	1	2	3	4	5
TNT explosive, (kg)	250	500	750	1000	1250

5.2.3 RS Tunnel response

Prior to the blast, gravity loading was applied to preload the model. As shown in the displacement vs. time plot in Figure 5.3, the tunnel was brought to the geostatic equilibrium state where the maximum displacement was within the allowable deflection of 1% internal diameter. The blast simulation was conducted for a duration of 50ms in order to evaluate the initial damage.

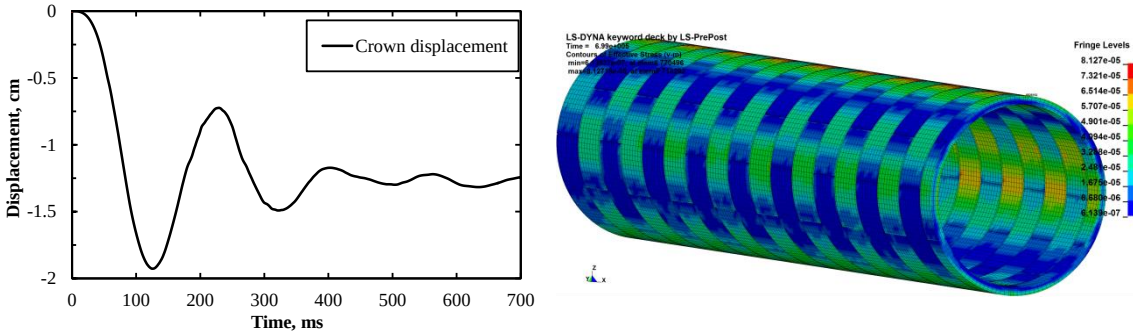

(a) Displacement-initialization (b) Initialized tunnel under gravity

Figure 5.3: Gravity initialization.

Figure 5.4(a) illustrates the blast load transfer mechanism in the tunnel. When the shock waves impacted the tunnel, the segments along the tunnel crown were compressed in the longitudinal direction as the shock waves progressed. However, as a result of soil confinement, energy dissipation of joint interfaces and shock wave attenuation, this effect was localized within a limited number of segments from the explosive, as shown in Figure 5.4(b). At the invert level, blast induced tension force in the longitudinal direction was redistributed to adjoining segments through the bolted circumferential joints. Although out of plane movements in the tunnel are naturally restrained along the longitudinal tunnel axis, the blast induced tension triggered the yielding of bolts. It was found that gaps which

opened between segments were insignificant (maximum of 1.2mm for load case 5) due to the fact that the bolts were strong in tension.

As the shock waves travelled through the tunnel, ovaling of the tunnel profile (in-plane response) was observed in the lining ring. Within the lining ring, segments responded in an arch like behaviour that directly transferred the load to adjoining segments through the radial joints. In the longitudinal direction, the vertical component of the blast load was redistributed to its adjacent segments through the shear force transmission capacity at the circumferential joints. In order to assess the in-plane response of the ring immediately below the explosive, displacement history of closest point on the tunnel crown was considered as shown in Figure 5.5. As expected, the vertical deformation increased with explosive weight. For load case 1, the tunnel crown experienced more than six times its geostatic displacement. For load cases 2 to 5, the peak crown displacements were several times of the geostatic displacement. This can be a hazard for the operational envelop which accommodates train and other services.

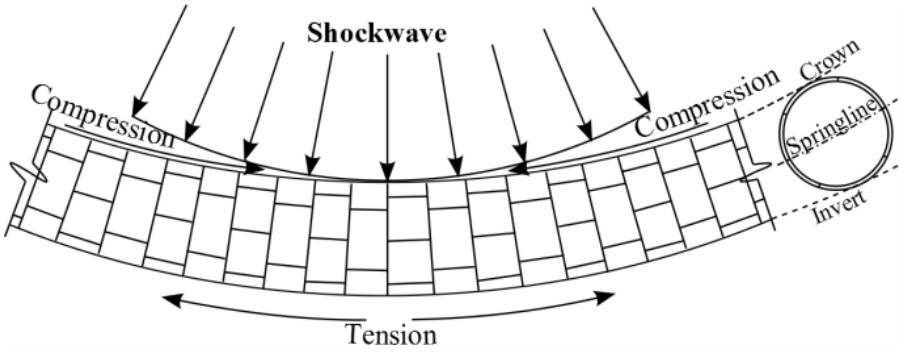

(a) Blast load transfer mechanisms

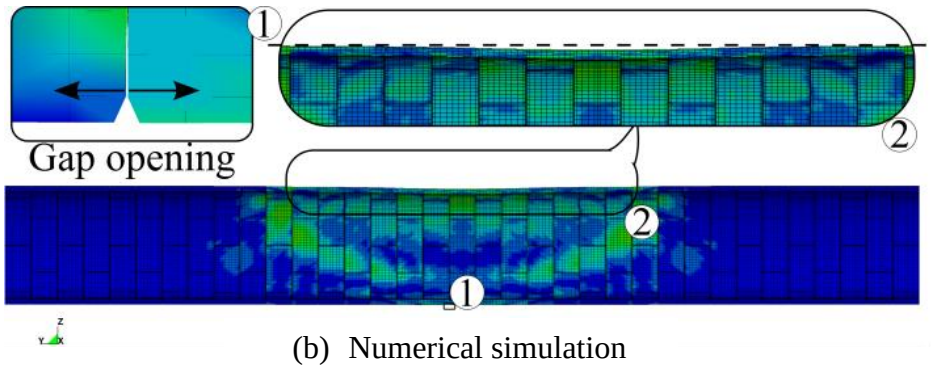

(b) Numerical simulation

Figure 5.4: Tunnel response in longitudinal direction

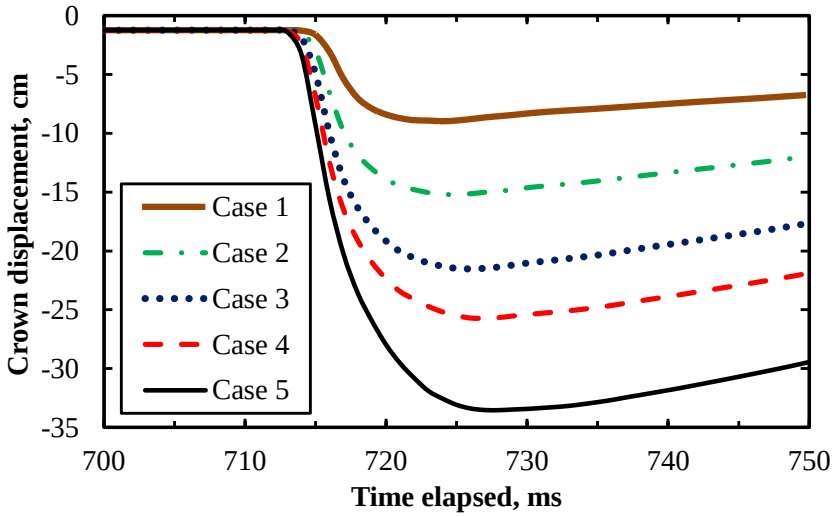

Figure 5.5: Tunnel crown displacement

Figure 5.6 demonstrates that the segments moved relative to each other (in the form of drifting response). This mainly occurred perpendicular to the tunnel axis between the rings along the longitudinal direction caused by the vertical component of the blast load redistributed to the adjoining rings through the bolted joints. These were weak in shear and in the vicinity of the explosion, many bolts failed in shear in the common planes and not through global deformation of the rings. As there were no bolt failures at the circumferential joints for load cases 1 to 3, the drifting responses were significantly recovered. However, load cases 4 and 5 generated a permanent drifting response as shown in Figure 5.6(b) whereas the in-plane drifting response has insignificant effects on the tunnel response as shown in Figure 5.6(c). The drifting response resulted in offset between waterproofing gaskets as shown in Figure 5.6(a). Further drifting may accelerate the soil and water inflow which may make the situation even worse by affecting the integrity of the above ground structures.

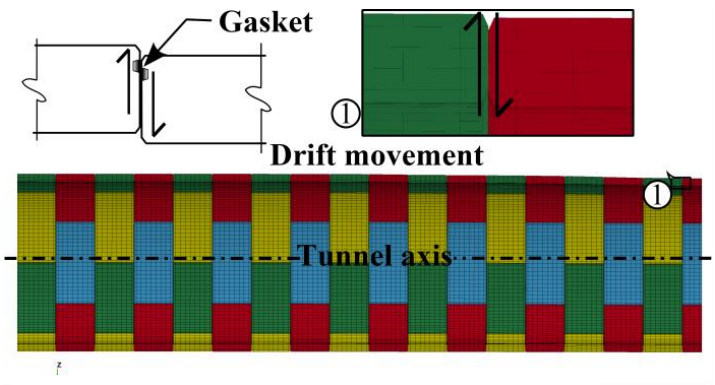

(a) Drift between adjacent lining rings

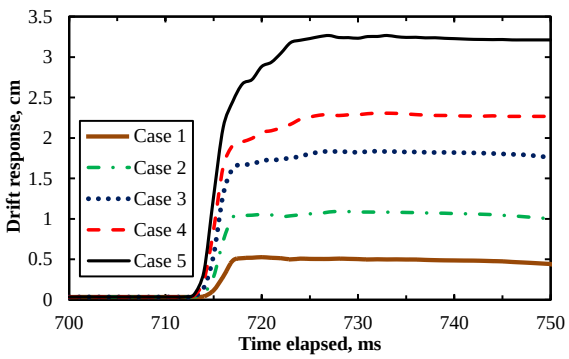

(b) Drifting response between lining rings

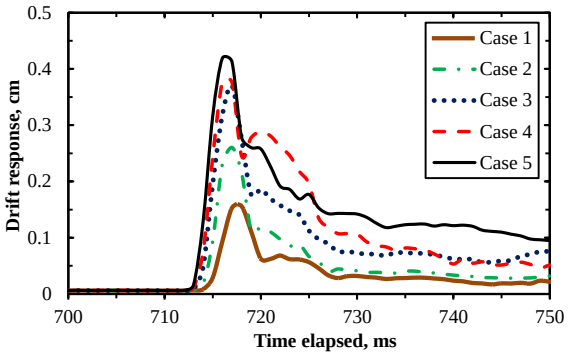

(c) In-plane drifting response between segments

Figure 5.6: Drifting response

The lining ring that was closest to the explosive ruptured first with cracks and a significant number of progressive cracks developed during the phase of lining vibration following the blast. Cracks were mainly generated by bending stresses. The number of cracks and the maximum crack widths increased with explosive as presented in Table 5.2. The crack width measurements were verified with a single element simulation in Appendix A. In all load cases, the maximum crack widths exceeded the design crack limiting value of 0.3mm (Engineering Group, 2010).

Table 5.2: Crack response under different load cases

Maximum crack width in mm / Nos. of cracks (crack width>0.3mm)				
Case1	Case2	Case3	Case4	Case5
1.92 / 396	4.11 / 907	5.43 / 1211	5.79 / 1472	7.33 / 1500

Figure 5.7 shows the cracks induced after 27 ms of detonation in load case 5. In the proximity to the tunnel crown as shown in Figure 5.7(a), the flexural cracks were first triggered by residual circumferential stresses from the combined action of hoop stresses and circumferential bending stresses on the interior surface of the segments. As displayed in Figure 5.7(b), further flexural cracks developed on the top surface of the segments due to the similar action, but the bending stresses were on the exterior surface. The main cracks that appeared in the longitudinal direction have the expectable orientation due to the bending stresses produced in the circumferential direction according to the ring-arch mechanism.

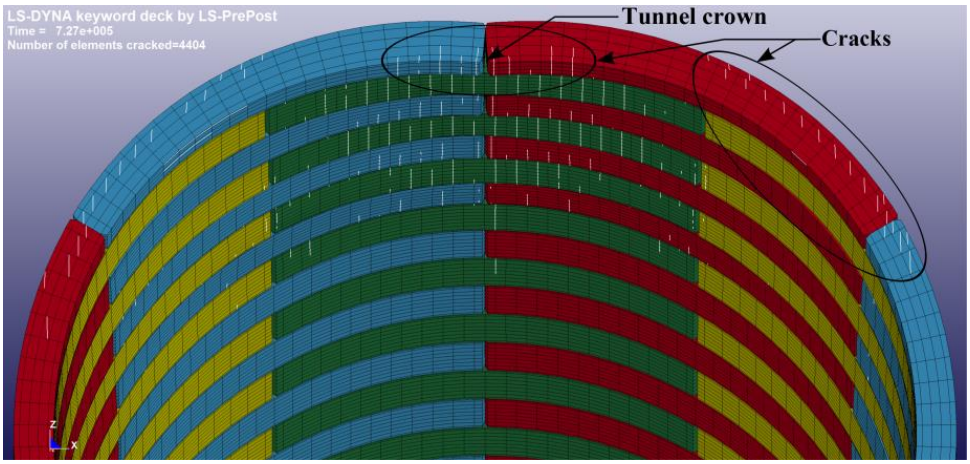

(a) view of cracks in the tunnel interior

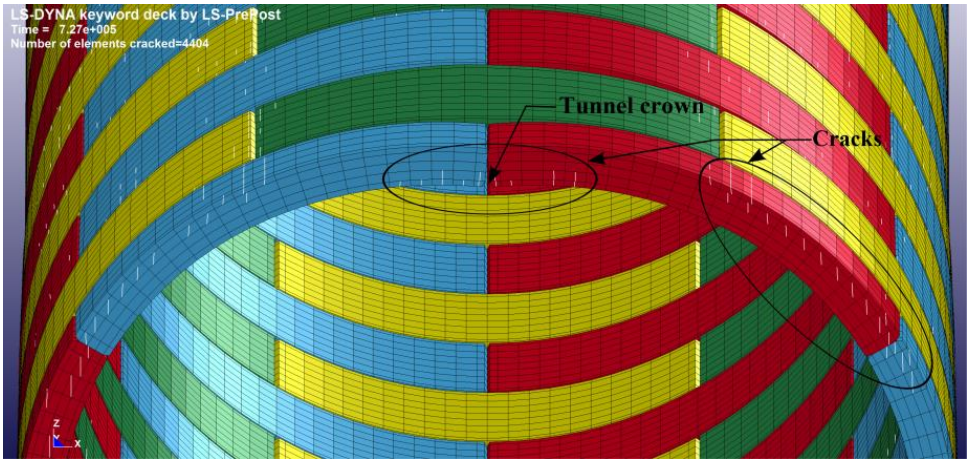

(b) view of cracks in the tunnel exterior

Figure 5.7: Crack patterns obtained from numerical simulations

5.3 BLAST RESPONSE OF SEGMENTED BORED TUNNELS WITH DIFFERENT TYPES OF SEGMENTS

The simulations indicated in the previous section that the drifting response resulted from the continuous vertical joints between the rings in a tunnel with RS system. In order to prevent the development of drift, two types of segment were considered. The first one is the precast concrete hexagonal segmental (HS) system which has the advantage of non-continuous ring joint. It is offset by a half segment width between the neighbouring segments along the longitudinal direction as shown in Figure 5.8(a). As there could be construction difficulties associated with the handling of the hexagonal segments by the conventional TBM which uses horizontal segment erection method, an interlocking segment (IS) system was also considered where a part of the segment is stepped and interlocked with neighbouring segments as shown in Figure 5.8(b).

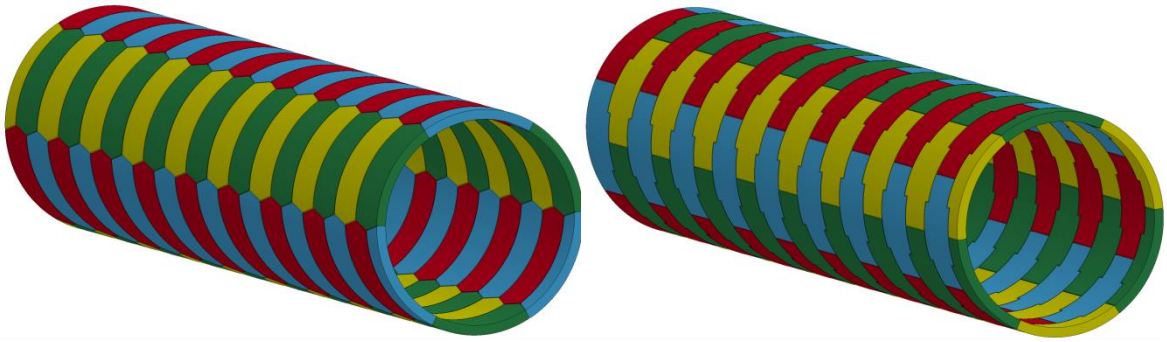

(a) Hexagonal segments (HS) (b) Interlocking segments (IS)

Figure 5.8: Different types of segments.

5.3.1 HS Tunnel response

Static responses of HS were similar to RS system under geostatic conditions, but there were significant changes in the blast responses due to the behaviour of joints. In the HS system, drifting response along the tunnel axis was essentially improved and converged to a very minimal residual displacement as shown in Figure 5.9(a). However, for weaker blast load, there were no significant change in the peak crown displacements (as shown in Figure 5.9(b)) compared to the RS system. For higher blast load, the crown displacements were slightly reduced because of the adopted joint system.

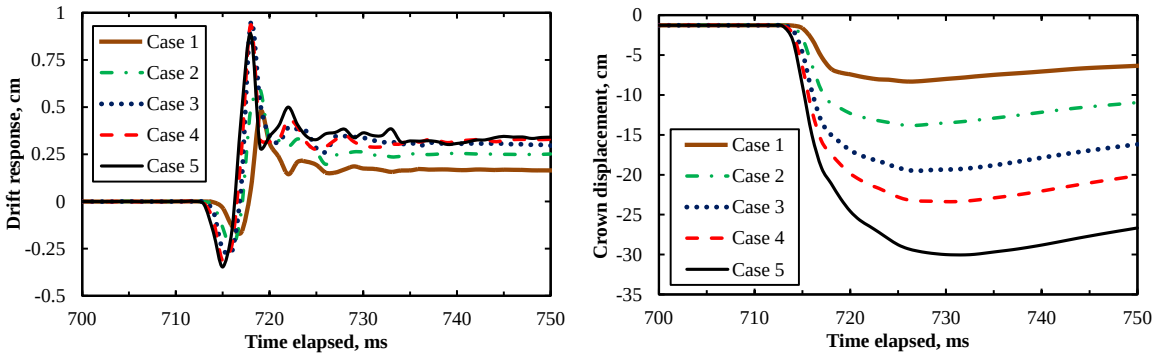

(a) Drifting response between lining rings (b) Tunnel crown displacement

Figure 5.9: Immediate HS ring response.

Figure 5.10(a) shows that for load case 3, the segments along the tunnel crown were subjected to extreme drift movements perpendicular to the tunnel axis. As the shock waves progressed, the crown-segments were disengaged and slipped along the adjacent segments upon failure of bolts in shear. While the drifting response developed and continued along the weakest plane as described by the zigzag lines, segments drifted relative to each other along the springline. Though this was a transient phenomenon and quickly returned to rest with a negligible residual displacement, the immediate crown-segment exhibited a large residual drifting of 11.0cm in the transverse direction as shown in Figure 5.10(b). Considering Figures 5.9(b) & 5.10(b), it is evident that the localized drift in the crown segment dominated the displacement response by more than 30%. Besides the localized drifting response, the global response of the overall HS system is stiffer than RS system. This resulted from the "V" shaped (two-surface) radial joints in HS system affecting the rotational ability (degree of flexibility) of the tunnel even though the "V" shaped joint consisting of two-surfaces significantly increased the sliding contact area compared to RS system which has a single surface radial joints (the radial joints are parallel to the tunnel axis).

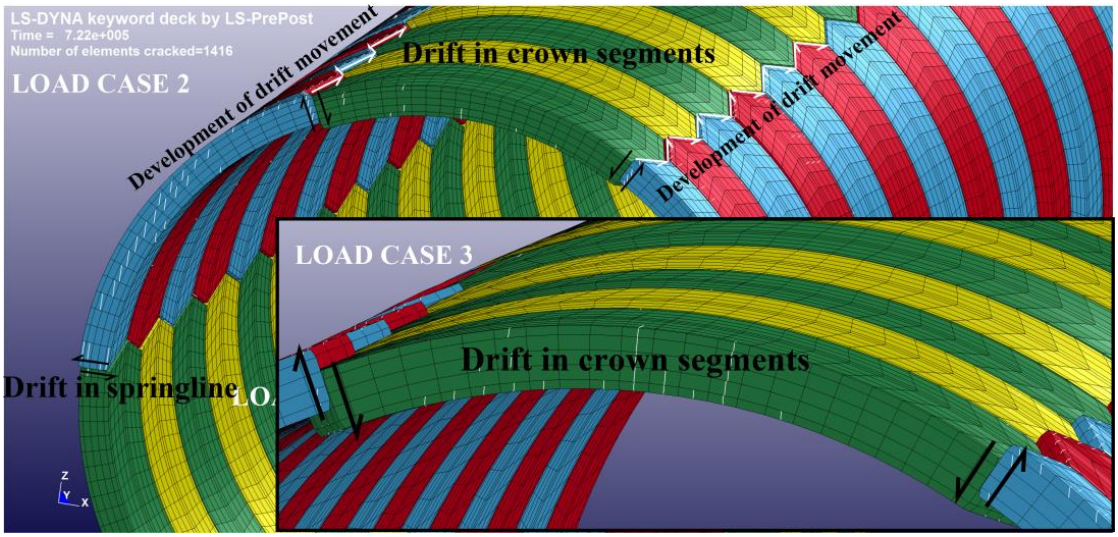

(a) Drifting response (Load cases 2 and 3)

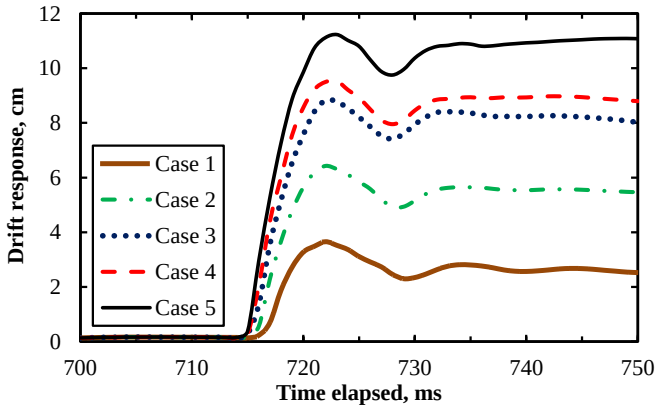

(b) In-plane drifting response between segments

Figure 5.10: Hexagonal segmented tunnel response.

5.3.2 IS Tunnel response

Finally, the IS system response is compared with RS system. The tunnel suffered permanent drifts between tunnel rings in all load cases, as shown in Figure 5.11(a), and the drifts were comparatively more than RS system. As shown in Figure 5.11(b), displacements were slightly more than RS system with unsmooth lines due to a series of sudden drift movements. Although the radial joints are parallel to the tunnel axis, alignment of radial joints (multi-surface) in the interlocking segment affected the flexibility of the radial joints.

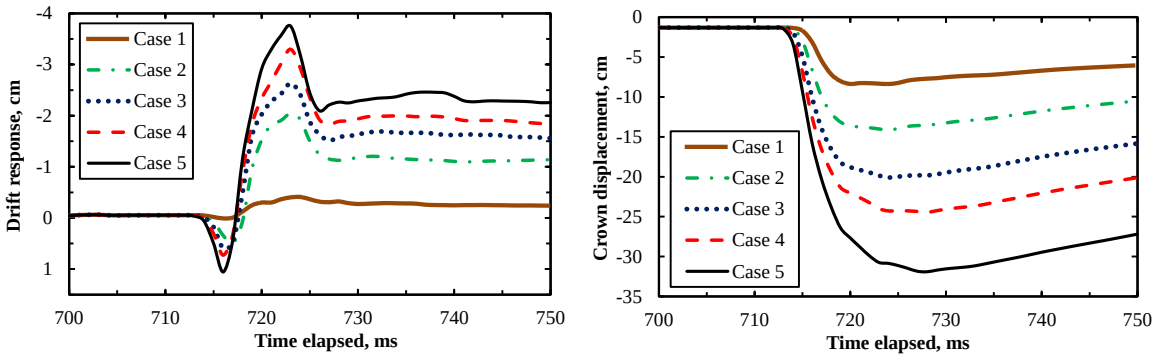

(a) Drifting response between lining rings (b) Tunnel crown displacement

Figure 5.11: Immediate IS ring response.

Figure 5.12 illustrates, for load case 5, that the tunnel rings suffered permanent drifts not only in the longitudinal direction, but also in the transverse direction (in-plane drifts) of the tunnel. As shown in Figure 5.12(a), nosing of the interlocking segments were subjected to a high concentrated stress due to the extreme hoop stress from the crushing of adjoining segments. This resulted in contact-element distortion and it appeared with cracks around the nosing of contact elements. It can be clearly seen that the downward drift at the crown, as displayed in Figure 5.12(b), increased the crown-displacement response. Overall, the interlocking joint system affected the tunnel response in both longitudinal and transverse directions of the tunnel.

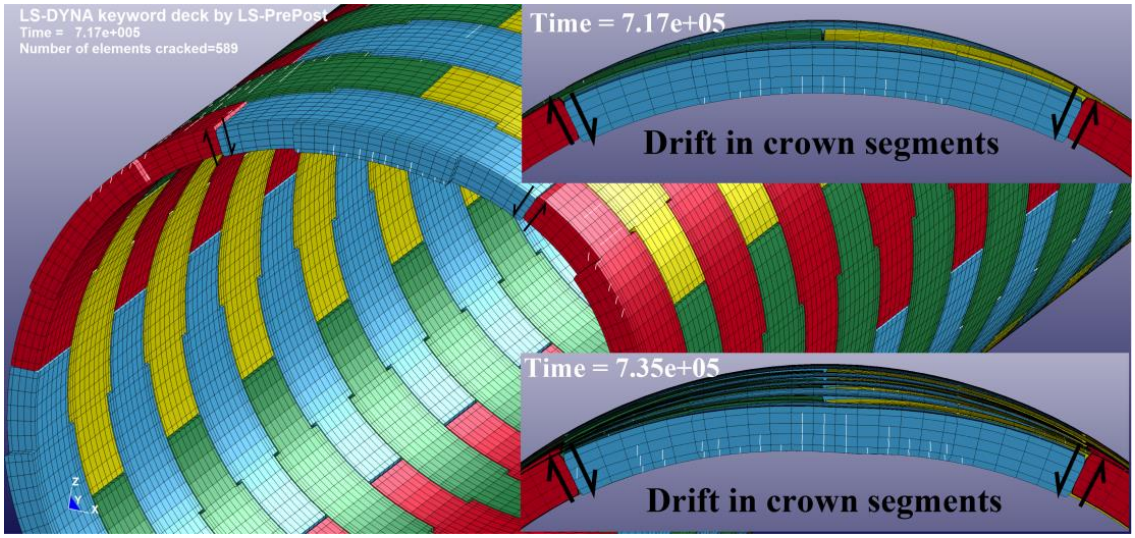

(a) Drifting response (Load case 5)

Figure 5.12: Interlocking segmented tunnel crown response

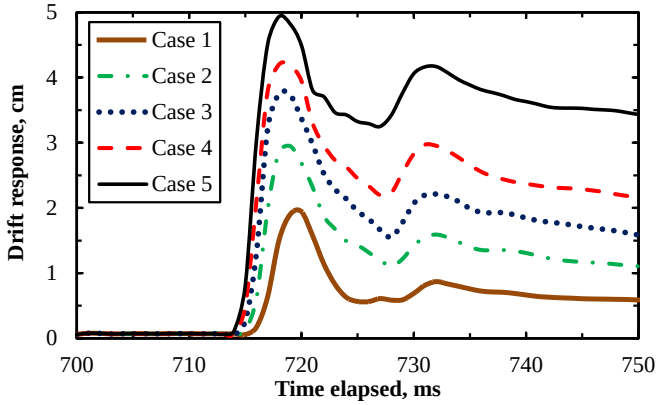

(b) In-plane drifting response between segments

Figure 5.12: Interlocking segmented tunnel crown response

5.4 NUMERICAL RESULTS AND DISCUSSION

The study provides confidence in adopting the established techniques to evaluate the response of segmented bored tunnels subjected to surface explosion using LS-DYNA. The blast performance of the segmented bored tunnels buried in dry sand was demonstrated for various blast load cases. The analysis showed that segments along the tunnel crown were compressed in the longitudinal direction while the segments in invert level were exposed to tension which generated a gap between the rings. The gap opening response was relatively insignificant compared to the compression induced effect at tunnel crown. However, the drifting response between the lining rings along the longitudinal axis is the main concern affecting the water tightness in the commonly used ring type modern tunnels. The hexagonal segmented tunnel system significantly reduced the longitudinal drifts, but it suffered in-plane drifts resulting from weak continuous joint alignments parallel to the tunnel axis. As shown in Figure 5.13(b), the 'V' shaped radial joints in the hexagonal segments affected the flexibility of the tunnel as well. The interlocking segmented tunnel system showed slightly higher crown-deflections than the commonly used tunnel system. It also suffered from drifts in all directions. Although the radial joints are parallel to the tunnel axis in the interlocking segmented tunnel, alignment of multi-surface contact in the interlocking segments, as shown in Figure 5.13(c), affected the flexibility of the radial joints.

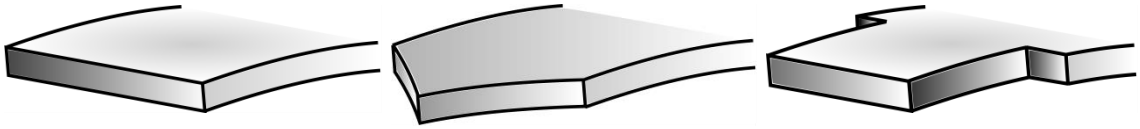

(a) RS-joint (b) HS-joint (c) IS-joint

Figure 5.13: Interface of radial joints

Comparison of different types of segment geometries demonstrated that the commonly used ring system with single-surface radial joints as presented in Figure 5.13(a) exhibited better performance with regards to the overall drift responses. In the transverse direction, this system is more flexible than other two systems in terms of in-plane drifting response. This suggests that providing a secondary lining around the primary lining will assist to redistribute the blast load to the neighbouring rings. The drifts in the circumferential joints needs to be further investigated to improve the joint performance under different soil conditions.

5.5 CHAPTER SUMMARY

In this chapter, a common single tube railway tunnel system with six identical rectangular segments (RS) were used to investigate the response of the tunnel subjected to surface blast. Fully coupled ALE numerical modelling technique incorporating Fluid Structure Interaction (FSI) as described in Chapter 4 was developed and applied. For a given tunnel depth of 6.35m, the influence of the explosive weight on the tunnel response was studied by varying the explosive weight. It was found that the number of cracks and the maximum crack widths in the segments increased with the explosive weight, as expected. Even for a small amount of explosive of 250kg of TNT, the maximum crack widths exceeded the design limiting value of 0.3mm. The tunnel experienced differential movements (in the form of drifting response) between segments in both longitudinal and circumferential directions. The drifting response in longitudinal direction, i.e between rings, affects the water tightness between the rings. However, in the circumferential direction, the drifting between segments (i.e in-plane drifting response) was insignificant.

Two types of segments, the hexagonal segments (HS) and interlocking segments (IS), were considered to study the drifting effects between the rings. HS tunnel system significantly reduced the drifts between the rings, but it suffered in-plane drifts resulting from weak continuous joint alignments in the longitudinal direction. IS tunnel system also suffered from the drifting between the rings as well as between segments in the plane of the ring. The drifting response revealed that the tunnel rings in the RC tunnel system were able to withstand higher blast loading compared to other two tunnel systems though they displayed noticeable drifting between the rings.

The coupled modelling techniques which were developed and applied to treat the blast response of buried tunnels provided useful information. The results on drift responses and vertical displacements offer new and valuable information in the area of blast response of segmented tunnels and will provide design information in future modelling and analysis in this area.

Chapter 6: Crucial parameters affecting the blast response of buried tunnels

6.1 INTRODUCTION

This chapter focuses on the investigation of several factors affecting the performance of shallow bored tunnels in soft soils. Blast performance of bored tunnel structures is influenced by the flexibility of the tunnel structure in relation to the properties of the surrounding soil medium. The tunnel lining needs to be adequately flexible to be able to deform and interact with the surrounding medium to resist the blast loading. After the blast, the tunnel must be able to return to operation without suffering unacceptable damages in the lining. The flexibility in the lining is determined by its ring bending stiffness which depends on the elastic modulus of the material as well as on the geometric properties of the lining, such as type of joints and number of segments used to form a ring.

The segmental linings are primarily made of reinforced concrete (RC) which behaves in a nonlinear manner. As the lining is subjected to blast loading, it cracks, behaves in a less stiff manner, and benefits by redistribution of moment along the circumference of the ring. The lining has joints which act like partial hinges. The stiffness of joints depends greatly on the stiffness of the individual bolts and joint orientations. Muir Wood (1975) suggested that the influence of joints may reduce the stiffness of the lining to one-fourth of the full lining value for an eight-segment lining. The reduction in the lining stiffness by increasing the number of segments increases the flexibility. However, the number of segments per ring depends on many parameters including the aspect ratio of the segment, internal diameter of the tunnel and the length of the segments (in the longitudinal direction). The number of segments per ring reduces in keeping with smaller tunnel diameters. For example, a common single tube railway tunnel system in Singapore (Wen et al., 2004) has five segments plus a key segment.

There are different types of radial joints including flat, convex and curved. The flat joints are more effective in terms of axial load transferring mechanism while both

convex and curved joints facilitate rotation at the joint, allowing the segment to deform and transfer moments at joints. Selection of an appropriate joint is essential to provide structural flexibility without the segments being drifted or displaced with one another in the radial direction.

The surrounding soil (soil skeleton) is a multiphase medium that includes solid soil particles, and pores filled with water and air as illustrated in Figure 6.1. The soil is dry if all pores are filled with air. If all pores are filled with water, the soil is saturated. Otherwise, the soil is partially saturated in which the water can be either continuous or discontinues in the pores depending on its degree of water saturation. Wang et al. (2004) described that the soil involves two basic deformation mechanisms under loading: (i) low pressure generates elastic deformation of bonds on the contact surfaces of particles; and high pressure generates both a failure in bond and displacements of the particles; and (ii) deformation occurs in all the soil phases based on their respective volume compression. When a soil experiences loading, both mechanisms act simultaneously.

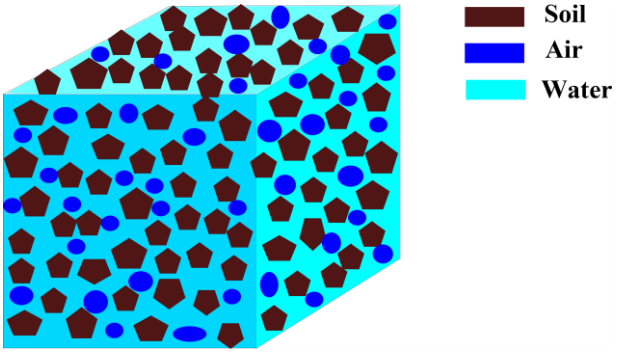

Figure 6.1: Soil skeleton

Under natural conditions, dry soil contains air and a small amount of water, whose compressibility significantly exceeds that of the skeleton. Under static and dynamic loading, the first mechanism initially governs the deformation. With increasing pressure, the bond between the particles deforms and displaces and the second mechanism becomes more important as the soil is compacted. In a saturated soil, the pores are filled with water and a little air. Under rapid impulsive loading, both the water and air provide higher load resistance than the particle bonds. The deformation and resistance are predominately determined by the second mechanism, specifically by

water and air deformation and the solid phase is only significant at relatively high pressure.

Under static loading, the water and air are squeezed out of the pores and the compressibility depends mainly on the solid skeleton. On the other hand, under blast loading, the soil skeleton deforms with the trapped air and water within the pores as the duration is not long for the air and water to flow through the skeleton. In this study, the soil model is considered as a single phase material at the macro view though the soil has a three phase material at the micro view.

This chapter first evaluates the blast performance of shallow bored tunnels in different soils. A common single tube railway tunnel system is considered and the tunnel ring includes five segments with a key segment along the tunnel circumference. A number of blast cases as described in Chapter 5 are considered by varying the mass of the explosive for a given tunnel depth of 6.35m. This chapter further investigates the effect of structural flexibility by varying the radial joints types and the number of segments forming the tunnel ring.

6.2 BLAST PERFORMANCE OF SHALLOW BORED TUNNELS IN DIFFERENT SOILS

6.2.1 Peak pressures in various soil types

The present study investigates the blast response of shallow bored tunnel in different soil types. Three types of soils considered by Jayasinghe et al. (2014) to investigate the blast effect on buried piles were used in this study. Table 6.1 presents the three soil types, such as saturated soil, partially saturated soil and dry soil. As described by Jayasinghe et al. (2014), a similar free-field study was conducted. The free-field peak pressure attenuation responses for those three soils were consistent with the plot presented by Jayasinghe et al. (2014). Figure 6.2 shows comparison of the peak pressure attenuation for the three types of soils as a function of scaled distances. It shows that both the soil type and the degree of water saturation played a large role in determining the peak pressures. The comparison shows that higher peak pressures occurred in the saturated clay soil.

Table 6.1: Soil properties for numerical simulation (Jayasinghe et al., 2014)

Soil properties	Saturated soil	Partially saturated soil	Dry soil
Composition	Clay	Sand & Clay	Sand
Density	2065 kg/m^3	1960 kg/m^3	1450 kg/m^3
Degree of saturation	100%	85% (V_a> 4%)	0%
Seismic velocity	1575 m/s	500 m/s	175 m/s

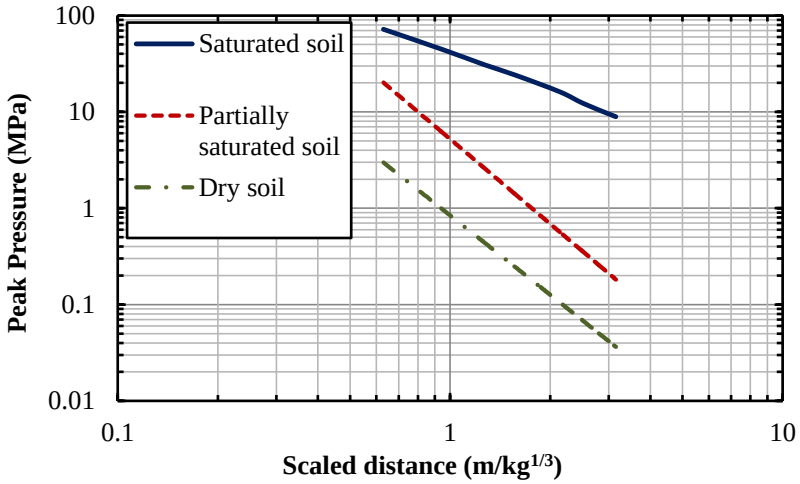

Figure 6.2: Comparison of free-field peak pressure

6.2.2 Description of segmented tunnel

As described in Figure 6.3, a common single tube railway tunnel system (Wen et al., 2004) was considered with a 150mm thickness annulus concrete grout of concrete grade 15 (Appendix B) around the tunnel. The inner diameter and the thickness of the tunnel lining were 5.8m and 275mm respectively. The segment was 1.4m length in longitudinal direction. As illustrated, the segments were rotated from ring to ring by 22.5 degree angle to the tunnel centreline (CL). Both radial and circumferential joints were flat and reinforcement details are described in Figure 5.1.

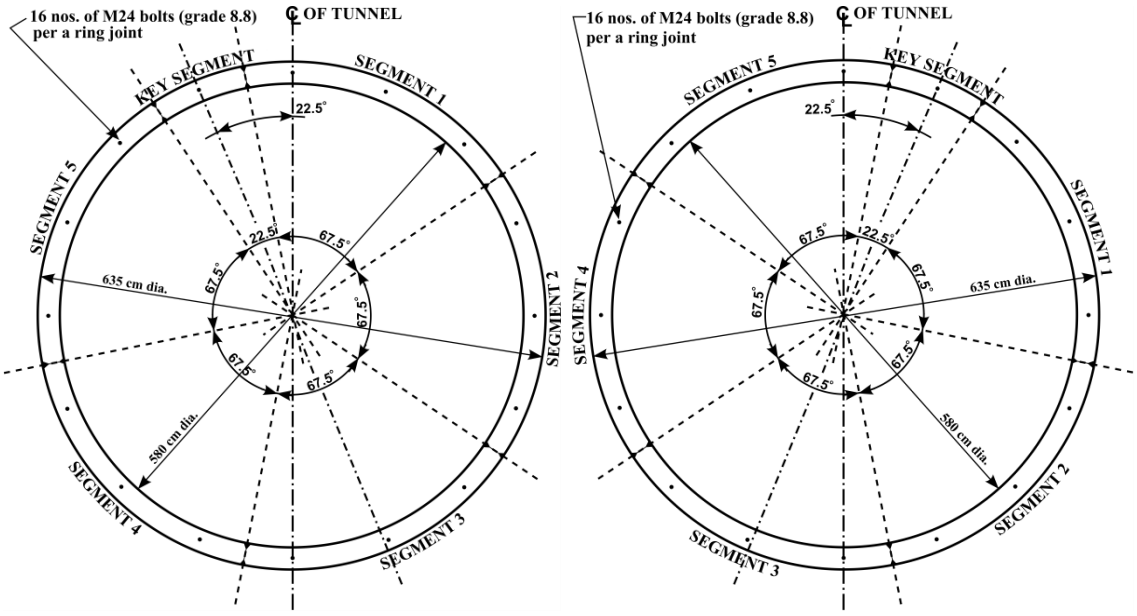

(a) Key segment: left-hand CL (b) Key segment: right-hand CL

Figure 6.3: General arrangement of segments

6.2.3 Description of numerical model

Figure 6.4 represents the three dimensional numerical model to study the effects of surface blast loading on tunnel response under influence of the soil properties. By considering the symmetries, half of the geometry was modelled with a cylindrical explosive on the ground surface. The annulus gap grout achieved a full round embedment with the surrounding soil. Therefore, the interface between the grout and soil was modelled using merged nodes. However, the interface between the segments and grout was modelled using the penalty-based contact surface-surface type. The soil properties were changed to investigate their effects on the different aspect of the tunnel response.

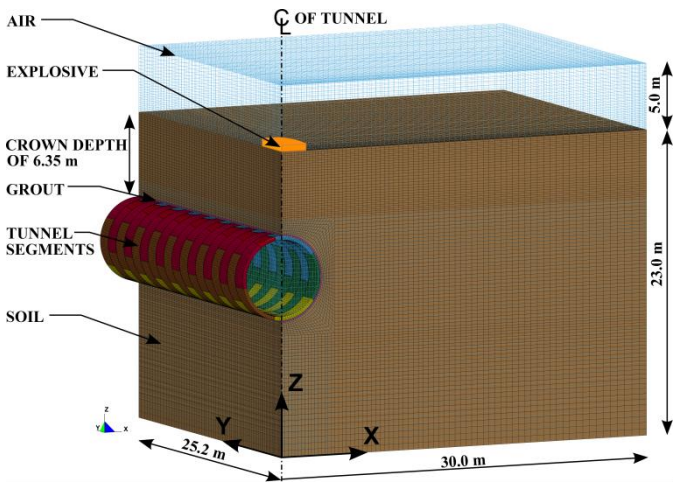

Figure 6.4: A half symmetrical numerical model

6.2.4 Blast response of segmented tunnel

Prior to the blast, the model was brought to equilibrium under gravity loading. As the simulations are quite expensive in terms of computational time and memory space, the process of capturing the blast responses was recorded over 300ms of duration. Blast induced tunnel deformations were three dimensional. However, as the tunnel is naturally restrained along the direction of tunnel axis, in-plane (ZX plane) deformation of the ring immediately below the explosive is critically more important than out of plane deformation in the blast analysis. Before the blast, tunnel exhibited a gravity-induced elastic diametric distortion. After the blast, the diametric distortion of the tunnel is significant as it changed its shape to ovalisation before the tunnel failed due to either the joint distortion or excessive cracks in the segmented tunnel. Blast induced tunnel in-plane deformation can be expressed by Equation 6.1.

$$D(t) = D_0 + \Delta(t) \qquad \text{Equation 6.1}$$

where: $D(t)$ is the diameter of deformed tunnel at time t, D_0 is the initial diameter of the tunnel and $\Delta(t)$ is diametric distortion at time t.

Figures 6.5 to 6.7 show the time histories of the diametric distortion which resulted from the displacement of the tunnel crown with respect to the tunnel invert in different

soils. The figures illustrate that the tunnel experienced unrecoverable deformation in all the cases. In general, after first peak, tunnels subjected to a series of noticeable fluctuations in distortion before steadying to residual distortions. It can be seen that the amplitude of the fluctuation depends on the soil type. For instance, the tunnel buried in the partially saturated soil displayed a quicker residual distortion than that in the other two soils. The tunnel buried in the dry soil suffered higher peak diametric distortions than the tunnel in the partially saturated soil. As expected, the tunnel buried in saturated soil produced considerably larger peak distortions. Beyond load case 3 in the saturated soil, the key segment in the immediate plane disintegrated from the neighbouring segments due to the drifting response resulting from the bolt failure and this may lead to progressive collapse of the tunnel structure. Therefore, it is recommended that the tunnels should be buried above the ground water table. However, this may not be practicable because of minimum soil cover requirement and variation of the ground moisture level with seasonal changes.

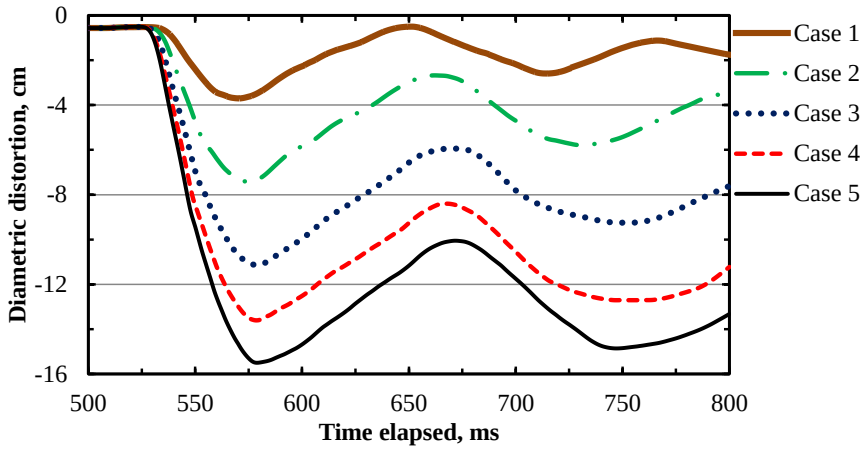

Figure 6.5: Diametric distortion in dry soil

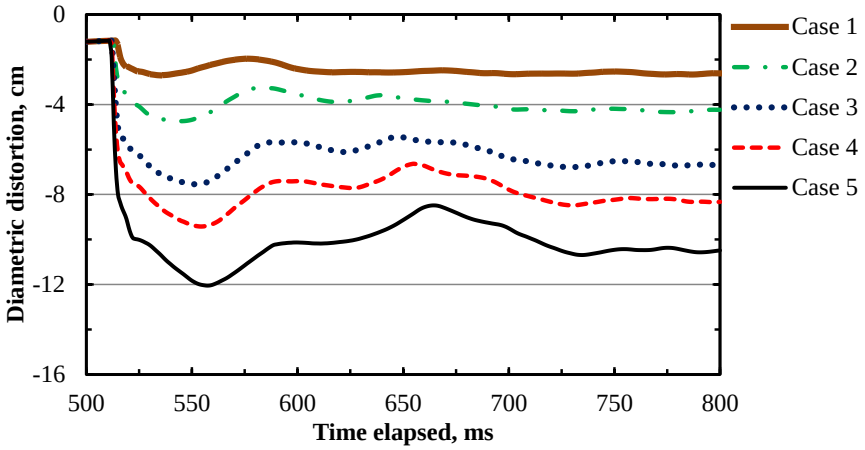

Figure 6.6: Diametric distortion in partially saturated soil

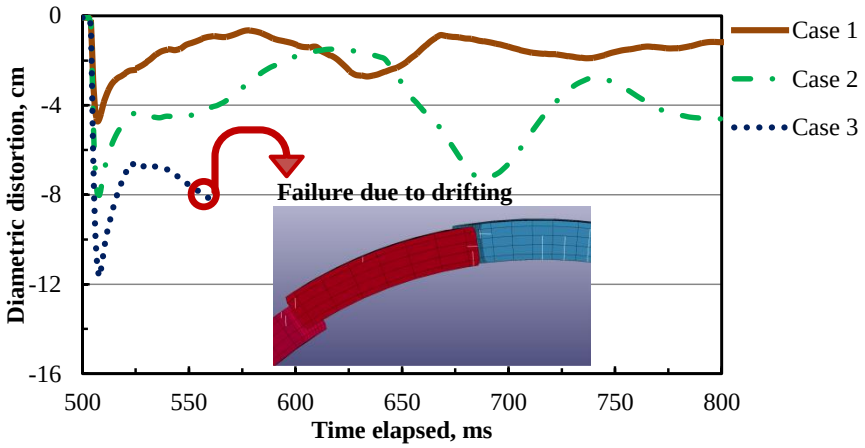

Figure 6.7: Diametric distortion in saturated soil

Table 6.2 compares the number of radial bolt failures during the first peak distortion and at the end of the simulation of the tunnel in different soils. There were no bolt failures in the tunnel buried in the dry soil for all load cases. Though the tunnel in the partially saturated soil displayed bolt failure for the highest load cases 4 and 5, in-plane tunnel profile were not affected by any form of drifting responses. For the saturated soil, there were bolt failures in all load cases. A comparison of peak pressure attenuations study, as shown in Figure 6.2, illustrates that the peak pressure of the saturated and partially saturated soils were 40 and 5 times the peak pressure of the dry soil at the depth of 6.35m for load case 1 (scaled distance ≈ 1.0m/kg$^{1/3}$). As a result, a large number of radial bolts failed in the saturated soil by the high intensity compressive blast wave impacting the tunnel crown. The number of bolt failure at the end of the simulation shows a rapid increase from load case 2 to 3 for the saturated soil.

Table 6.2: Numbers of radial bolt failure

	Numbers of radial bolt failure during the first peak distortion/end of the simulation(@ 800ms)				
	Case 1	Case 2	Case 3	Case 4	Case 5
Dry	0/0	0/0	0/0	0/0	0/0
Par. saturated	0/0	0/0	0/0	3/3	3/3
Saturated	1/4	4/11	7/32	9/41	11/51

Figure 6.8 illustrates the contours of plastic strain developed along the bolts connecting the key segment with neighboring segments during their respective first peak distortions. In dry soil, effective plastic strains in the bolts are very small for load case 5 as shown in Figures 6.8(a) and 6.8(b). As part of the modeling technique, a failure strain erosion criterion was used such that the beam elements within the concrete were eroded once the plastic strains within those elements exceed 0.12. In the partially saturated soil, for load case 4, the first bolt failed after 15ms of the explosion as displayed in Figure 6.8(d). At the end of the simulation, there were three bolt failures in both load cases 4 and 5. In Figures 6.8(e) and 6.8(f), the scenario was more critical in the saturated soil as all radial bolts failed immediately after the first peak distortion. After the bolt failures, as shown in Figure 6.7, the key segment drifted upwards due to the presence of blast induced negative pressure at the tunnel crown.

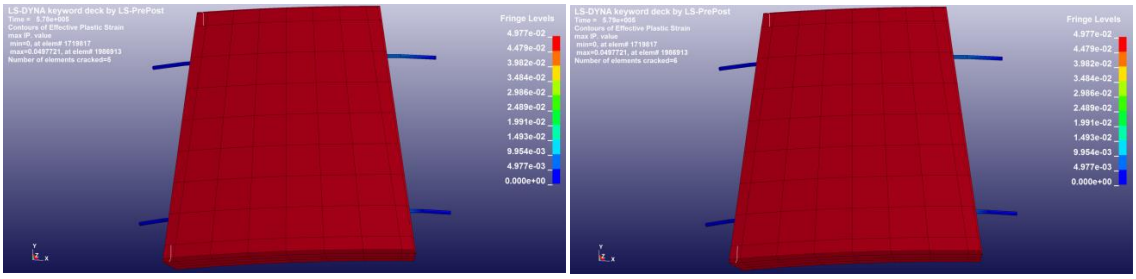

(a) t = 578ms (Dry -Case 5) (b) t = 579ms (Dry -Case 5)

Figure 6.8: Radial bolt failure adjacent to key segment

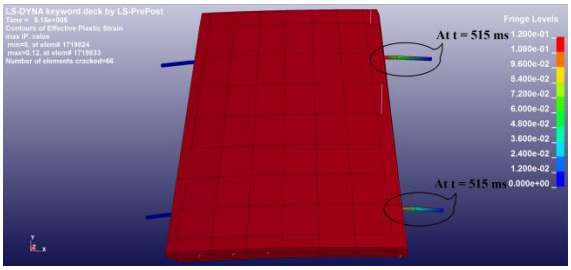

(c) t = 515ms (Partially saturated -Case 4)

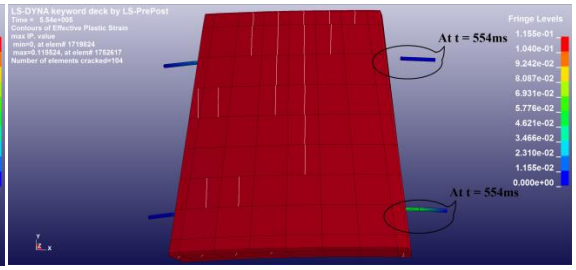

(d) t = 554ms (Partially saturated -Case 4)

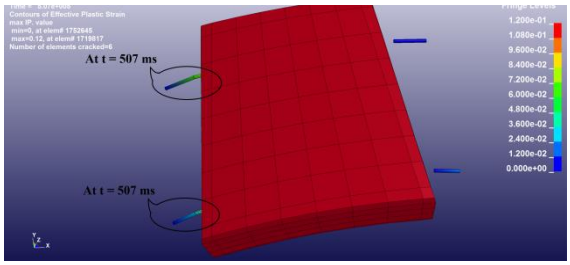

(e) t = 507ms (Saturated-Case 3)

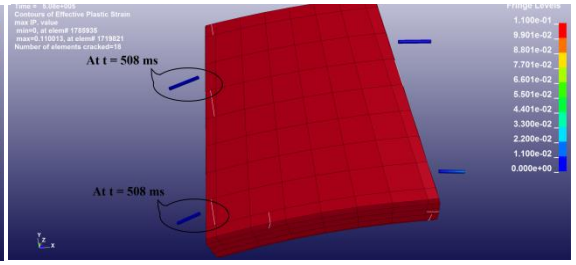

(f) t = 508ms (Saturated-Case 3)

Figure 6.8: Radial bolt failure adjacent to key segment

6.3 EFFECT OF RADIAL JOINT TYPES

This section examines how the tunnel's flexibility influences its response to the surface blast by varying the radial joint/contact types. The radial joints can be either designed as flat, convex-concave or convex-convex. The capacity of a joint to resist blast loading depends on the load transmission behaviour and its ultimate capacity. Table 6.3 compares the ability of joints to rotate and transfer the loads based on the geometry of the joints. Due to the inherent complex behaviour of segmental joints under blast loading, it is essential to study the combined effect resulting from rotation, axial/hoop force transmission and shear force transmission at the joints.

In this study, the circumferential joints were all considered as flat. The tunnels were buried in saturated clay soil. Other than the geometrical aspect of radial joints, the tunnels were identical in terms of structural aspects such as number of segments, dimensions, materials and reinforcement arrangements. Since the tunnel in saturated soil was severely deformed for the explosive of 750kg of TNT, the load cases were refined as presented in Table 6.4 with five new load cases to study the effect of explosive mass on the tunnel response.

Table 6.3: Radial joint types and corresponding force transmission capacity

Types of radial joints	Shear force transmission	Axial force transmission	Rotational capacity
 (a) Flat joint	Medium	High	Low
 (b) Convex-concave joint	High	Medium	Medium
 (c) Convex-convex joint	Low	Low	High

Table 6.4: New Load cases

Case	1N	2N	3N	4N	5N
TNT explosive, (kg)	250	375	500	625	750

The shockwave was transmitted to the tunnel lining in the form of compressive hoop stress and normal stress. The hoop stress acts along the circumference of the lining while the normal stress acts perpendicular the lining surface. Load case 1N was considered as an example to study the crack formation immediately after impact of the shockwave. There were no cracks in the flat joints as shown in Figure 6.9(d). As the hoop stress at the tunnel crown was greatly increased by the shockwave, in addition to the bolt resistance, the flat joints in the vicinity of the tunnel crown greatly resisted the blast induced normal stress by the increased frictional resistance capacity between the flat joints which are effective in transferring the hoop stress. However, a large number of elements of the convex-concave joints were cracked before the bolt failure due to a high intensity of shear force transmitted through the edge elements making the

periphery as displayed in Figure 6.9(f). It should be noted that the edge elements marking the periphery of the convex-concave joints were not reinforced because of minimum required concrete covers. Due to rapid increase in hoop stress at the tunnel crown, the convex-convex joints exhibited high stress concentrations at the radial contact causing splitting forces which resulted cracks in the segments as shown in Figure 6.9(g). In these joints, the normal stress was primarily resisted by radial bolts rather than the frictional forces at the interface. Until the bolts reached ultimate strength, the segments were slightly rotated about the joints. After the bolts failure, the segments were moved up and down with respect to the neighboring segments. As a result, the number of cracks appeared to be increased on the edges.

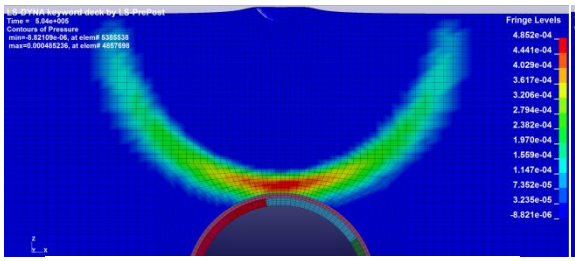

(a) Shockwave at 504ms

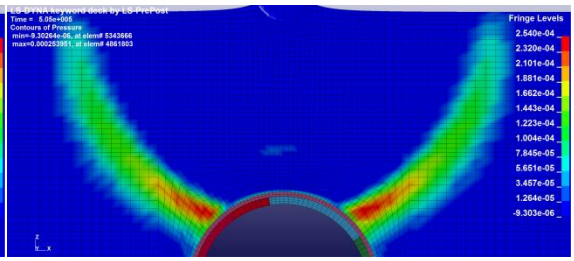

(b) Shockwave at 505ms

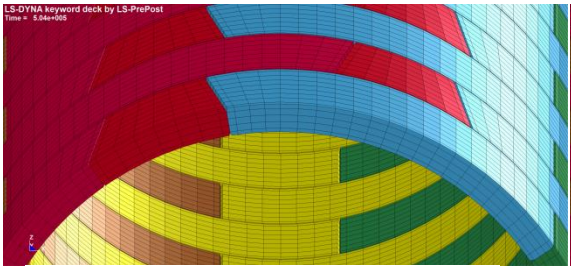

(c) Flat joint at 504ms

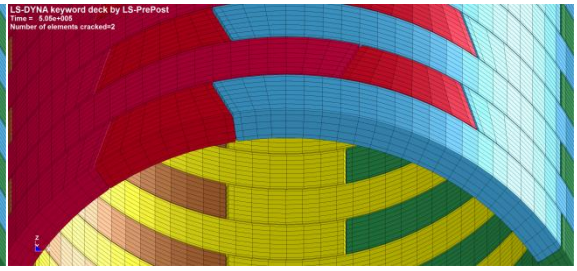

(d) Flat joint at 505ms

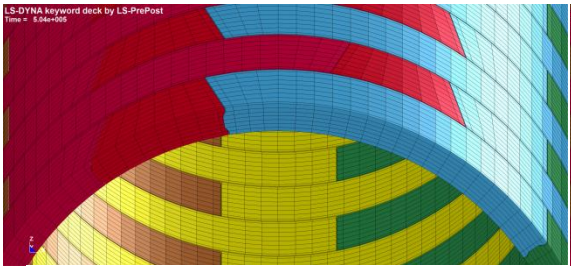

(e) Convex-concave joint at 504ms

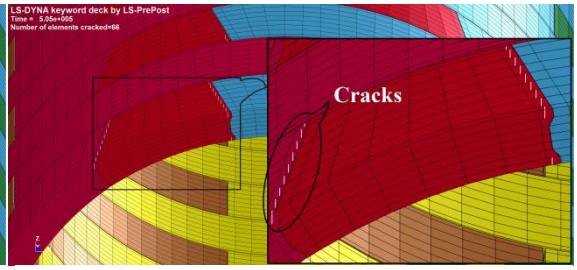

(f) Convex-concave joint at 505ms

Figure 6.9: Initial crack formation after impact of shockwave in load case 1N

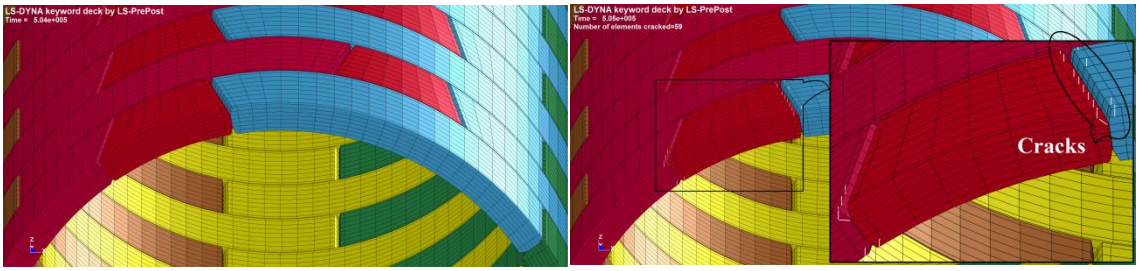

(g) Convex-convex joint at 504ms (h) Convex-convex joint at 505ms

Figure 6.9: Initial crack formation after impact of shockwave in load case 1N

Figure 6.10 describes the in-plane radial drifting response in different types of radial joints. In the first three load cases, the variations of the drifting responses were insignificant although the number of radial bolt failures varied significantly as summarized in Table 6.5. In load case 4N, both flat and convex-convex joints displayed larger drifting at the end of the simulation than in convex-concave joint. As the explosive is further increased to case 5N, the tunnel with flat joints suffered large drifting as shown in Figure 6.10(e). Although the tunnel with convex-concave joints displayed a larger number of bolt failures at the end of the simulation in load cases 3N to 5N, the high shear transmission capability resulting from the interlocking system in the convex-concave joint largely protected the tunnel profile at failure by minimizing the drifting responses.

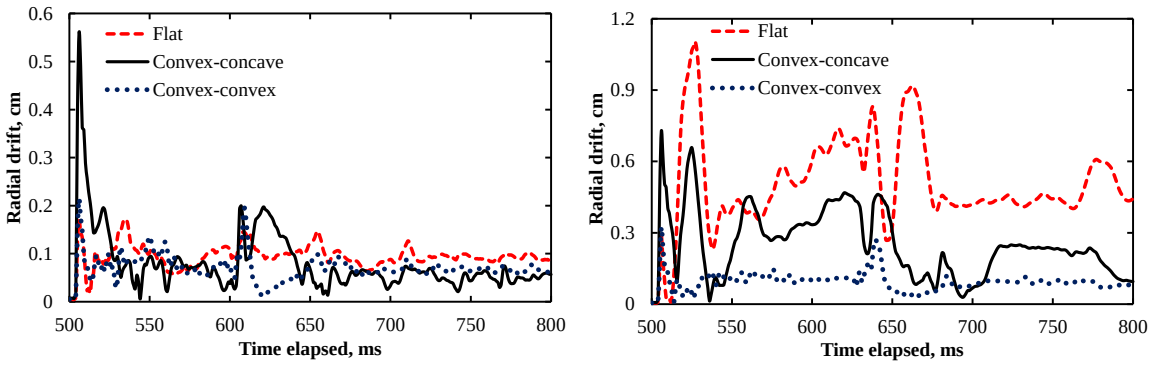

(a) Case 1N (b) Case 2N

Figure 6.10: Radial drift response of an immediate ring

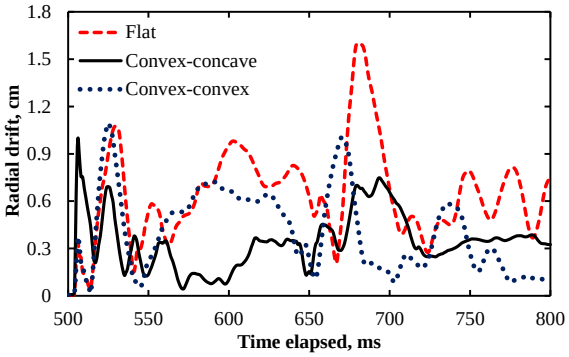

(c) Case 3N

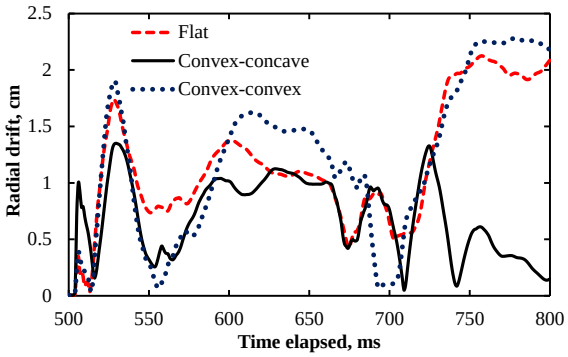

(d) Case 4N

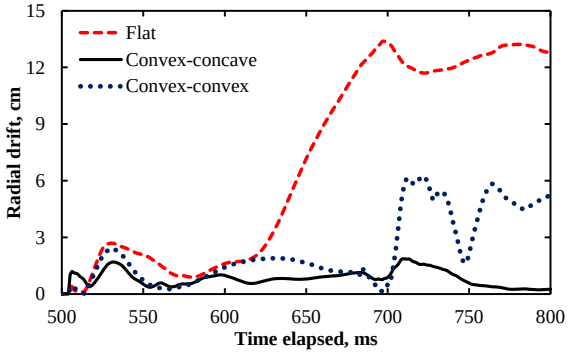

(e) Case 5N

Figure 6.10: Radial drift response of an immediate ring

Table 6.5: Numbers of radial bolt failure

	Numbers of radial bolt failure during the first peak distortion/end of the simulation(@ 800ms)				
	Case 1N	Case 2N	Case 3N	Case 4N	Case 5N
Flat joint	1/4	3/8	4/11	7/18	7/32
Convex-concave joint	0/2	0/6	0/17	4/30	6/39
Convex-convex joint	1/2	3/5	4/11	4/26	4/32

Table 6.6 compares the maximum crack width in both the first peak distortion and at the end of the simulation (at 800ms). It appears that the maximum crack width in the tunnel lining exceeded its limiting design value of 0.3mm at the end of the simulation in all load cases. As expected, the maximum crack width increases with the explosive mass. The cracks were opened and closed during the phase of vibration. Under small explosive loads (load case 1N), the convex-convex joint performance is better in terms

of the crack formation as the maximum crack width slightly exceeded the limiting value due to its greater flexibility allowing the segment to deform and dissipate the bending moment. During the first peak deformation, the joint proximity to the tunnel crown exhibited a maximum crack width of 0.42mm which is more than the crack width in the crown segment at the end of the simulation. The number of bolt failures was reduced by almost half in the flat jointed tunnel as summarized in Table 6.5.

In load case 2N, the convex-convex joint transferred a significant amount of moment to the mid-span of the segment. As a result, the tunnel was subjected to an increase in the crack width due to the increase in sagging moment. The convex-concave joint displayed large crack width during the first peak distortion due to the lack of reinforcement in the periphery of the joints. Table 6.5 illustrates that there were no bolt failures in the convex-concave joint during the first peak distortion, but the numbers bolt failure was considerably increased at the end of the simulation because the radial bolts resisted significant amount of share after failure of the edge elements making the periphery.

Table 6.6: Maximum crack width in mm

	Maximum crack width in mm during the first peak distortion/end of the simulation(@ 800ms)				
	Case 1N	Case 2N	Case 3N	Case 4N	Case 5N
Flat joint	0.12 / 0.62	0.51 / 0.63	0.65 / 0.97	0.74 / 1.61	0.92 / 2.20
Convex-concave joint	0.74 / 0.93	0.70 / 1.07	0.92 / 1.14	0.81 / 1.67	1.15 / 2.25
Convex-convex joint	0.42 / 0.37	0.48 / 0.89	0.65 / 1.90	0.69 / 2.12	0.85 / 2.57

As the explosive is increased to load case 5N, intensity of the blast induced shock wave is more concentrated on the tunnel crown. The rigid nature of the flat joints around the tunnel crown dissipated the blast energy by allowing the segments to slide against each other. This dissipation of local effects is further facilitated by failure of radial bolts. Consequently, the flat joint exhibited more radial drifting and hence induced an eccentricity at the joint causing additional moment in the segments. Similar to the flat joint, the convex-convex jointed tunnel suffered from high drifting response with the same number of bolt failures at the end of the simulation. Although the convex-concave

joint displayed more bolt failures, the joints sustained the higher load of explosive at failure. The maximum crack widths were nearly the same in all types of joints. This shows that choice of joint types has insignificant influence on the blast response of segmental tunnel for higher blast loads as the segments were damaged before activating the flexibility of the joints. However, for weaker/smaller blast loads ($\leq$250kg of TNT), the joint types influenced the tunnel response by allowing the segments to rotate about the joints.

Performance of the convex-concave joint can be improved by providing adequate reinforcement to facilitate the load transfer from one segment to another without cracking. However, the particular shape of the edges creating the periphery of the segment makes it difficult to place the reinforcement as a minimum required cover is necessary for protection against corrosion in the segments. On the other hand, the flat joints are very efficient in transferring the hoop stress between segments with less end reinforcement. Furthermore, the flat joints effectively provide grooves to accommodate the watertight gasket within the joints.

6.4 EFFECT OF NUMBER OF SEGMENTS

With an increase in the number of segments forming a ring, the number of joints increases accordingly. This section examines how the number of segments affects the flexibility of the tunnel. The stiffness of the joint is always less than that in the body of the segment. Therefore the flexibility of the tunnel lining increases with an increase in the number of segments. Equation 6.2 computes the equivalent stiffness of the lining from Muir Wood (1975). This equation demonstrates that the lining will always be less stiff than an unjointed lining if the number of joints is more than 4.

$$I_e = I_j + I\left(4/n\right)^2 \qquad \text{Equation 6.2}$$

where: I_e is moment of inertia of jointed lining

I_j is the moment of inertia of the joint

n is the number of joints (if >4)

I is the moment of inertia of the unjointed lining

In order to examine the effect of number of segments in a ring on the blast response of the tunnel, three types of segmented tunnels are considered by varying the number of segments as shown in Figure 6.11. These are labelled as Type 1, 2 and 3 and consist of five, six and seven segments respectively, including the key segment along the tunnel circumference. The key segments are of the same size in all three tunnel types. Types 1, 2 and 3 tunnels are similar in terms of structural aspects such as dimensions, materials, reinforcement arrangements and joint details. The joints were considered as flat in all three types.

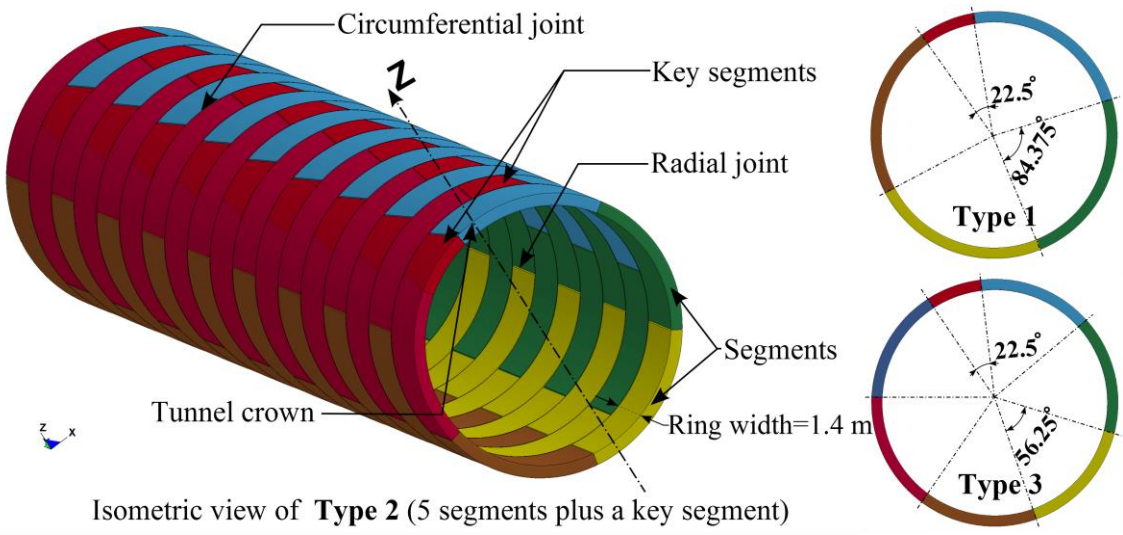

Figure 6.11: Isometric view of segmental lining

Figure 6.12 compares the in-plane radial drifting response between segments closest to the tunnel crown of the immediate ring. In load case 1N, there were no significant changes in the drifting response of those three tunnels. However, as the load increased from case 2N to 4N, Type 3 tunnel showed very minimal drifting compared to other two tunnels. Beyond load case 4N, all the tunnels suffered excessive drifting and wide cracks that lead to high strain in the reinforced steel and also many bolt failures at the joints. Excessive drifting response can lead to a progressive collapse of the tunnel structure.

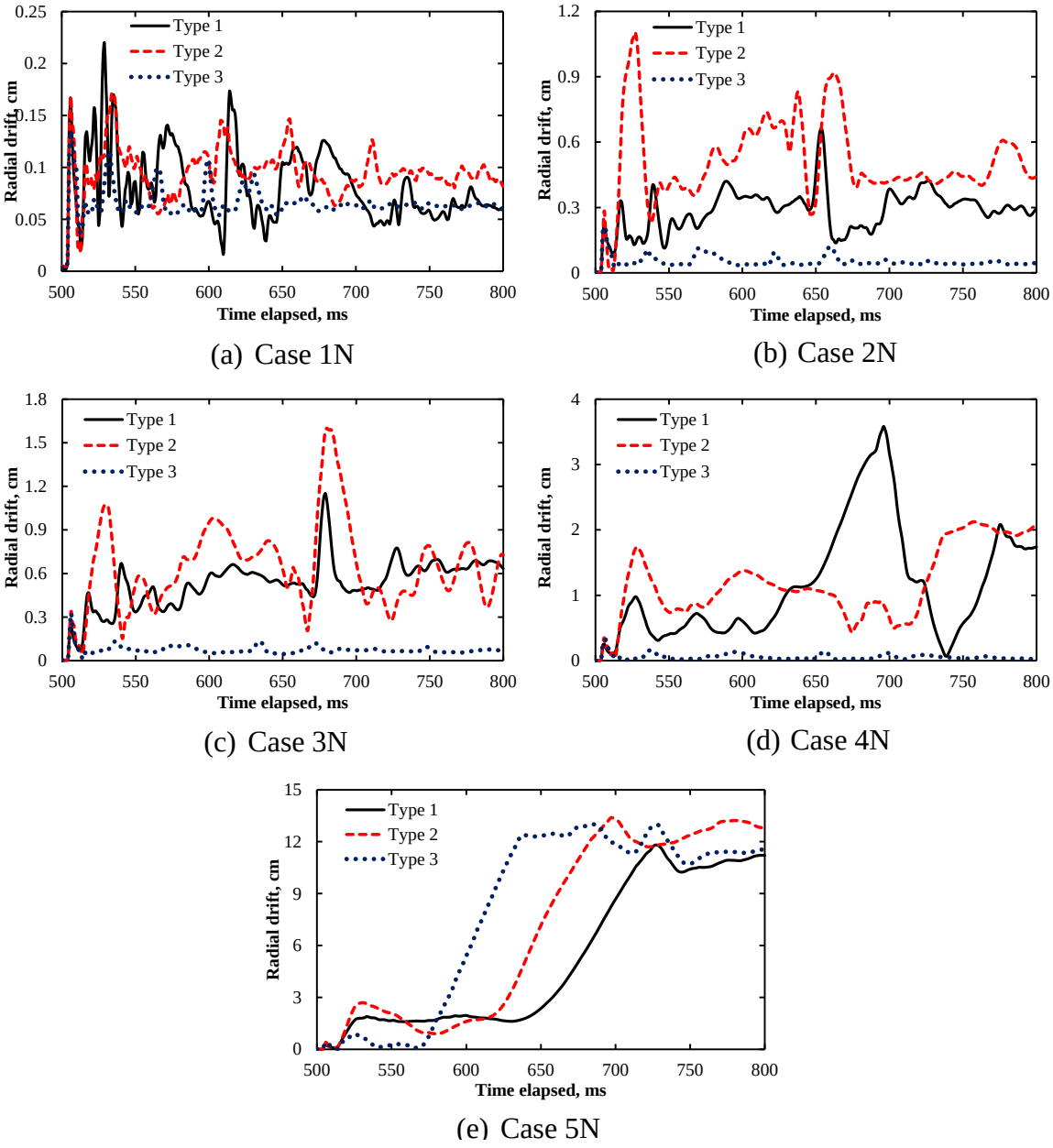

Figure 6.12: Radial drift response of an immediate ring

Figure 6.13 shows the crack development after 300ms of the explosion in Type 1 tunnel for load case 4N. The lining ring that was closest to the explosive ruptured first with flexural cracks, followed by inclined flexure-shear cracks above the springline of the tunnel. The flexural cracks formed when the tensile stresses due to bending exceeded the flexural strength of the concrete under arch mechanism of the tunnel behaviour. The cracks developed and extended to adjoining rings during the phase of shock wave propagation. Within the ring, the segment on the right-hand side of the key segment suffered excessively and a deep crack progressed through the entire segment material at

the tunnel crown. This segment is therefore at risk of failing. However, as the key segment has a small arc angle, it showed minor flexural cracks which opened and closed during vibration and degree of severity. As expected, number of cracks, crack widths and depths (crack depth to width ratio) increased with explosive mass. Observed flexural cracks at the tunnel crown were much more than the shear cracks and the flexural crack widths varied in range from 0 to 3.41mm.

Full-depth flexural cracks rarely occur in the segments as one part of the cross section (in the longitudinal direction) should be in compression at all times to provide the internal bending moment to resist the external moment which results from both the soil and the blast loads. Most of the cracks formed during the phase of blast impact were closed on the compression side of the segment under the action of the hoop stress. However, a crack which opened fully at the tunnel crown did not close during the tunnel fluctuations and the bending moment was significantly reduced to a small value. This could be possible as the doubly reinforced section could provide the essential internal resisting moment, without the need of compression in the concrete.

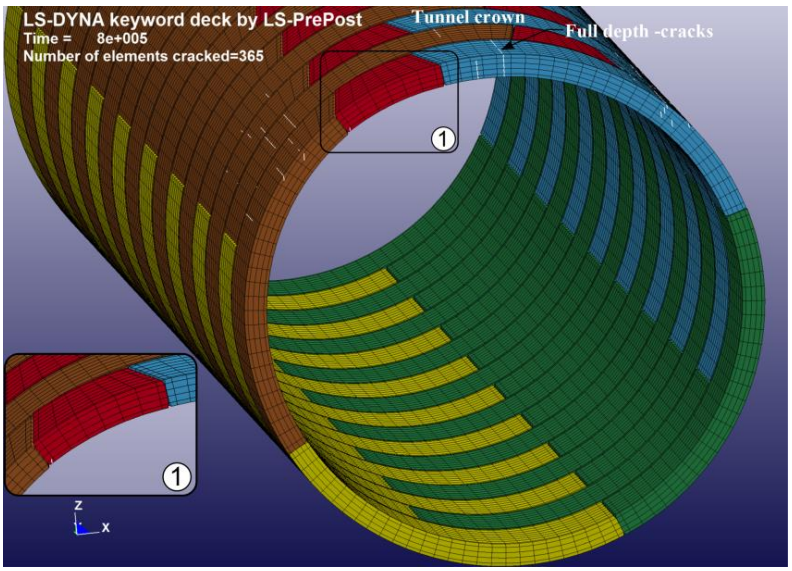

Figure 6.13: View of cracks (>0.3mm) in Type 1 tunnel in load case 4N

The stiffness of the segment is relatively higher than that in the radial joint. The stiffness of joints using bolts in tension and shear depends greatly on the stiffness of the individual bolts and joint orientations. Blast induced global response of the tunnel is governed by the joint stiffness provided that the segments are adequately reinforced.

Reduction of the tunnel stiffness due to excessively wide and deep cracks in the segments altered the load transfer mechanism, by which the segments were prompted to rotate about the weakest cracked plane rather than about those radial joints. This could be the reason that the in-plane drifting response is significantly smaller in Type 1 tunnel than that in Type 2 tunnel, in which the key segment drifted relative to the right-hand segment as shown in Figure 6.14. As the number of segments in a ring increased from Type 1 to Type 2, the numbers of elements cracked (crack width > 0.3mm) were reduced by nearly half and cracks were shallower and thinner.

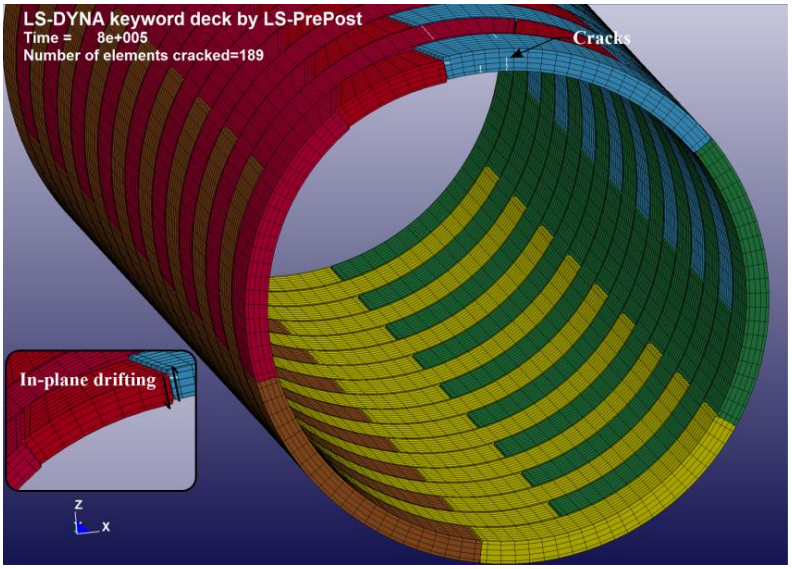

Figure 6.14: View of cracks (>0.3mm) in Type 2 tunnel in load case 4N

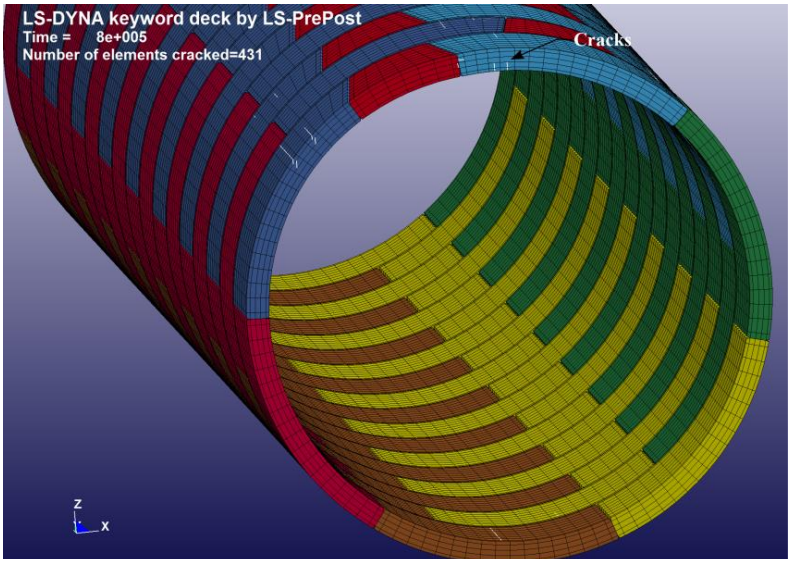

Figure 6.15: View of cracks (>0.3mm) in Type 3 tunnel in load case 4N

Table 6.7: Maximum crack width in mm

	Maximum crack width in mm during the first peak distortion/end of the simulation(@ 800ms)				
	Case 1N	Case 2N	Case 3N	Case 4N	Case 5N
Type 1	0.13 / 1.46	0.80 / 1.95	1.16 / 2.76	1.51 / 3.41	0.95 / 3.77
Type 2	0.12 / 0.62	0.51 / 0.63	0.65 / 0.97	0.74 / 1.61	0.92 / 2.20
Type 3	0.38 / 0.49	0.54 / 0.84	0.57 / 1.42	0.82 / 1.46	0.95 / 2.78

Table 6.8: Numbers of radial bolt failure

	Numbers of radial bolt failure during the first peak distortion/end of the simulation(@ 800ms)				
	Case 1N	Case 2N	Case 3N	Case 4N	Case 5N
Type 1 (10 radial bolts/ring)	0 / 1	0 / 2	2 / 4	2 / 14	3 / 21
Type 2 (12 radial bolts/ring)	1 / 4	3 / 8	4 / 11	7 / 18	7 / 32
Type 3 (14 radial bolts/ring)	0 / 0	1 / 2	1 / 3	1 / 5	3 / 9

The numbers of elements cracked in Type 3, as displayed in Figure 6.15, were more than twice those for Type 2. As presented in Table 6.7, the maximum crack widths were not much different compared to those in Type 2 tunnel. On the other hand, the numbers of radial-bolt failures were largely reduced in all load cases as shown in Table 6.8. As a result of less numbers of bolt failures at the radial joints, in-plane drifting responses were insignificant. While Type 3 tunnel offered better performance in terms of reduced radial bolt failure because of its increased flexibility, Type 2 tunnel suffered a large number of radial bolt failures among other tunnels in all load cases.

Besides the radial bolt failures, the tunnels experienced a significant number of bolt failures at the circumferential joints. There were no circumferential bolt failures for load cases 1N to 3N. However, in load case 4N, the circumferential bolts in the ring at the tunnel crown failed because of the high stress concentration from the blast induced shear transmission force induced between the rings at the crown. The number of

circumferential bolt failures varied between the tunnels and this was influenced by the localized relative movement between the segments in the common plane between rings. Figure 6.16 shows the contours of stress developed along the bolt before and after the bolt failures in Type 3 tunnel for load case 4N. As presented in Table 6.9, for load case 4N, Type 1 tunnel exhibited three circumferential bolt failures closest to the tunnel crown whereas Type 2 tunnel was free from the circumferential bolt failures. For load case 5N, Type 1, Type 2 and Type 3 tunnels displayed 10, 3 and 7 circumferential bolt failures respectively. Due to the influence of high flexibility in Type 3 tunnel, the tunnel ring closest to the explosive attracted more blast energy. This resulted in higher relative deformation in the closest ring with respect to the adjacent rings. The relative movement between the rings increased the number of circumferential bolt failures. As Type 1 tunnel is considerably rigid, the closest ring distributed the blast load to its adjacent rings through the common plane, in which a large number of the circumferential bolts failed in shear. However, in terms of the circumferential bolt failures, Type 2 tunnel displayed an intermediate response compared to Type 1 and Type3 tunnels.

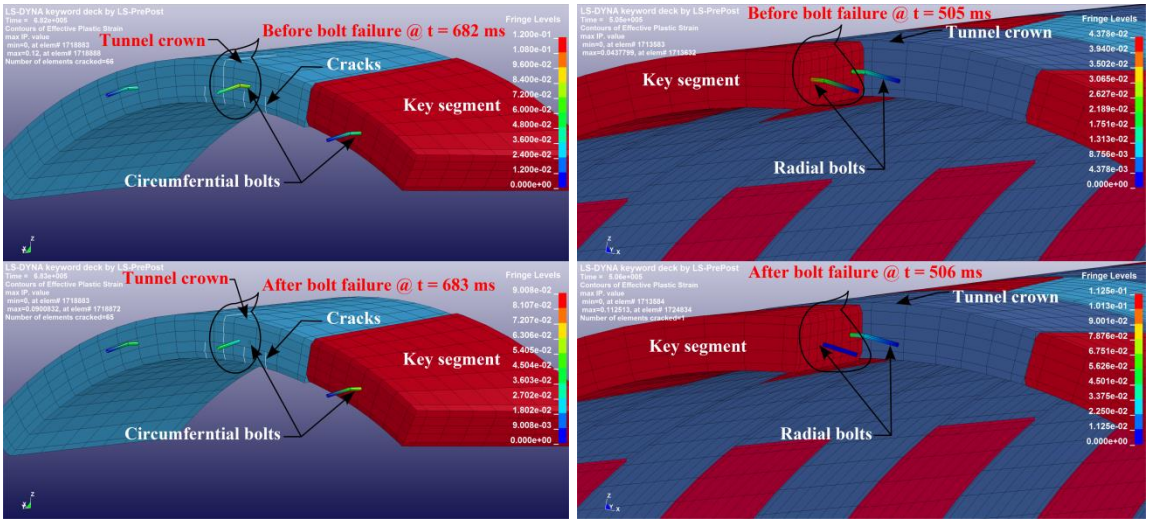

(a) First circumferential bolt failure (b) First radial bolt failure

Figure 6.16: View of bolt failure in Type 3 tunnel (Load case 4N)

Table 6.9: Numbers of circumferential bolt failure

	Case 1N	Case 2N	Case 3N	Case 4N	Case 5N
Type 1 (17 circumferential bolts/ring)	0	0	0	3	10
Type 2 (16 circumferential bolts/ring)	0	0	0	0	3
Type 3 (19 circumferential bolts/ring)	0	0	0	1	7

6.5 DISCUSSION OF NUMERICAL RESULTS

Comprehensive studies were carried out by varying several parameters affecting the blast response on a segmental tunnel buried in various homogenous soils. First, a tunnel having five segments plus a key segment in a ring was buried in different soil types, such as saturated soil, partially saturated soil and dry soil, to examine the effect of soil properties on the tunnel response. The study showed that the tunnel buried in the dry soil has higher peak diametric distortion than the tunnel in partially saturated soil. Though the intensity of shockwave is smaller in dry soil than the partially saturated soil, the deformation of the dry soil might be high due to poor bond between the soil grains and the soil skeleton which consists of a large amount of air causing high compressibility. Compared to other types of soils, the tunnel buried in the partially saturated soil displayed a quick residual distortion. The tunnel buried in the saturated soil was found to have the highest peak distortion and the tunnel suffered a large number of bolt failures.

The effects of joint types as well as the number of segments forming a ring were also investigated when the tunnel is buried in the saturated soil. The study showed that, for weaker/smaller blast loads ($\leq$250kg of TNT), the choice of joint types has a great impact on the blast response of the tunnel in terms of bolt failure and crack formation. However, for higher blast loads, the segments were damaged before activating the joint induced flexibility in the tunnel. There were no significant changes in the bolt failures and crack formation for higher blast loads, but the convex-concave joint sustained the tunnel profile by minimizing the drifting response at the joints. Flat joints were effective

in transferring the hoop stress and it encouraged friction induced shear resistance at the joints. The nosing elements making the periphery in convex-concave joint resisted shear force by mechanical interlocking of those elements and many elements failed after shockwave impact. While the flat joints are effective in transferring hoop stress at the joints, convex-convex joint resulted in less number of bolt failures and significant improvement in the crack response for weaker blast loading. Besides the joint responses to the blast loading, the benefits associated with constructability in terms of accommodating watertight gasket and less joint reinforcement outweigh the flat joint from other joints such as convex-concave joint and convex-convex joint.

A tunnel with seven segments (six segments plus a key segment) in a ring has resulted in very minimal drifting response compared to other types of tunnel up to 625kg of TNT explosive. There was a sudden reduction in the maximum crack widths as the number of segments increased from five segments (four segments plus a key segment) in a ring to six segments (five segments plus a key segment) in a ring. For example, the maximum crack width was reduced to 0.62mm from 1.46mm for 250kg of TNT explosive. However, as the number of segments further increased to seven segments in a ring, change in the maximum crack widths was insignificant. Although the tunnel with seven segments in a ring displayed less radial bolt failures, the numbers of circumferential bolt failures were significantly higher than the tunnel with six segments in a ring.

6.6 CHAPTER SUMMARY

In this chapter, the effect of crucial parameters on the tunnel response under surface blast provides another perspective to the study of segmental tunnels. The influence of the surrounding soil properties and geometrical characteristics of the segmental tunnel lining were investigated. First, a commonly used single tube tunnel having six segments (five segments plus a key segment) was used to examine the effect of soil properties on the tunnel response. The tunnel buried in saturated soil, partially saturated soil and dry soil were considered. Secondly, the influence of segment geometry was studied with respect to the joint types and the number of segments forming the ring. The main findings of this chapter are as follows:

1. The blast response of buried tunnel in saturated soil is more severe in terms of crack formation and bolt failures than the tunnel buried in either partially saturated soil or dry soil when subjected to the same surface explosion.

2. In all soil conditions, the diametric distortions increase with the explosive mass and the distortions are unrecoverable in all load cases (from 250 to 1250kg of TNT). As the explosive mass increased to more than 750kg of TNT, the tunnel buried in the saturated soil displayed segment-disintegration from neighbouring segments.

3. For weaker blast loads ($\leq$250kg of TNT), joint types influenced the tunnel response by allowing the segments to rotate about the joints, whereas for higher blast loads, the segments were damaged before triggering the flexibility of the joints.

4. While the flat joints are effective in transferring hoop stress at the joints, convex-convex joint resulted in less number of bolt failures and significant improvement in the crack response for weaker blast loading.

5. As the number of segments increased in a ring, the maximum crack width decreased. However, as the number of segments further increased to seven segments (six segments plus a key segment) in a ring, it did not make much difference in the magnitude of the maximum crack width.

6. Although the tunnel with seven segments in a ring displayed less radial bolt failures, the numbers of circumferential bolt failures were significantly more than the tunnel with six segments in a ring.

Chapter 7: Blast impact and mitigation measures

7.1 INTRODUCTION

The dynamic behaviour of the tunnel under the influence of a series of surface blast loads were previously investigated by varying a number of parameters, such as soil types, joint types and number of segments in a ring. Blast induced ground shock had a high level of impact on the performance of buried tunnel structures. This chapter considers damage evaluation factors such as cracks in the segments, bolt failure, drifting or sliding of segments against each other. The tunnel failure may be driven by a single factor or by a combination of several factors. These factors are discussed in this chapter along with mitigation measures that could be implemented to minimize the blast impact.

This chapter begins by analysing the blast response of the buried tunnel in saturated soil with clay composition (Table 6.1) under a number of parametric conditions; soil cover (tunnel depth), distance of explosive from the tunnel centreline (ground distance) and explosive weight. Critical factors identified from the sensitivity study are considered to mitigate the blast effect by the following measures:

1. wrapping the tunnel with a flexible and compressible barrier consisting of a layer of polyurethane foam;
2. wrapping the tunnel with a secondary in-situ reinforced concrete lining;
3. use of Steel Fiber Reinforced Concrete (SFRC) in precast segments;
4. energy absorbing flexible honeycomb elements;
5. introducing a buster slab between the tunnel crown and the ground surface.

In the first two measures, the space between the bored soil face and the lining is filled using the protective barrier materials which are in contact with the tunnel surface. As a third measure, Steel Fiber Reinforced Concrete (SFRC) is used instead of conventional reinforced concrete segments to produce the tunnel segments. Deformable honeycomb-type cell elements are introduced at the radial joints as a fourth measure in order to

absorb a considerable amount of blast energy. Finally, as an external measure, a buster slab is placed between the tunnel crown and the explosive in order to combat the shockwave before reaching the target.

7.2 THE EFFECT OF TUNNEL DEPTH AND STAND-OFF DISTANCE IN BLAST IMPACT

There are numerous empirical relationships relating stand-off distance to blast effects from various explosive weights for free-field explosions (Department of the Army, 1986 and Yankelevsky et al., 2011). However, the relationship between stand-off distance and the segmented tunnel response due to a surface blast are not reported. There is no established guidance for predicting either the tunnel response or the characteristics of the blast loading. In this section, the effects of tunnel depth, ground distance and explosive weight on the tunnel response are studied. Figure 7.1 (a) shows that the tunnel depth is varied from 6.35m (= 1D) to 12.70m (= 2D), and the ground distance is varied from the tunnel centreline to 12.70m (= 2D) as shown in Figure 7.1(b). As described in Table 5.1, the cylindrical disk type explosive weight is varied from 250 to 1250kg of TNT.

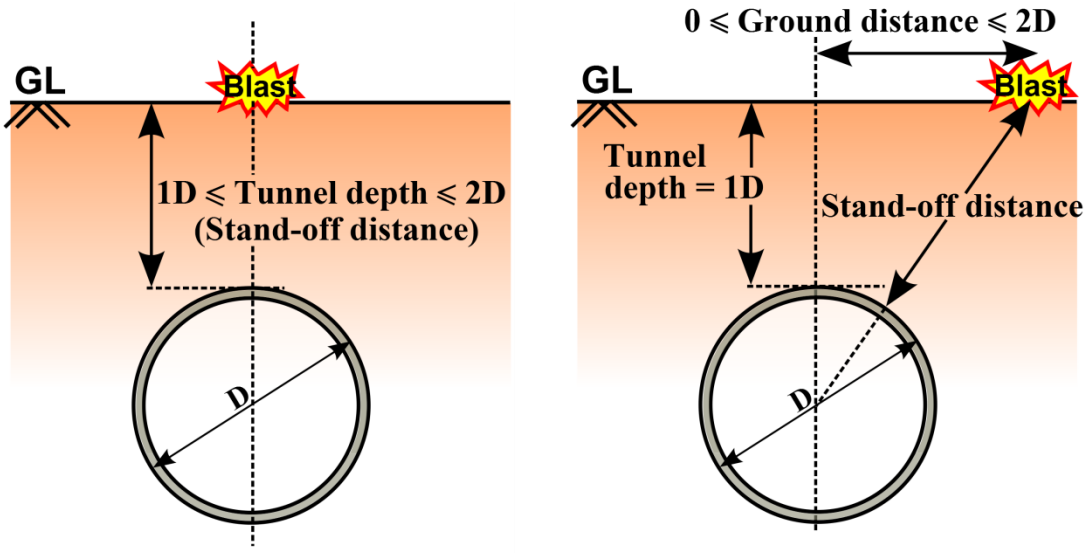

(a) Variation of tunnel depth (b) Variation of ground distance

Figure 7.1: Variation of tunnel depth and ground distance

Cracks in segments, bolt failure and drifting response are considered in this study as

critical factors to evaluate the blast performance of the tunnel structure. The damage state of tunnels can be divided into the following four groups:

1. no damage (the tunnel is considered to behave elastically with some minor cracks in segments (maximum crack width < 0.3mm) and no bolt failure);
2. slight damage (a small number of cracks exceeded the crack limiting value of 0.3mm and a few incidents of bolt failure at joints, but the drifting response is insignificant);
3. moderate damage (a large number of cracks exceeded the crack limiting value of 0.3mm, a large number of failed bolts triggered significant drifting or sliding of segments at joints, however, the tunnel remains functional by keeping the in-plane tunnel profile due to hoop compression);
4. severe damage or collapse (formation of fully depth cracks, large number of bolt failures resulting in large drifting between segments).

The damage state rises as intensity of shockwave impacting the tunnel increases. Low-energy blast impact causes no and slight damages in the tunnel lining while high-energy blast impact causes moderate and severe damages.

In the present study, more than 30 models were considered to identify critical situations under the influence of tunnel depth, ground distance and explosive weight, but only a few important results are shown in this section. Figure 7.2 illustrates the failure modes of the tunnel under a load of 750kg of TNT (Load case 3 refers to Table 5.1) at different tunnel depths. It can be seen that the tunnel depth showed significant influence on the failure modes of the tunnel when the surface explosive was directly above the tunnel crown. For the tunnel depth of 6.35m (1D), the tunnel was severely damaged with wide and deep cracks, segments were crushed and drifted away from the adjacent segments and a large number of bolts failed as shown in Figure 7.2(a). There was not much difference in the tunnel buried at depth 2D in terms of number of bolt failures. However, when referring to damage due to the crack, a significant change in the crack response retained its in-plane tunnel profile without large drifting between segments as displayed in Figure 7.2(b). The damage level corresponds to the state of “moderate damage”. As the depth further increases to 2D, the tunnel responded with very small

cracks, in which the maximum crack width was 0.24mm, less than the crack limiting value of 0.3mm. From this point of view, it is appropriate to say that the tunnel is safe with "no damage".

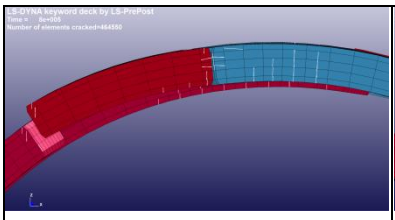	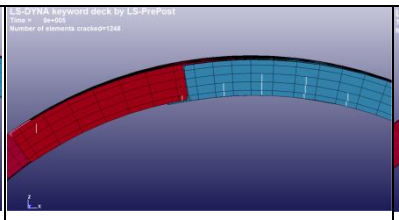	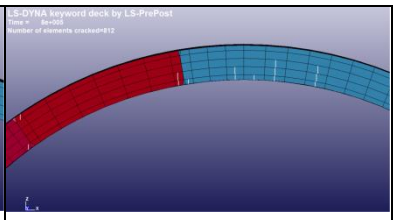
(a) Depth = 1D	(b) Depth = 1.5D	(c) Depth = 2D
Max. crack width = 2.20mm	Max. crack width = 0.57mm	Max. crack width = 0.24mm
Nos. of cracks (>0.3mm) = 81674	Nos. of cracks (>0.3mm) = 60	Nos. of cracks (>0.3mm) = 0
Nos. of bolt failure = 35	Nos. of bolt failure = 10	Nos. of bolt failure = 0
Severe damage	Moderate damage	No damage

Figure 7.2: Failure modes of the tunnel under different tunnel depths (load case 3)

Table 7.1 compares the damage scenarios for the tunnel based on the drifting response, maximum crack width and corresponding numbers of bolt failures under a series of explosives from case 1 (250kg of TNT) to case 5 (1250kg of TNT). For the first two damage states, the drifting response is insignificant, although few radial bolts failed resulting in "slight damage" state. The combined effect of the cracking and bolt failure influenced the drifting response in "severe damage" state where the crown segments were severely drifted with respect to the adjacent segments in both longitudinal and transverse directions. This resulted in a significant number of circumferential bolt failures beyond load case 3 for the tunnel depth of 6.35m (1D). There were no circumferential bolt failure in both depth 1.5D and depth 2D in all load cases. The segments were slightly drifted and stabilized in "moderate damage" state while maintaining the in-plane tunnel profile.

Table 7.1: Maximum crack width in mm / nos. of bolt failures

Depth	Case 1	Case 2	Case 3	Case 4	Case 5
Depth 1D	0.62 / 4	0.97 / 11	2.20 / 35	3.00 / 45	4.40 / 63
Depth 1.5D	0.20 / 0	0.37 / 2	0.57 / 10	0.60 / 17	0.90 / 32
Depth 2D	0.15 / 0	0.21 / 0	0.24 / 0	0.36 / 2	0.54 / 6

: No damage : Slight damage

: Moderate damage : Severe damage

Figure 7.3 compares the failure modes of the tunnel under load case 3 at different ground distances for a specified tunnel depth of 6.35m (1D). The cracks on the segments were observed from different ground distances. The ground distance from the explosive has a significant influence on the damage response, which is similar to the tunnel response due to the variation of the tunnel depth. As compared in Table 7.2, there were no bolt failures at a distance of 12.70m (2D) for load cases 1 to 4. In load case 5 for a distance 2D, the tunnel displayed considerable drifting between segments.

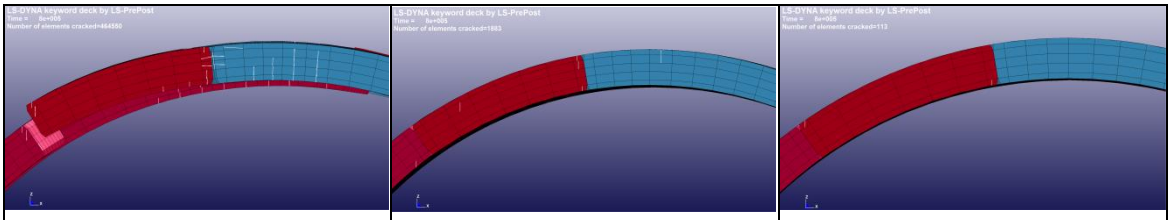

(a) Distance = 0	(b) Distance = 1D	(c) Distance = 2D
Max. crack width = 2.20mm	Max. crack width = 0.40mm	Max. crack width = 0.10mm
Nos. of cracks (>0.3mm) = 81674	Nos. of cracks (>0.3mm) = 34	Nos. of cracks (>0.3mm) = 0
Nos. of bolt failure = 35	Nos. of bolt failure = 4	Nos. of bolt failure = 0
Severe damage	Moderate damage	No damage

Figure 7.3: Failure modes of the tunnel under different ground distances (load case 3)

Table 7.2: Maximum crack width in mm / nos. of bolt failures

Distance	Case 1	Case 2	Case 3	Case 4	Case 5
Distance 0	0.62 / 4	0.97 / 11	2.20 / 35	3.00 / 45	4.40 / 63
Distance 1D	0.10 / 0	0.31 / 0	0.40 / 4	0.46 / 11	0.65 / 21
Distance 2D	0.01 / 0	0.07 / 0	0.10 / 0	0.35 / 0	0.60 / 2

: No damage : Slight damage

: Moderate damage : Severe damage

The effects of explosive weight versus stand-off distance of the tunnel were used to plot different damage zones for two situations described in Figure 7.1. Figure 7.4(a) depicts the variation of damage states due to the influence of the tunnel depth, in which the stand-off distance is equal to the tunnel depth. Three critical lines are drawn using best-fitting lines to divide the boundary between different damage zones. Some intermediate coordinates were selected and relevant simulations were carried out to fine-tune the critical lines. The following equations mathematically express the relationship between the stand-off distances to the explosive weight:

$$\left.\begin{aligned} \text{Line}\,1: R &= 2.94\ln(w) - 6.78 \\ \text{Line}\,2: R &= 3.94\ln(w) - 15.02 \\ \text{Line}\,3: R &= 5.40\ln(w) - 28.42 \end{aligned}\right\} 6.35m \le R \le 12.70m \qquad \text{Equation 7.1}$$

where R is the stand-off distance in m, w is the explosive weight in kg.

Line 1 illustrates the threshold border between no damage zone to slight damage zone, points on the left side of the line produces no damage in the tunnel lining. Line 2 depicts the threshold border between slight damage zone to moderate damage zone. The coordinates between Line 1 and 2 denotes that the tunnel exhibited minor cracks with few bolt failures. Under slight damage, the tunnel can return to operation after some surface repairs. The third line divides the moderate and the severe damage zones. The region between Line 2 and 3 produces moderate damage. Table 7.1 shows that 250kg of TNT explosive can cause moderate damage on shallow buried tunnels. In addition to

deep and wider cracks, the tunnel segments suffered a large number of bolt failures causing drifting or sliding displacement between segments. It may be considered that those affected segments are at risk of failing. Furthermore, infiltration of water and soil through the joints can alter the surrounding ground condition and speed up the damage state. This may require complete replacement of affected segments. Replacing segments are often associated with time consuming labour and in turn correspondingly cost intensive repair work.

The right side of Line 3 illustrates that the combination of explosive (w) and stand-off distance (R) resulted in very severe damage to the structural integrity of segmented lining. The most severe damage state associated with deep and wider cracks and several bolt failures. The cracks extended from the bottom of interior surface to top of the segments due to high bending stresses developed from the explosion. Several bolt failures caused drifting between segments at the radial joints. When the drifting exceeded a certain degree, the segments lost contact hoop force transmission capacity at those radial joints. As a result, the segmented lining was subjected to progressive collapse as displayed in Figure 7.2(a).

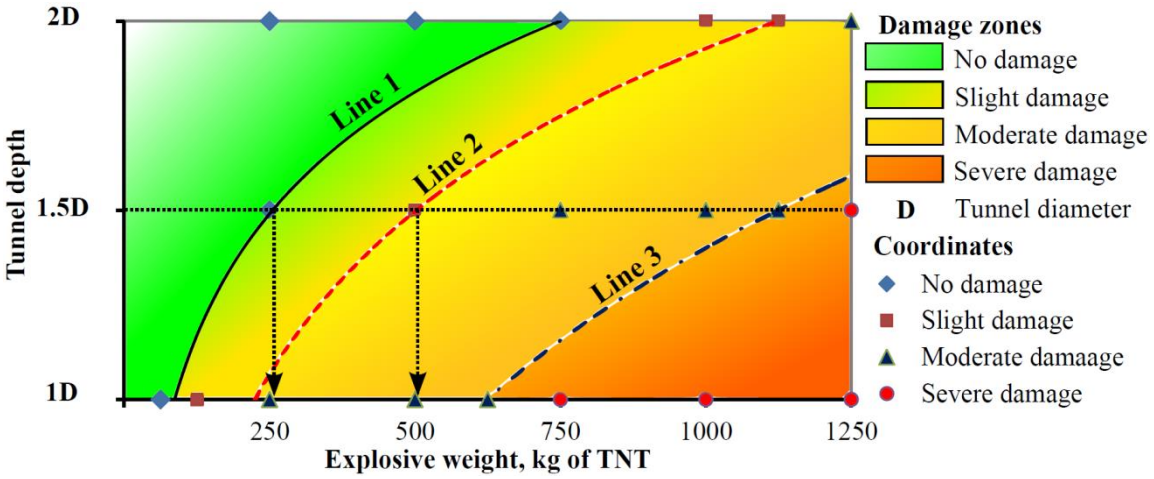

(a) Explosive weight vs tunnel depth for different damage state

Figure 7.4: Critical explosive weight vs. stand-off distance for different damage state

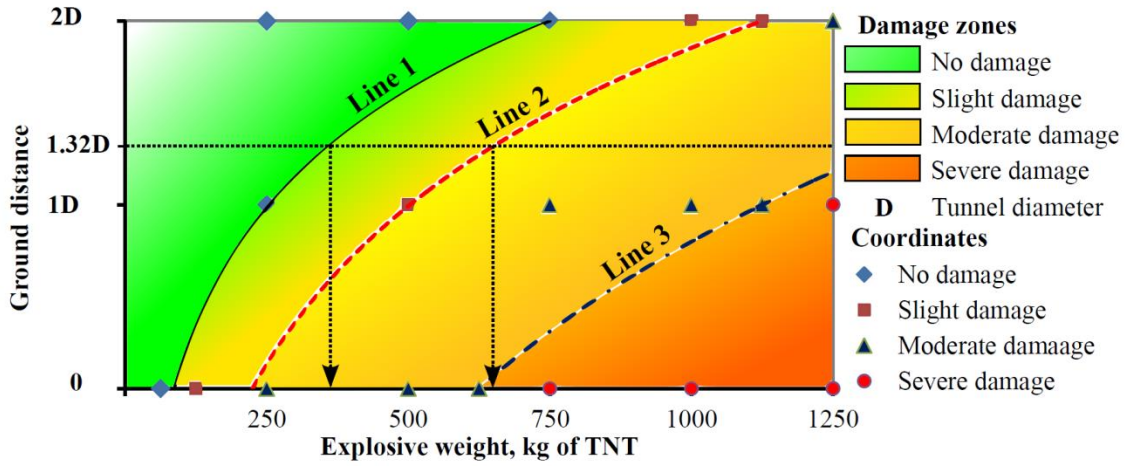

(b) Explosive weight vs ground distance for different damage state

Figure 7.4: Critical explosive weight vs. stand-off distance for different damage state

A ground distance of 1.32D in Figure 7.4 (b) is equivalent to the stand-off distance of 1.5D (tunnel depth of 1.5D in Figure 7.4 (a)). Two critical explosive weights for stand-off distance of 1.5D corresponding to Line 1 and Line 2 are projected as shown in Figure 7.4(a). The projected values for Line 1 & 2 are 250 and 500kg of TNT respectively. Similar arrows shown in Figure 14 (b) denote that those values for Line 1 & 2 are significantly greater than 350 and 650kg of TNT respectively. For the same scaled distances, the study shows that the tunnel is more vulnerable to the surface explosion from the explosive placed on the centerline of the tunnel than any other locations on the surface. When the shockwave impacted the tunnel, the sideways component of the shockwave influenced the tunnel motion in a direction perpendicular to the ground surface. Due to shallow soil cover above the tunnel crown, the tunnel is more flexible in crown-invert direction than the lateral direction as the infinite soil medium constrains the tunnel in the lateral direction. In addition, the previous study in section 4.2.5 demonstrates that shallower gauge points experienced slightly small peak pressure than the corresponding gauge points directly below the explosive.

Furthermore, Figure 7.4 (b) assists in developing a protection and safety zone in order to reduce detrimental effects of any possible surface explosions. Incorporation of proper and adequate precaution/protection measures by restricting any activities within the zones will protect the tunnel from credible blasts. For example, the study shows that the introduction of a safety zone 1.0D distance from the tunnel centerline completely

protects the tunnel from an explosion caused by car bombs and the tunnel is even safe with slight damages if the explosion is caused by SUV/van bomb (Table 1.1).

7.3 MITIGATION OF BLAST IMPACT USING DIFFERENT APPROACHES

The previous study demonstrated that the surface explosive placed directly above the tunnel crown creates detrimental effects to the tunnel. In this section, different mitigation measures as described in Section 7.1 are considered to minimise the tunnel damage induced by the surface explosion.

7.3.1 Wrapping the tunnel with flexible and compressible barrier consisting of a layer of polyurethane foam.

The efficacy of a protective barrier material in mitigating the blast effects on the buried tunnel is studied in this section where a compressible porous barrier consisting of a layer of polyurethane foam is installed around the tunnel. The barrier material is placed into the space between the bored soil face and the lining. In the conventional tunnel, the space is filled by annulus concrete grout.

The polyurethane layer was approximated as isotropic, nearly incompressible, and hyperplastic rubber material. The constitutive behaviour was described with the formulation of Blatz and Ko (1962). This material is considered to be rate-independent and implemented in LS-DYNA as MAT_BLATZ-KON_RUBBER which was used for treating the blast response of sandwich structures (Bahei-El-Din & Dvorak, 2007). Material properties of polyurethane foam (Appendix B) used in the study were provided by De et al. (2013).

Figure 7.5 compares the crack responses of the tunnel with concrete grout and the tunnel with polyurethane foam after 300ms of explosion. In this study, the tunnel depth and explosive weight were 6.35m (1D) and 250kg of TNT respectively. The tunnel, with concrete grout displayed moderate damage where the maximum crack width and number of bolt failure were 0.62mm and 4 respectively, whereas the tunnel with polyurethane exhibited no damage with allowable minor cracks of 0.1mm.

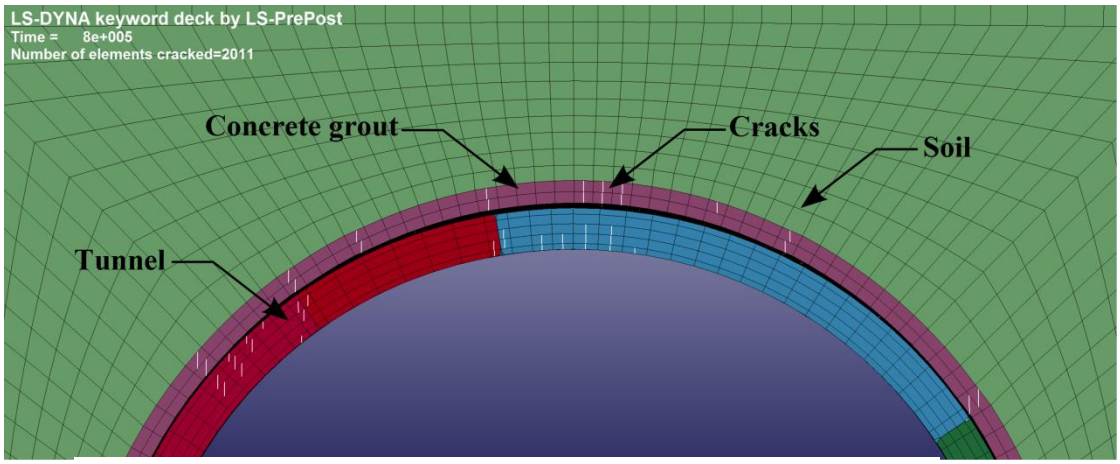

(a) Crack response of conventional tunnel with concrete

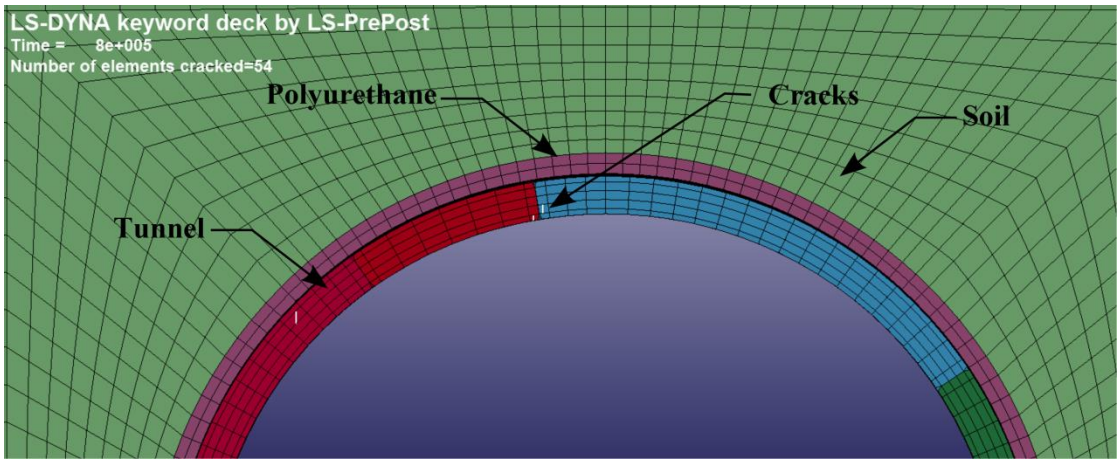

(b) Crack response of tunnel with polyurethane

Figure 7.5: Comparison of crack response of tunnels (Load case1 and depth=1D)

The total energy imparted by the shockwave to the tunnel structure is converted into kinetic energy and strain energy. The strain energy includes elastic strain energy and plastic strain energy due to permanent deformation. The elastic strain is kept mainly in the inner elements in the segments. Energy dissipation occurs in the crushable polyurethane foam.

Figure 7.6(a) compares the time histories of the total kinetic energy of the tunnel structure (total tunnel length of 25.2m) considering the above-defined situation. The reported energy magnitudes in figures refer to the total volume of segments, reinforcement, bolts and polyurethane foam. The exterior concrete grout exhibited immediate permanent crushing with cracks due to blast induced ground shockwave. Therefore, the conventional tunnel with concrete grout displayed a sharper increase in the total kinetic energy (at a peak value of 2300kJ) than the tunnel with polyurethane. Replacement of polyurethane (instead of

concrete grout) reduced the maximum total kinetic energy by 300kJ. The total strain energy computed in both cases is compared in Figure 7.6(b). Both cases show an initial peak before reaching the residual total strain energy. During the peak, the tunnel with polyurethane dissipated significantly more strain energy by the polyurethane foam during localized plastic deformation. After the peak, the tunnel with concrete grout dissipated a large amount of strain energy in the tunnel by cracking of the segments as it is evident from the comparison of cracks in Figure 7.5. This was reduced by about 50% in the tunnel with polyurethane, which is entirely due to the polyurethane layer around the tunnel. Therefore, the behaviour of the tunnel with polyurethane shows better energy absorption over the conventional tunnel.

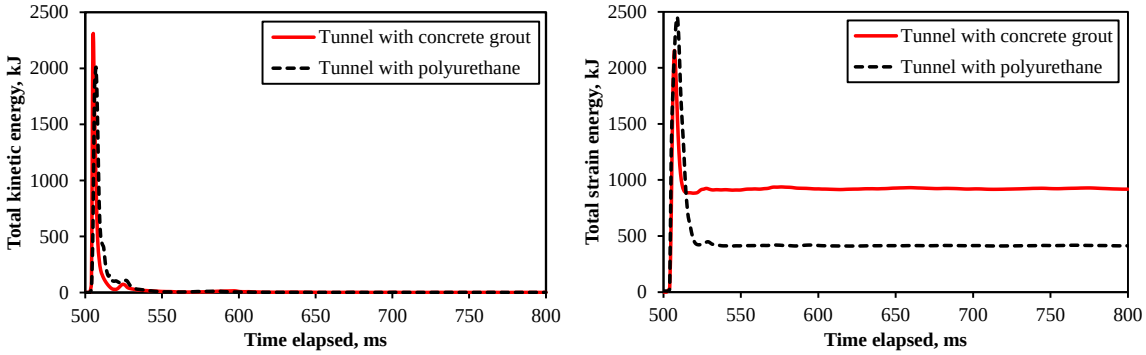

(a) Kinetic energy vs. time (b) Strain energy vs. time

Figure 7.6: Time history of total kinetic and strain energies

Figure 7.7 illustrates how the critical lines defining the damage zones move with the introduction of protective barrier of polyurethane foam around the tunnel. The arrow indicates the line of improvement. Figure 7.7 clearly depicts the improvement in the tunnel protection in first three damage zones compared to Figure 7.4 (a). Lower part of Line 1 moved to the right-hand-side about the coordinate of (750, 2D) as Line1_Poly. A similar trend was observed in Line 2 where the slight damage zone moved to a higher order of explosive range. This resulted in a significant reduction in the moderate damage zone compared to the conventional tunnel with concrete grout. However, there was no difference in the severe damage zone.

In the severe damage zone, though the tunnels showed significant improvement in terms of crack response at a micro level, the tunnel failure is triggered by a significant increase in

number of bolt failures in macro level. The immediate ring attracted more blast shock pressure through the barrier material as the polyurethane is more flexible than the concrete grouting material in the conventional tunnel. As a result, a large number of circumferential bolts failed in the immediate ring joint.

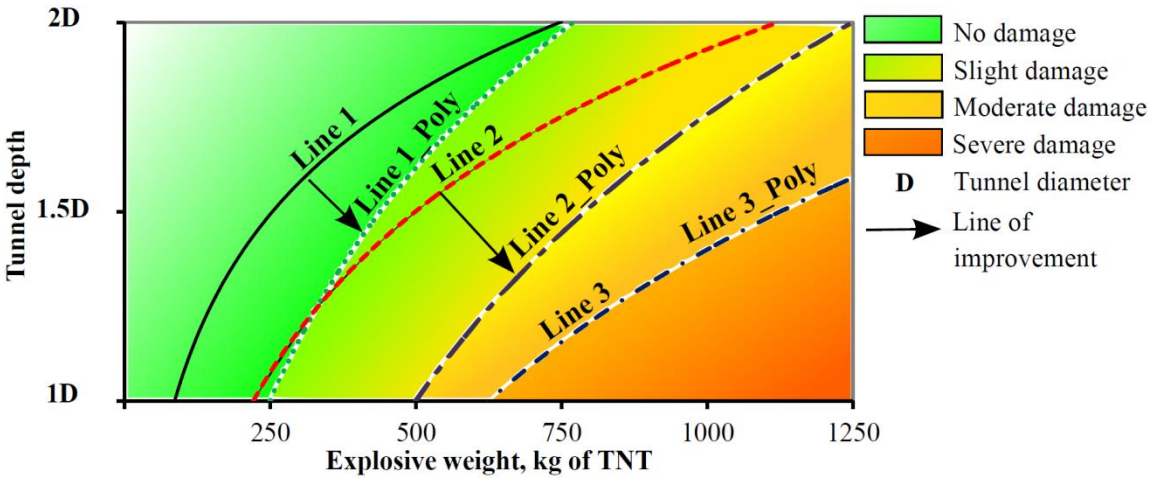

Figure 7.7: Critical explosive weight vs. tunnel depth for polyurethane foam

7.3.2 Wrapping the tunnel with a secondary in-situ reinforced concrete lining

A similar study as described in the previous section was considered by replacing the concrete grout with in-situ reinforced concrete, which acts as a secondary lining to the segmented tunnel. For the secondary lining, the same grade of concrete as used for the precast segments was considered. The secondary lining was 150mm thick and double reinforced with 10mm diameter rebars at 175mm spacing in both circumferential and transverse directions with 10mm diameter shear links. A similar modelling technique to that used for the primary segmented lining was used to model the secondary lining.

Both flexible and rigid protective barrier materials provide an adequate level of protection of the tunnel. Figure 7.8 compares the shockwave interaction with those barrier materials at different times after the explosion. Propagation of the shockwave through the soil is visible in two separate situations. At t = 504ms (Figures 7.8(a) & (b)), the shockwave impacted on the barrier materials. When the shockwave impacted on the barrier materials, the compression shockwave expanded on the surface of the flexible polyurethane barrier as shown in Figure 7.8(a). The compression shockwave reflecting from the polyurethane barrier resulted in a temporary stage of wave

stagnation around the tunnel crown as depicted in Figure 7.8(b) whereas, in the rigid RC barrier, the reflected shockwave was quickly moved out of the surface as displayed in Figure 7.8(d).

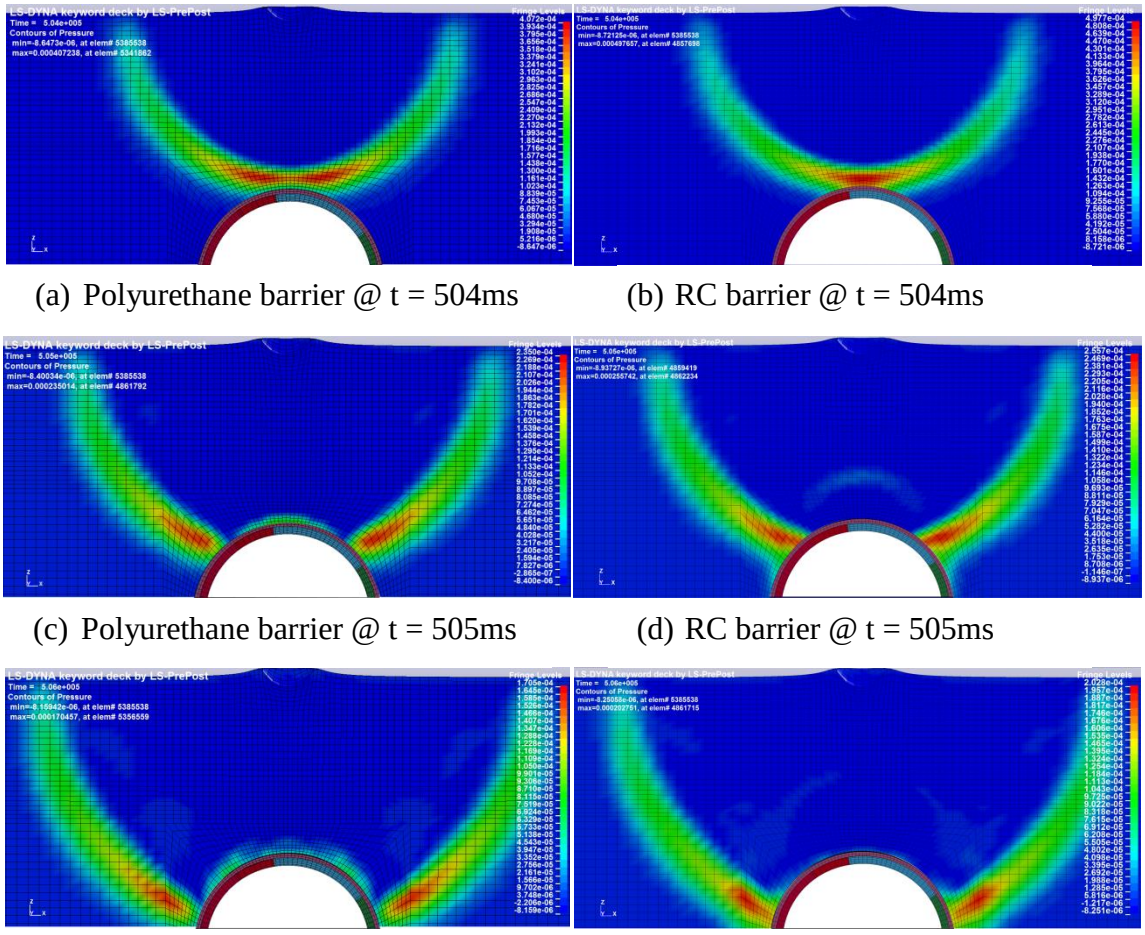

(a) Polyurethane barrier @ t = 504ms (b) RC barrier @ t = 504ms

(c) Polyurethane barrier @ t = 505ms (d) RC barrier @ t = 505ms

(e) Polyurethane barrier @ t = 506ms (f) RC barrier @ t = 506ms

Figure 7.8: Comparison of shockwave interaction with the barrier materials

While the flexible barrier material provides protection by allowing the material to deform and absorb the blast energy, the rigid RC barrier provides passive blast protection by allowing material to crack and reflect the shockwave. Figure 7.9 illustrates that the RC barrier protected tunnel against low-energy blast impact. The critical Line 1 equally moved to the right by expanding the no damage zone while shrinking the slight damage zone. Changes in the moderate damage zone are insignificant. Mitigation measure by replacing the concrete grout by the secondary RC layer has not altered the severe damage zone, although the numbers of circumferential bolt failures were significantly reduced by the grater load distribution capacity of the secondary layer.

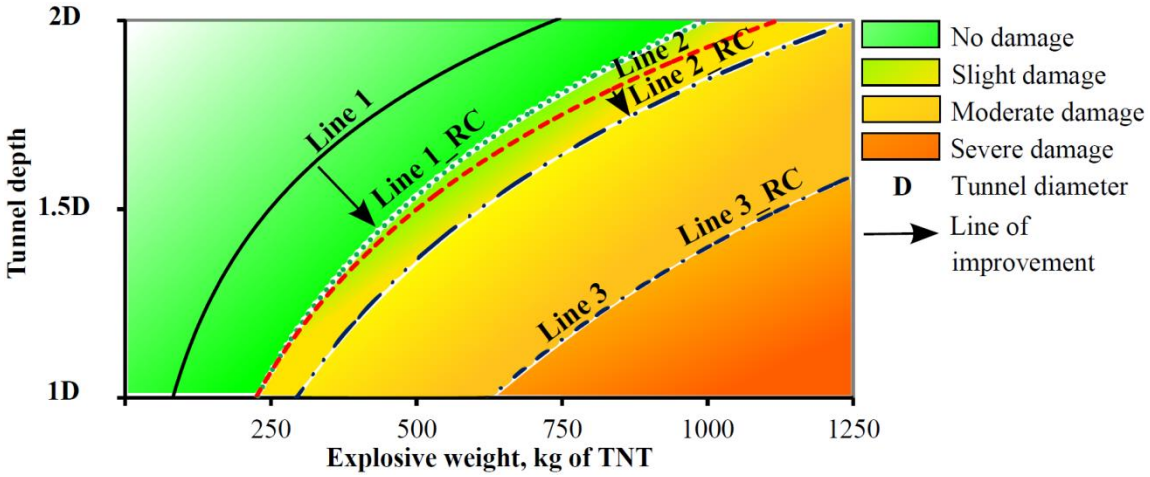

Figure 7.9: Critical explosive weight vs. tunnel depth for Reinforced Concrete secondary lining

7.3.3 Replacing Reinforced Concrete (RC) segments by Steel Fibre Reinforced Concrete (SFRC) segments.

This section examines how the tunnel responds to the surface blast when its segments are generated from Steel Fibre Reinforced Concrete (SFRC) without rebars. A similar model described in the earlier section was considered. SFRC was modelled using the same material model of MAT_WINFRITH_CONCRETE which was validated and used for treating the blast response of SFRC slab (Ågårdh, 1997). SFRC material parameters for the segmental lining are provided by Beňo and Hilar (2013) as shown in Table 7.3.

Table 7.3: Material properties of SFRC

Parameter	Value
Density (g/cm^3)	2.29
Unconfined compressive strength (MPa)	57.2
Tensile strength (MPa)	4.2
Poisson's ratio	0.2
Specific fracture energy (N/m)	7500

After shockwave impact on the tunnel, a number of cracks were visible in the concrete grout whereas no cracks appeared in the segments for all load cases because of higher

fracture energy and tensile strength. Figure 7.10 shows the crack formation at the end of the simulation for Load case1 (refers to Table 5.1) and depth=1D. The tunnel segments were deformed while keeping the numbers of bolt failures small than the conventional RC segmented tunnels. For instance, the tunnel buried at a depth of 6.35m showed only one radial bolt failure for load case 1 whereas the tunnel with RC segments displayed four bolt failures for the same situation.

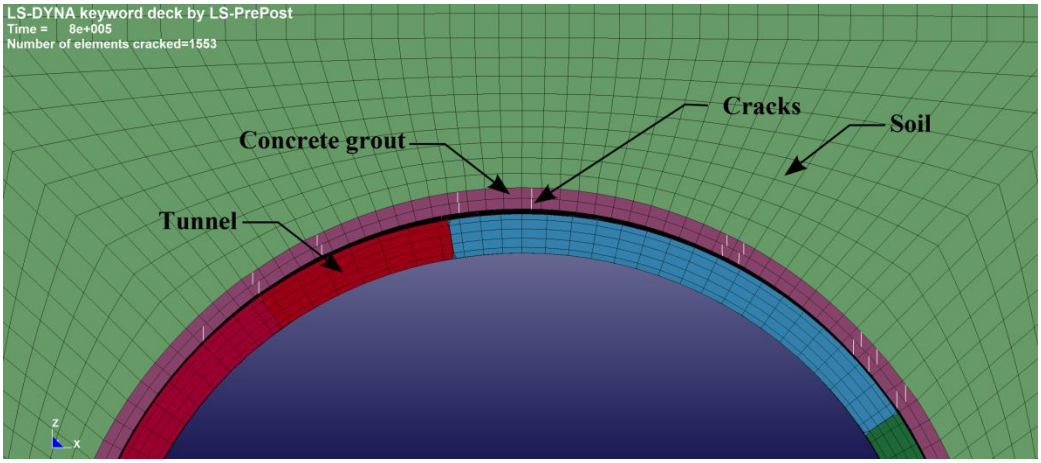

Figure 7.10: The crack response of SFRC tunnel (Load case1 and depth=1D)

As the intensity of the shockwave impacting the tunnel increased, SFRC segments displayed rigid response compared to the RC segmented tunnel. The dynamic response of the tunnel lining is governed by the flexural stiffness defined as *EI* where *E* is the Young's modulus and *I* is the second moment of area. Though *E* is nearly the same for both segments, excessive crack width opening in RC segments largely reduced its *I* value and resulted in increased flexibility in RC tunnel response. Figure 7.11 shows the influence of the critical lines by replacing the conventional RC with SFRC segments. The movement of Line 1 to the right displayed a great expansion in the area of no damage zone. Similarly, the movement of Line 2 shifted the slight damage zone to the right. As a result, the moderate damage zone significantly shortened. For instance, (750, 1.5D) coordinate in the moderate damage zone is moved to slight damage zone due to the replacement of SFRC segments. However, there was no change in severe damage zone.

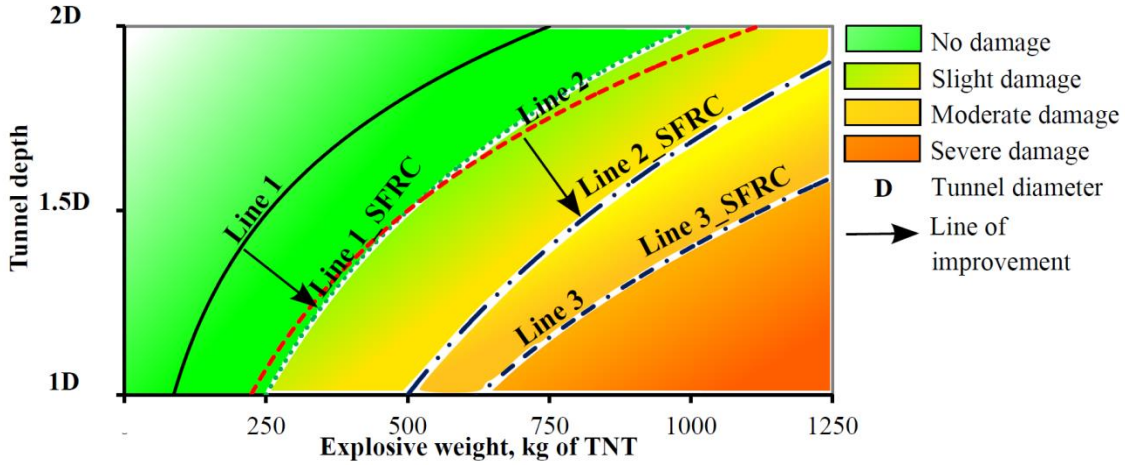

Figure 7.11: Critical explosive weight vs. tunnel depth for SFRC lining

7.3.4 Introducing energy absorbing flexible honeycomb elements between radial joints.

In the bored tunnels, there are no flexible (compressible) elements of type used in conventional tunnelling. However, in this section, an adjustable lining system has been developed and applied based on honeycomb flexible (compressible) elements principle in order to minimise the blast effects on the segments by allowing them to expand along the circumference and rotate about the joints. The flexible (compressible) elements are expressly used to take up the blast load in order to reach equilibrium before the segments are damaged. The parts consisting of the flexible elements can be integrated into the segment on one side or on both sides and they form a complete segment ring as shown in Figure 7.12.

In this case, every single flexible part was incorporated into the segment on right side (circling the ring in clockwise direction) and the flexible part was cast together with appropriate anchor keys into the segment. The other side of the flexible part was connected to the segment face using bolts during the installation. The radial bolts were M24 grade 8.8 straight bolts. The ring joints were similar to the conventional tunnel. The flexible parts were made of a series of cells that were assembled using welded vertical and horizontal 4 mm thick mild steel plates as shown in Figure 7.12(a).

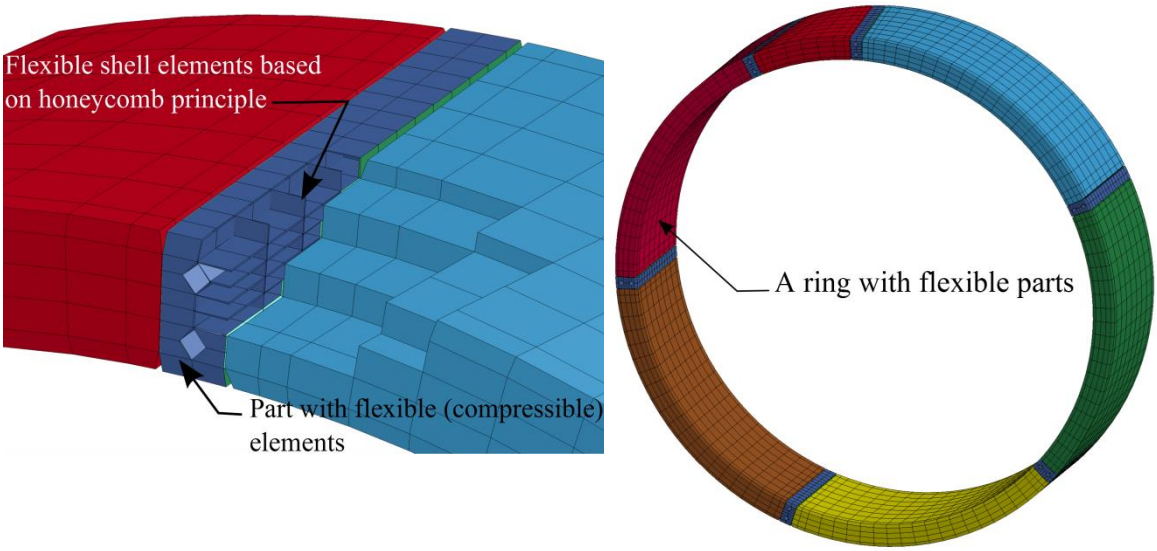

(a) Cut section of a flexible part (b) A ring with flexible parts

Figure 7.12: Arrangement of flexible parts in a ring

The mild steel plates were modelled as shell elements using MAT_PLASTICIY_KINEMATIC material model. The fitted faces between the segments and the flexible parts were simulated using CONTACT_TIED_NODES_SURFACE_OFFSET type contact whereas the free surfaces (at the radial joint) between the segments and the flexible parts were modelled using CONTACT_AUTOMATIC_SURFACE_TO_SURFACE type contact. As one end of the bolt was bolted to the flexible part, the connection was considered as fully fixed.

Figure 7.13 shows the blast influence diagram by varying both the explosive mass and tunnel depth with the introduction of flexible honeycomb elements between the radial surfaces of the segments. It can be clearly seen that the no damage zone has significantly increased. In this zone, deformation of flexible parts dominated the global deformation. The flexible parts were crushed and deformed in the circumferential direction in order to allow the neighbouring segments to expand and rotate at their radial interface. After reaching a state of equilibrium, the segments started to crack due to combined bending and hoop stresses. Crushing of flexible elements has significantly delayed the commencement of crack propagation in the segments compared to the conventional segmental lining.

As the intensity of shockwave impacting the tunnel increased, both the flexible parts and segments responded simultaneously to the blast load, resulting in no improvement in the

crack response. In this tunnel, the flexible parts were not only deformed due to the circumferential hoop stress, but also due to the shear force transmission at the radial joints. The shear deformation of the flexible part in the radial direction has significantly reduced the number of radial bolt failures. For example, the coordinate (250, 1D) in the conventional tunnel denoted 0.64mm maximum crack width and four number of bolt failures. With introduction of flexible parts, the same coordinate moved to slight damage zone as it displayed 0.6 mm maximum crack width and no bolt failures. Figure 7.14(a) illustrates the deformed tunnel profile and the closest flexible part showed significant plastic damage. As shown in Figure 7.13, the slight damage zone displayed a slight improvement as the difference between Line 2 and Line 2_Honey are insignificant.

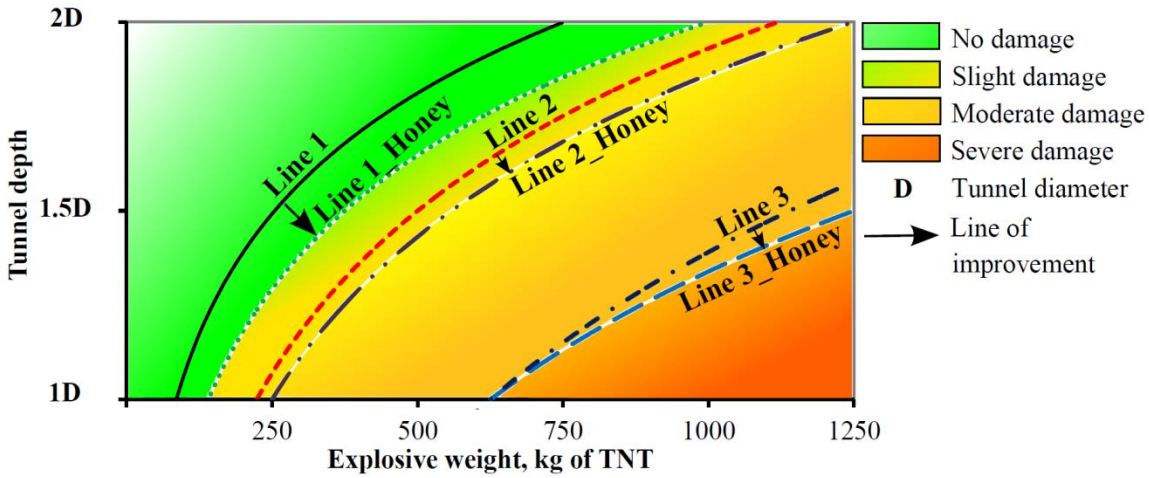

Figure 7.13: Critical explosive weight vs. tunnel depth for flexible honeycomb elements

In the severe damage zone, immediately after the explosion the segments were damaged before the flexible parts deformed and absorbed significant amount of blast energy. After that, the segments together with the flexible parts resisted the blast load. Crushing of the flexible parts in the circumferential direction increased the segments' bending ability. As a result, segments displayed a large number of deep and wider cracks. For example, a tunnel with 1D depth under 750kg of TNT surface explosive displayed a large number of full depth cracks as shown in Figure 7.14(b). The similar situation in the conventional tunnel displayed a large drifting between the crown segments as shown in Figure 7.2(a). However, in this case, the drifting response is significantly reduced due to the introduction of the flexible part which deformed in the radial direction, but saved the number of radial bolt failures. As the blast response is severe in terms of the overall

crack response compared to the conventional tunnel, the coordinate (750,1D) is still in the severe damage zone. As displayed in Figure 7.13, increased soil confinement of the tunnel buried at 1.5D depth slightly reduced the upper limit of the severe damage zone.

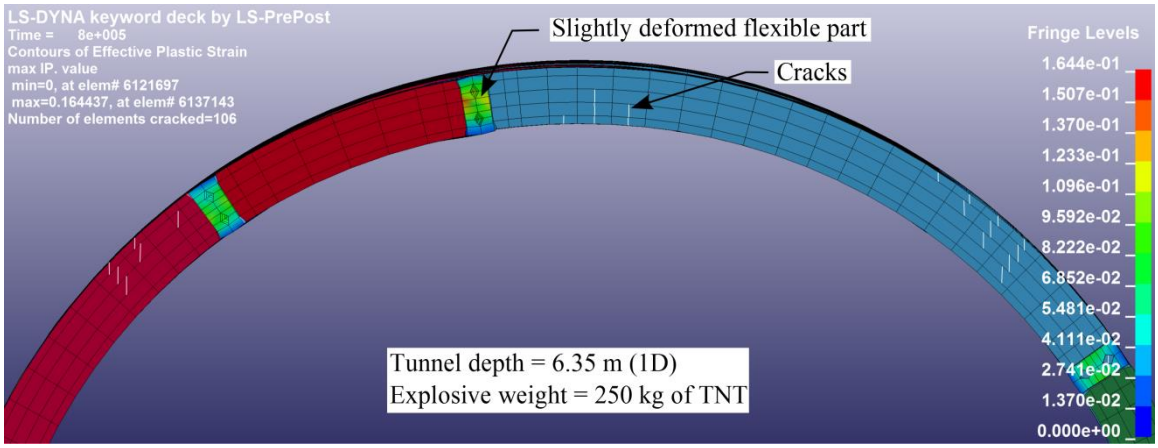

(a) Deformed shape of the tunnel buried in 1D depth for load case 1

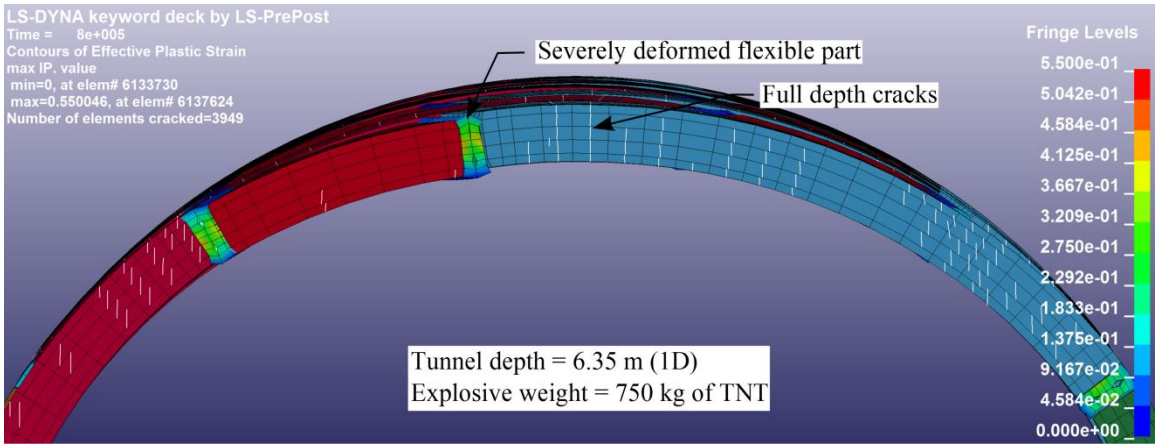

(b) Deformed shape of the tunnel buried in 1D depth for load case 3

Figure 7.14: Tunnel deformation after 300 ms of the explosion for different load cases

7.3.5 Introducing a reinforced concrete buster slab above the tunnel crown.

This is an external blast mitigation measure combating the shockwave before reaching the tunnel structures. This method can be applied to both a newly designed tunnel and to blast retrofitting of existing tunnel structures. In this method, a reinforced concrete slab (buster slab) was buried between the tunnel crown and the ground surface and at the exact center of the tunnel as shown in Figure 7.15(a). The buster slab was 8.5 m width, 14.0m long and

90cm thick and reinforcement details are shown in Figure 7.15(b). The same concrete strength grade as used for producing the segments was used to make the buster slab.

In this modelling, the interaction between the soil and the buster slab was modelled using CONTACT_AUTOMATIC_ SURFACE_TO_ SURFACE type contact which allowed the sliding and separation at the contact interface.

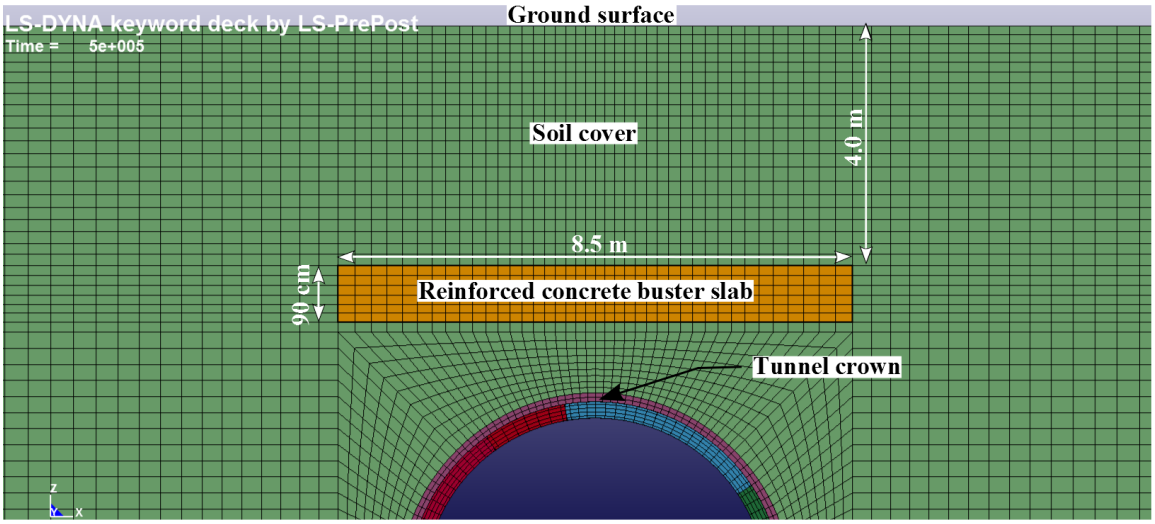

(a) Incorporated buster slab model

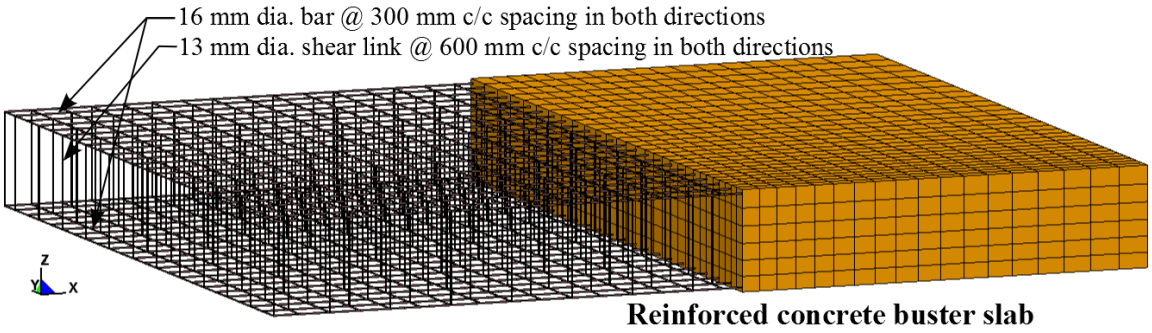

(b) Reinforced concrete buster slab model

Figure 7.15: Numerical models

Figure 7.16 illustrates the shockwave interaction with the buster slab for a situation, in which the tunnel depth and the explosive weight were 6.35m (1D) and 250kg of TNT respectively. Following the impact of a shockwave on the buster slab, a significant amount of the shockwave refraction occurred beneath the slab as shown in Figure 7.16(b).

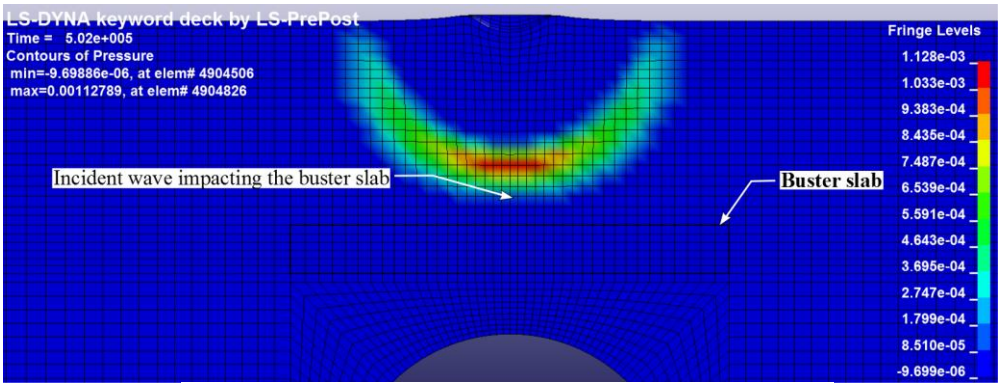

(a) Shockwave after 2ms of explosion

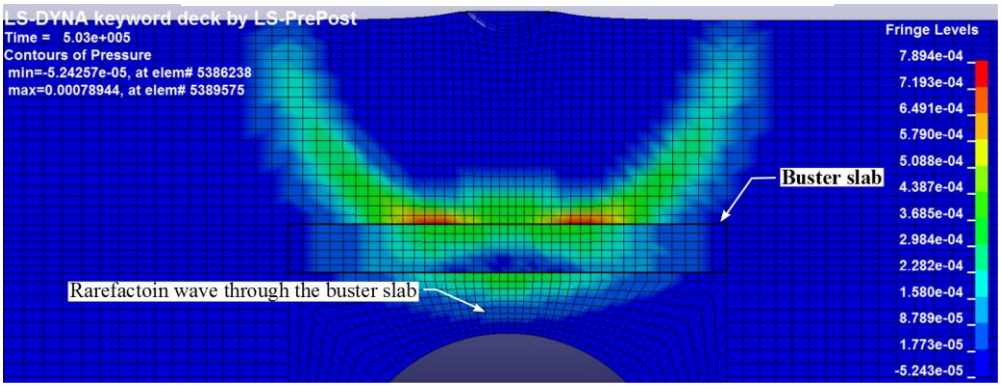

(b) Shockwave after 3ms of explosion

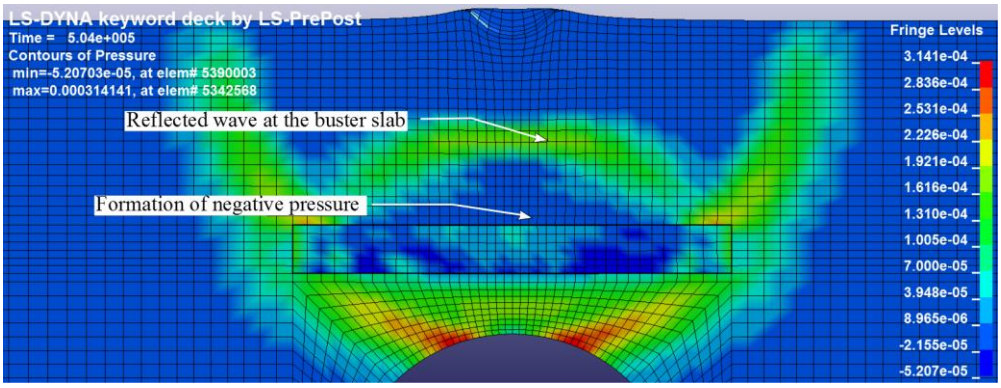

(c) Shockwave after 4ms of explosion

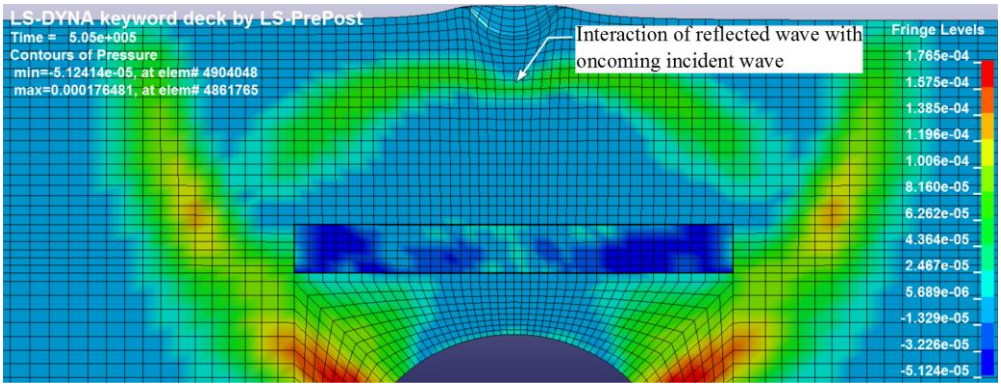

(d) Shockwave after 5ms of explosion

Figure 7.16: Shockwave propagation through the buster slab-Depth= 1D & Load case 1

As displayed in Figure 7.16(c), a reflection of incident shockwave at the slab surface caused considerable negative pressure in the soil above the top of the buster slab. As a result, a slight gap remained between the soil and the slab. Besides the small gap opening, the slab moved with the soil due to the soil confinement. The reflected wave interacted with oncoming incident wave disturbing the spherical pattern of the reflected wave near to the crater which is shown in Figure 7.16(d). Overall, the buster slab significantly reduced the intensity of the shockwave striking the tunnel through a series of reflections and rarefaction of the shockwave.

The blast influence diagram is shown in Figure 7.17. This mitigation approach shows a significant improvement in all the damage zones. Expansion of no damage zone illustrates that the shallow buried tunnel with the soil cover of 6.35m can resist up to 250kg of TNT without critical damages. The same tunnel can even resist up to 750kg of TNT with moderate damages. The introduction of the buster slab has dramatically reduced the negative pressure around the tunnel crown whereas, in the conventional tunnel without the buster slab (for 750kg of TNT), segments moved relative to each other and left extreme offsets between segments due to the present of negative pressure. Even in the severe damage zone, maximum crack widths and number of bolt failures were significantly reduced compared to the conventional tunnel without the buster slab.

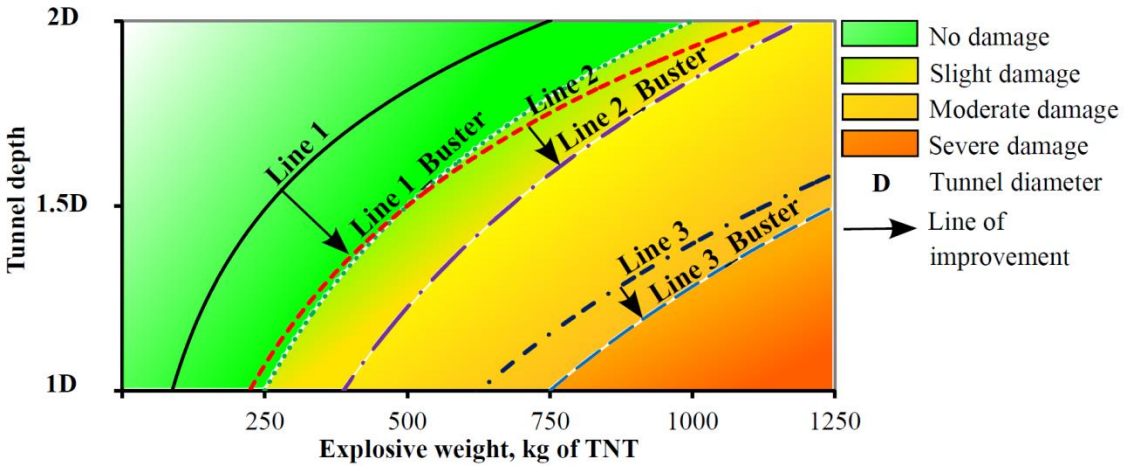

Figure 7.17: Critical explosive weight vs. tunnel depth for buster slab introduction

7.4 DISCUSSION OF NUMERICAL RESULTS

The analysis was further extended to predict the blast response of the segmented tunnel to different scale distances by varying the tunnel depth as well as the ground distance of explosive from the tunnel centreline. The tunnel was considered as buried in saturated soil.

Four damage categories for the segmented tunnel lining subjected to surface blast were investigated, such as no damage, slight damage, moderate damage and severe damage. The numerical results mathematically transformed to the critical lines to represent the critical explosive weight versus the stand-off distance relationships corresponding to the four damage states. It is clear that the tunnel depth as well as the ground distance of the explosive from the tunnel centreline have significant influence on the damage levels of tunnel response. The obtained analytical curves allow a quick and simple assessment of the vulnerability of buried tunnels subjected to surface blast. Comparison of critical lines for an identical scale distances illustrates that the tunnel lining is vulnerable to surface explosions which occurred directly above the centre of the tunnel than those that occurred at any equivalent scale distances by moving the explosive away from the tunnel centre on the ground. For the tunnel considered in this study, the safe explosive weight to resist the explosion that occurred directly above the centre of the tunnel are recommended: if a tunnel is buried at a depth of 6.35m, the safe explosive weight to avoid severe damage should be a maximum of 625kg of TNT, whereas for a depth of 9.52m, the safe explosive weight is 1125kg of TNT which is almost double. Providing a safety zone (a distance of 6.35m on either side of the tunnel centreline) on the ground will protect the shallow buried tunnel from severe damage from up to 1125kg of TNT explosive.

Different blast mitigation measures were included in this study to decrease the vulnerability by adopting prevention and mitigation measures to reduce the structural damage and to increase the coping capacity. Five mitigation approaches are discussed in this study as follows:

7.4.1 Wrapping the tunnel with a flexible and compressible barrier consisting of a layer of polyurethane foam.

A compressible porous barrier consisting of a layer of polyurethane foam was used to fill the circular annular gap between the bored soil face and the lining. Energy absorption capability of the polyurethane layer significantly reduced the tunnel damage in terms of cracks and bolt failure. The first two critical lines were moved to the right side of a higher order of explosive range. For the tunnel considered in this study, the following improvements are suggested: if a tunnel depth is 6.35m, it can resist up to 500kg of TNT with slight damage, whereas the conventional tunnel can resist only up to 230kg of TNT. The tunnels did not show any improvement for high-energy blast impact. As a result, the severe damage zone remained unchanged. In this zone, the immediate ring in the tunnel lining has attracted more blast load as the polyurethane layer is less stiff to distribute the blast load to its neighbouring rings.

7.4.2 Wrapping the tunnel with a secondary in-situ reinforced concrete lining

The annular gap was filled with a secondary reinforced concrete lining to protect the primary segmented lining. This barrier provides a passive blast protection by allowing the secondary lining to crack and reflecting the shockwave. It also helped to redistribute the blast load to its neighbouring rings. This approach significantly improved the blast performances against low-energy blast impact. For example, if a tunnel depth is 6.35m, it can resist up to 240kg of TNT with no damage, whereas the conventional tunnel can resist only up to 85kg of TNT. However, there was no significant difference in high-energy blast impact since the severe damage zone remained unchanged. It should be noted that the secondary lining approach is more expensive and time consuming than the spraying the concrete grout. Since the annular gap (the thickness is 150mm in this study) is comparatively smaller than the lining thickness, the capping may not be sufficient to resist the blast induced bending stresses. Increasing the annular gap may not be feasible with the conventional TBM.

7.4.3 Replacing Reinforced Concrete (RC) segments by Steel Fibre Reinforced Concrete (SFRC) segments.

The tunnel lining was constructed using Steel Fibre Reinforced Concrete (SFRC) segments without reinforced bars. After the explosion, the segments were free from major cracks due to high specific facture energy than in the conventional reinforced concrete (RC). It was observed that, for low-energy blast impact, SFRC lining displayed a small number of radial bolt failures compared to the conventional RC lining. As a result, the first two critical lines were significantly moved to right side, resulting significant reduction in the tunnel damage than that of previous mitigation measures such as wrapping the tunnel with polyurethane foam and secondary RC layers. However, for high-energy blast impact, SFRC lining is not very effective as it has reduced flexural strength compared to the conventional RC. This resulted in a large number of both radial and circumferential bolt failures. It is suggested that increasing the number of segments in a ring may help to increase the flexibility of SFRC segments.

7.4.4 Introducing energy absorbing, flexible honeycomb elements between radial joints.

Honeycomb flexible (compressible) cell elements were introduced between the radial joints in order to allow the segments to expand along the circumference and rotate about the joints. Under low-energy blast impact, crushing of flexible elements has significantly delayed the commencement of crack formation in the segments as well as the reduced number of bolt failures compared to the conventional segmented lining. As a result, a tunnel buried at 9.52m showed there was a significant rise in its no damage resistance from 250kg to 375kg of TNT. For high-energy blast impact, both the flexible elements and the segments deformed simultaneously and displayed no improvement in the crack response. However, deformation of flexible elements in the radial direction considerably minimised the number of radial bolt failures. By considering the additional costs associated with introducing the flexible elements, it seems that it is not worth in terms of overall improvement in the blast performance of the tunnel considered in this study.

7.4.5 Introducing a reinforced concrete buster slab above the tunnel crown.

Introduction of a buster slab expressively reduced the vulnerability of the tunnel response to the surface explosion. The buster slab interrupted and combated the shockwave on its way to the target. After reflection of the shockwave, a significant amount of rarefaction of the shockwave transmitted through the buster slab and interacted with the tunnel structure.
As the intensity of the shockwave has significantly reduced, the tunnel displayed huge improvement in overall blast performance. Movement of all the critical lines to the right enlarged the area of no damage zone as well as diminished the other damage zones. Overall, this method is very effective in mitigating blast effects on the tunnel as it can be applied to a newly designed tunnel and to blast retrofitting of exiting tunnel as well.

7.5 CHAPTER SUMMARY

In this chapter, a parametric study was considered by varying the tunnel depth as well as the ground distance of explosive from the tunnel centerline. The tunnel was considered as buried in the saturated soil. The study showed that the tunnel lining is vulnerable to surface explosions which occurred directly above the centre of the tunnel than those that occurred at any equivalent scale distances by moving the explosive away from the tunnel centre on the ground. The finding from the parametric study was further extended to mitigate the blast effects by introducing different mitigation strategies. The main findings of this study are as follows:

1. When a tunnel is subjected to a surface explosion, the tunnel depth as well as the ground distance of the explosive from the tunnel centreline have a significant influence on tunnel response.

2. If a tunnel is buried at a depth of 6.35m, the safe explosive weight to avoid severe damage should be less than 625kg of TNT, whereas for a depth of 9.52m, the safe explosive weight is 1125kg of TNT which is almost double.

3. Providing a safety zone (a distance of 6.35m on either side of the tunnel centreline) on the ground will protect the shallow buried tunnel from severe damage from up to 1125kg of TNT explosive.

4. For low-energy blast impacts, a strategy of wrapping the tunnel with a flexible and compressible barrier consisting of a layer of polyurethane foam significantly reduced the tunnel damage. For example, if the depth of a wrapped tunnel is 6.35m, it can resist up to 500kg of TNT with slight damage, whereas the conventional tunnel can resist only up to 230kg of TNT. The lack of load redistribution capability of the polyurethane did not make any difference in high-energy blast impacts. As a result, the severe damage zone remained unchanged.

5. An approach of wrapping the tunnel with a secondary reinforced concrete lining offered a significant improvement for low-energy blast impact due to its passive blast resistance as well greater redistribution ability. For example, if the tunnel depth is 6.35m, the wrapped tunnel can resist up to 240kg of TNT with no damage, whereas the conventional tunnel can resist only up to 85kg of TNT. For high-energy blast impacts, there was no change in the severe damage zone.

6. Replacing the conventional reinforced concrete segments by steel fibre reinforced concrete (SFRC) segments has a significant impact on the blast response. As a result of improved crack response and reduction in the number of bolt failures, upper boundaries of both no damage and slight damage zones displayed a significant expansion towards higher blast level. For example, if the tunnel depth is 9.52m, it can resist up to 875kg of TNT with slight damage, whereas the conventional tunnel can resist only up to 500kg of TNT. However, for high-energy blast impact, SFRC lining displayed stiff behaviour as SFRC has reduced flexural strength compared to the conventional RC. As a result, the severe damage zone remained unchanged.

7. As a result of the introduction of honeycomb flexible (compressible) cell elements between the radial joints, crack formations in the segments were delayed and the numbers of radial bolt failures were reduced for low-energy blast impacts compared to the conventional segmented lining. For example, the tunnel buried at 9.52m showed there was a significant rise in its no damage resistance from 250kg to 375kg of TNT. For high-energy blast impacts, there was no difference in terms of crack response. Hence the severe damage zone has an insignificant effect.

8. Introduction of a buster slab expressively improved the blast performance of the tunnel in terms of crack formation, number of bolt failure and drifting between segments. Unlike other approaches mentioned above, this approach significantly influenced the tunnel response from low to high energy blast impacts as the buster slab considerably reduced the intensity of shockwave transmission. For example, if the tunnel is buried at a depth of 6.35m, the safe explosive weight to avoid severe damage is at 750kg of TNT, whereas the conventional tunnel can resist only up to 625kg of TNT.

Chapter 8: Conclusion and Recommendations

8.1 REVIEW OF RESEARCH WORK

The principal objectives of this thesis were to investigate the performance of segmented bored tunnels subjected to surface blast loads, and to study the behaviour of joints in the segmented tunnel. This research developed and applied fully coupled numerical techniques incorporating Fluid Structure Interaction (FSI) to accurately predict the dynamic response of segmented tunnels to blast loads using an advanced general purpose multi-physics simulation software LS-DYNA. Throughout the thesis, the aim has been accomplished.

Two different numerical techniques (i) coupled FSI in ALE and (ii) coupled SPH-FE techniques were considered for treating the response of buried tunnels subjected to surface blast loads. In the coupled FSI in ALE, eight-node solid elements were used with different spatial discretisation solvers. Lagrangian meshes were used to model the soil and the tunnel while Eulerian meshes were used separately to model the surrounding air and explosive. In the coupled SPH-FE, the portion of soil experiencing large deformations and the explosive were modelled with SPH particles while the rest of the geometry was modelled with Lagrangian meshes. The surrounding outside space of the explosive was assumed to be a vacuum. The reinforced concrete segments were modelled using eight-node solid Lagrangian elements. The reinforcement steel and bolts were modelled using Hughes-Liu beam elements with cross sectional integration. The reinforcing beam elements and bolts were modelled as discrete elements immersed in the segment meshes using Constrained_Lagrangian_In_Solid coupling.

The modelling techniques were validated using previous experimental records. Based on the comparison of the two techniques in terms of computational efficiency and accuracy, it was found that the coupled FSI in ALE technique outweighed the coupled SPH-FE technique to treat surface blast loads. To achieve the basic objectives, a parametric study was performed to observe the behaviour of the segmented tunnels of

various segment geometries, different joint types and number of segments forming the tunnel ring. Three types of soil: saturated, partially saturated and dry soils were considered in order to investigate the effect of soil properties on the blast response of a buried tunnel.

A second phase of the research consisted of investigating the effect of stand-off distances by varying the tunnel depth as well as the ground distance of the explosive from the tunnel centreline. Four damage categories of the tunnel lining subjected to a surface blast were investigated, such as no damage, slight damage, moderate damage and severe damage. In order to improve damage performance and to decrease the vulnerability of the tunnel, five different blast mitigation measures were illustrated.

8.2 MAIN FINDINGS OF THIS RESEARCH AND RECOMENDATIONS

The main findings of this research are presented below:

This research developed and applied two different numerical modelling techniques (i) coupled FSI in ALE and (ii) coupled SPH-FE for treating the blast response of buried tunnels subjected to surface blast. Comparison of the two techniques using results from a centrifuge test (De, 2012) shows that the coupled FSI in ALE technique outweighed the coupled SPH-FE technique in terms of accuracy and computational efficiency. This provides confidence in the coupled FSI in ALE modelling technique for predicting the response of segmented bored tunnels subjected to surface blast.

The validated numerical technique was then extended to study the effects of the geometric shapes of the segments on the blast response of the tunnel. Hexagonal segments (HS) significantly reduced the drifting between the tunnel rings, but they suffered severe in-plane drifting within the ring. Interlocking segments (IS) also suffered from the drifting between rings as well as in-plane drifting. Though the tunnel with rectangular segments (RS) displayed considerable drifting between the rings, in-plane drifting was insignificant because of increased flexibility due to the orientation of radial joints.

The blast response of buried tunnel in saturated soil is more severe in terms of crack formation and bolt failures than the tunnel buried in either partially saturated soil or dry

soil when subjected to the same surface explosion. In all soil conditions, the diametric distortions increase with the explosive mass and the distortions are unrecoverable in all load cases (from 250 to 1250kg of TNT) treated in this study. As the explosive mass increased to more than 750kg of TNT, the tunnel buried in the saturated soil displayed segment-disintegration from neighbouring segments. For weaker blast loads (250kg of TNT), joint types influenced the tunnel response by allowing the segments to rotate about the joints, whereas for higher blast loads, the segments were damaged before triggering the flexibility of the joints. While the flat joints were effective in transferring hoop stress at the joints, convex-convex joints resulted in less number of bolt failures and significant improvement in the crack response for weaker blast loading.

As the number of segments increased in a ring, the maximum crack width decreased. However, as the number of segments further increased to seven segments (six segments plus a key segment) in a ring, it did not make much difference in the magnitude of the maximum crack width. Although the tunnel with seven segments in a ring displayed less number of radial bolt failures, the numbers of circumferential bolt failures were significantly higher than the tunnel with six segments (five segments plus a key segment) in a ring.

When a tunnel is subjected to a surface explosion, the tunnel depth as well as the ground distance of the explosive from the tunnel centreline have a significant influence on tunnel response. If a tunnel is buried at a depth of 6.35m, the safe explosive weight to avoid severe damage should be less than 625kg of TNT, whereas for a depth of 9.52m, the safe explosive weight is 1125kg of TNT which is almost double. Providing a safety zone (a distance of 6.35m on either side of the tunnel centreline) on the ground will protect the shallow buried tunnel from severe damage from up to 1125kg of TNT explosive.

This research also provides recommendations for blast mitigation of the segmental tunnels subjected to surface explosion. For low-energy blast impact, a strategy of wrapping the tunnel with a flexible and compressible barrier consisting of a layer of polyurethane foam significantly reduced the tunnel damage. For example, if the depth of a wrapped tunnel is 6.35m, it can resist up to 500kg of TNT with slight damage,

whereas the conventional tunnel can resist only up to 230kg of TNT. The lack of load redistribution capability of the polyurethane did not make any difference in the severe damage zone which remained unchanged in the damage influence diagram.

An approach of wrapping the tunnel with a secondary reinforced concrete lining offered a significant improvement for low-energy blast impacts due to its passive blast resistance as well greater load redistribution ability. For example, if a tunnel depth is 6.35m, a wrapped tunnel can resist up to 240kg of TNT with no damage, whereas the conventional tunnel can resist only up to 85kg of TNT. For high-energy blast impacts, there was no change in the severe damage zone.

Replacing the conventional reinforced concrete segments by steel fibre reinforced concrete (SFRC) segments has a significant impact on the blast response. As a result of improved crack response and reduction in the number of bolt failures, upper boundaries of both no damage and slight damage zones showed a significant expansion towards higher blast level. For example, if the tunnel depth is 9.52m, this type of tunnel can resist up to 875kg of TNT with slight damage, whereas the conventional tunnel can resist only up to 500kg of TNT. However, for high-energy blast impacts, SFRC lining displayed stiff behaviour as SFRC has reduced flexural strength compared to the conventional RC. As a result, the severe damage zone remained unchanged.

As a result of the introduction of Honeycomb flexible (compressible) cell elements between the radial joints, crack formations in the segments were delayed and the numbers of radial bolt failures were reduced for low-energy blast impacts compared to the conventional segmented lining. For example, the tunnel buried at 9.52m showed there was a significant rise in its no damage resistance from 250kg to 375kg of TNT. For high-energy blast impacts, there was no difference in terms of crack response. Hence the severe damage zone has an insignificant effect.

Introduction of a buster slab expressively improved the blast performance of the tunnel in terms of crack formation, number of bolt failure and drifting between segments. Unlike other approaches as mentioned above, this approach significantly influenced the tunnel response from low to high energy blast impacts as the buster slab considerably

reduced the intensity of shockwave transmission. For example, if the tunnel is buried at a depth of 6.35m, the safe explosive weight to avoid severe damage is at 750kg of TNT, whereas the conventional tunnel can resist only up to 625kg of TNT.

Based on the present study of the response of the segmented tunnel subjected to surface blast loads, it can be concluded that the present modelling techniques and research findings can serve as a benchmark reference in future development in this research area and in the verification and validation of numerical models. This study also made an effort to provide a confidence level for mitigating the blast effects on the tunnel response.

8.3 FUTURE RESEARCH

From the experience gained in this numerical research study the following recommendations are made for future studies in this area:

- Numerical simulation of a tunnel buried in a layered soil profile is recommended for future studies in order to simulate real field conditions. In the present study, the soil is considered as a homogeneous single layered soil.

- The present research did not consider the bolt holes in the segments as it is numerically more expensive. The bolts were modelled as discrete elements coupled to the solid elements of the segments throughout its length. A detailed numerical study is required in order to evaluate and verify the influence of bolt holes in the segments under blast loads.

- Due to the limitation in the non-reflecting boundaries, surcharge loads from moving vehicle and super imposed dead loads from aboveground structures are not considered in the present modelling. Therefore, further research is required to include those loads to simulate the real the conditions.

- In the present thesis, small diameter single tube railway tunnels were considered to investigate the blast effects. However, there are many large diameter segmented tunnels which need to be investigated.

- Some of the blast mitigation measures considered in this study are expensive. Since soils are capable of absorbing blast energy, extensive research should be conducted in future studies for mitigating the blast effects on the tunnels by introducing appropriate backfilling materials to cover the top ground surface of the tunnels.

References

Abbo, A. J., & Sloan, S. W. (1995). *A smooth hyperbolic approximation to the Mohr-Coulomb yield criterion*. Computers & Structures, 54(3), 427-441. doi: http://dx.doi.org/10.1016/0045-7949(94)00339-5

Ågårdh, L. (1997). *Fe-Modeling of Fibre Reinforced Concrete Slabs Subjected to Blast Load*. J. Phys. IV France, 07(C3), C3-723-C723-728.

Alia, A., & Souli, M. (2006). *High explosive simulation using multi-material formulations*. Applied Thermal Engineering, 26(10), 1032-1042. doi: http://dx.doi.org/10.1016/j.applthermaleng.2005.10.018

Ambrosini, D., Luccioni, B., & Danesi, R. (2004). *Influence of the soil properties on craters produced by explosions on the soil surface*. Computational Mechanics, XXIII, 571-590.

Ambrosini, R. D., & Luccioni, B. M. (2005). *Craters Produced by Explosions on the Soil Surface*. Journal of Applied Mechanics, 73(6), 890-900. doi: 10.1115/1.2173283

Arulmoli, K., VELACS Project, Earth Technology Corporation, National Science Foundation (U.S.) (1992). *VELACS Verification of Liquefaction Analyses by Centrifuge Studies Laboratory Testing Program: Soil Data Report*. Earth Technology Corporation.

Bahei-El-Din, Y. A., & Dvorak, G. J. (2007). *Behavior of Sandwich Plates Reinforced with Polyurethane/Polyurea Interlayers under Blast Load*. Journal of Sandwich Structures and Materials, 9, 261-281.

Baylor, J. T. (1992). *Parameters Affecting Loads on Buried Structures Subjected to Localized Blast Effects*: Army Engineer Waterways Experiment Station Vicksburg Ms Structures Lab.

Beňo, J., & Hilar, M. (2013). *Steel Fibre Reinforced Concrete for Tunnel Lining-Verification by Extensive Laboratory Testing and Numerical Modelling*. Acta Polytechnica Journal of Advanced Engineering, 53(4), 329-337.

Bessette, G. C. (2004). *Modeling Coupled Blast/Structure Interaction with Zapotec, Benchmark Calculations for the Conventional Weapon Effects Backfill (CONWEB) Tests*: Sandia National Laboratories Report SAND20044096.

Blatz, P. J., & Ko, W. L. (1962). *Application of Finite Elastic Theory to the Deformation of Rubbery Materials*. Transactions of the Society of Rheology., VI, 223-251.

Bull, J. W., & Woodford, C. H. (1998). *Camouflets and their effect on runway support.* Computers & Structures, 69(6), 695-706. doi: http://dx.doi.org/10.1016/S0045-7949(98)00135-7

Conterterrorism 2014 Calendar (2014), *Bomb Threat Stand-off Distances*. Retrieved March 2014, from http://www.nctc.gov/site/technical/bomb_threat.html

Cooper, P. W., & Kurowski, S. R. (1996). *Introduction to the Technology of Explosives*: VCH.

Darwin, D., Barham, S., Kozul, R., & Luan, S. (2001). *Fracture energy of high-strength concrete*. ACI Materials Journal, 98(5).

Davies, M. C. R. (1994). *Dynamic Soil Structure Interaction Resulting from Blast Loading.* Paper presented at the Centrifuge 94. Rotterdam:Balkema.

Davies, M. C. R., & Williams, A. J. (1992). *Centrifuge Modelling the Protection of Buried Structures Subjected to Blast Loading*. Structures Under Shock and Impact II, 663-674.

De, A. (2012). *Numerical simulation of surface explosions over dry, cohesionless soil*. Computers and Geotechnics, 43(0), 72-79. doi: http://dx.doi.org/10.1016/j.compgeo.2012.02.007

De, A., Morgante, A. N., & Zimmie, T. F. (2013). *Mitigation of Blast Effects on Underground Structure Using Compressible Porous Foam Barriers*. Paper presented at the Poromechanics V. http://ascelibrary.org/doi/abs/10.1061/9780784412992.116

De, A., & Zimmie, T. F. (2011). *Modeling of Surface Blast Effects on Underground Structures*. Paper presented at the Geo-Frontiers Congress.

Department of the Army (1986). *Fundamental of Protection Design for Conventional Weapons*, TM5-855-1, US Army Engineers Waterways Experimental Stations, Vicksburg.

Engineering Group (2010). *Civil Design Criteria for Road and Rail Transit Systems*, Land Transport Authority, Singapore.

Feldgun, V. R., Kochetkov, A. V., Karinski, Y. S., & Yankelevsky, D. Z. (2008). *Internal blast loading in a buried lined tunnel*. International Journal of Impact Engineering, 35, 172 - 183.

Gingold, R. A., & Monaghan, J. J. (1977). *Smoothed particle hydrodynamics-theory and application to non-spherical stars*. Monthly Notices of the Royal Astronomical Society, 181, 375-389.

Glasstone, S., & Dolan, P. J. (1977). *The Effects of Nuclear Weapons* (3 ed.): United States Department of Defense and the Energy Research and Development Administration.

Gui, M., & Chien, M. (2006). *Blast-resistant Analysis for a Tunnel Passing Beneath Taipei Shongsan Airport–a Parametric Study*. Geotechnical and Geological Engineering, 24(2), 227-248.

Hallquist, J. O. (2006). *LS-DYNA THEORY MANUAL*, Livermore Software Technology Corporation(LSTC). California, USA.

Hayes, P. G. (1989). *Backfill Effects on Response of Buried Reinforced Concrete Slabs*. Vicksburg, Mississippi: Waterways Experiment Station, Corps of Engineers.

Higgins, W., Chakraborty, T., & Basu, D. (2012). *A high strain-rate constitutive model for sand and its application in finite-element analysis of tunnels subjected to blast*. International Journal for Numerical and Analytical Methods in Geomechanics (2012).

Higgins, W. T. (2011). *Development of a high strain-rate constitutive model for sands and its application in finite element analysis of tunnels subjected to blast.* (M.S. thesis), University of Connecticut, Storrs, Connecticut, USA.

Jayasinghe, L. B., Thambiratnam, D. P., Perera, N., & Jayasooriya, J. H. A. R. (2013). *Computer simulation of underground blast response of pile in saturated soil*. Computers & Structures, 120(0), 86 - 95.

Jayasinghe, L. B., Thambiratnam, D. P., Perera, N., & Jayasooriya, J. H. A. R. (2014). *Effect of soil properties on the response of pile to underground explosion*. IABSE, Structural Engineering International Journal, (in press).

Jayasooriya, Ruwan, David P. Thambiratnam, Nimal J. Perera and Vladis Kosse. 2011. *Blast and residual capacity analysis of reinforced concrete framed buildings*. Engineering Structures 33 (12): 3483-3495.

Joint Departments of the Army, the Navy and the Air Force (1990). *Structures to Resist the Effect of Accidental Explosions*, TM5-1300/NA VFAC P-397/AFR 88-22.

Kinney, G.F. and Graham, K.J. (1985). *Explosive shocks in air (2nd edition)*. Springer-Verlag, 282pp.

Kramer, S. L. (1996). *Geotechnical Earthquake Engineering*. USA: Prentice-Hall.

Krauthammer, T., & Chen, Y. (1989). *Soil-structure interface effects on dynamic interaction analysis of reinforced concrete lifelines*. Soil Dynamics and Earthquake Engineering, 8(1), 32-42.

Kutter, B. L., O'Leary, L. M., & Thompson, P. Y. (1988). *Gravity-Scaled Tests on Blast-Induced Soil-Structure Interaction*. Journal of Geotechnical Engineering,, 114, 431-447.

Laine, L., & Sandvik, A. (2001). *Derivation of Mechanical properties for sand. Proceedings of the 4th Asia-Pacific Conference on Shock and Impact Loads on Structures*, CI-Premier PTE LTD, Singapore, 361-368.

Lee, W. Y. (2006). *Numerical modeling of blast-induced liquefaction.* (doctoral dissertation), Department of Civil and Environmental Engineering, Brigham Young University, USA.

Lewis, B. A. (2004). *Manual for LS-DYNA Soil Material Model 147*. Federal Highway Administration, McLEAN, VA.

Liu, H. (2009). *Dynamic Analysis of Subway Structures Under Blast Loading*. Geotechnical and Geological Engineering, 27(6), 699-711.

Liu, H. (2012). *Soil-Structure Interaction and Failure of Cast-Iron Subway Tunnels Subjected to Medium Internal Blast Loading*. Journal of Performance of Constructed Facilities, Vol. 26, 691-701.

Livermore Software Technology Corporation, LSTC (2007). *LS-DYNA Keyword User's Manual v971*. California, USA.

Luccioni, B., Ambrosini, D., Nurick, G., & Snyman, I. (2009). *Craters produced by underground explosions*. Computers & Structures, 87(21-22), 1366-1373.

Lucy, L. (1977). *A numerical approach to the testing of the fission hypothesis*. The Astronomical Journal, 82, 1013-1024.

Malvar, L. J., & Crawford, J. E. (August 1998). *Dynamic Increase Factors for Concrete*. Paper presented at the Twenty-Eight DDESB Seminar, Orlando, FL,.

Matuska, D. A. (1984). *HULL Users' Manual*. Air Force Armament Laboratory, Florida, USA: Orlando Technology, Incorporated, Florida, USA.

McMaster, W., H. (1984). *Computer codes for fluid-structure interactions*. American Society of Mechanical Engineers.

Monaghan, J. J. (1992). *Smoothed particle hydrodynamics*. Annual review of astronomy and astrophysics, 30, 543-574.

Monaghan, J. J. (1994). *Simulating Free Surface Flows with SPH*. Journal of Computational Physics, 110(2), 399-406. doi: http://dx.doi.org/10.1006/jcph.1994.1034

Morris, J.P., M.B. Rubin, S.C. Blair, L.A. Glenn and F.E. Heuze. (2004). *Simulations of underground structures subjected to dynamic loading using the distinct element method*. Engineering Computations 21 (2/3/4): 384-408.

Muir Wood, A. M. (1975). *The circular tunnel in elastic ground*. Geotechnique, 25(1), 115 – 127.

Munfah, N. (2009). *Safety and Security of Tunnels and Underground Transportation Facilities*. Parsons Brinckerhoff, National Tunnelling Practice Leader, New York, U.S.A.

Naesgaard, E., Byrne, P., M, & Wijewickreme, D. (2007). *Is P-wave velocity an indicator of saturation in sand with viscous pore fluid?* International Journal of Geomechanics, 7(6), 437-443.

Olarewaju, A. J. (2012a). *Study on the Impact of Varying Degrees of Underground Accidental Explosions on Underground Pipes by Simulation*. Earth Science Research, Published by Canadian Centre of Science and Education, Vol.1, No. 2, 189-199. doi: 10.5539/esr.v1n2p189

Olarewaju, A. J. (2012b). Effect of Loose Sand and Dense Sand on the Response of Underground Empty Pipes due to Accidental Explosions. *Electronic Journal of Geotechnical Engineering (EJGE), Vol. 17 Bundle G*, 879-891.

Olarewaju, A. J. (2013). *Prediction and Assessment of Loads from Various Accidental Explosions for Simulating the Response of Underground Structures using Finite Element Method*. Electronic Journal of Geotechnical Engineering (EJGE), Vol. 18 Bundle B, 375-396.

Oluokun, Francis A, Edwin G. Burdette, & Deatherage, J. H. (1991). *Young's modulus, Poisson's ratio and compressive strength relationships at early ages*. ACI Materials Journal, 88, 3-9.

Ortman, & Catherine, M. (2008). *The Effect of Diameter on Dynamic Seabed Penetration* (ADA486586 ed.): NAVAL ACADEMY ANNAPOLIS MD.

Ottosen, N. S. (1977). *A Failure Criterion for Concrete*. Journal of Engineering Mechanics Division, 103(4), 527-535.

Peroni, M., Peroni, L., & Dallocchio, A. (2009). Thermo-mechanical model identification of a strengthened copper with an inverse method *DYMAT 2009-9th International Conference on the Mechanical and Physical Behaviour of Materials under Dynamic Loading* (Vol. 2, pp. 1367-1373). France: EDP Sciences.

Procházka, P., P, Kravtsov, A., N, & Peskova, S. (2008). *Blast impact on structures of underground parking*: Wessex Institute of Technology, UK.

Saleh, M., & Edwards, L. (2011). *Application of a soil model in the numerical analysis of landmine interaction with protective structures* Paper presented at the 26th International symposium on blastics MIAMI.

Sandford, T. C. (2000). *Soil-Structre Interaction of buried strcutres* A2K04: Committeee on Subsurface Soil-Structure Interaction, Universtiy of Maine, U.S.A.

Schwer, L. (2011). *The Winfrith Concrete Model: Beauty or Beast? Insights into the Winfrith Concrete Model*. Paper presented at the 8th European LS-DYNA Users Conference, Strasbourg, France.

Shin, J. H., Moon, H. G., & Chae , S. E. (2011). *Effect of blast-induced vibration on existing tunnels in soft rocks*. Tunnelling and Underground Space Technology, 26(1), 51-61.

Sivalingam, K., Thambiratnam, D. P., & Gallage, C. (2014). *Performance of Buried Tunnels Subjected to Surface Blast Incorporating Fluid Structure Interaction*. ASCE Journal of Performance of Constructed Facilities. doi: doi:10.1061/(ASCE)CF.1943-5509.0000585

Skyscrapercity.com (2013). A cross-section of Moorgate Retrieved March 2013, from http://www.skyscrapercity.com/showthread.php?t=236257&page=168

Thiyahuddin, I., Gu, Y., & Thambiratnam, D. P. (2012). *A coupled SPH/FEM analysis of portable water filled barriers*. Paper presented at the 4th International Conference on Computational Methods (ICCM2012), Gold Coast, Qld.

Wang, J.N. (1993). *Seismic Design of Tunnels (A Simple State-of-the-Art Design Approach)*. Parsons Brinckerhoff Quade & Douglas, Inc., U.S.A.

Wang, J. (2001). *Simulation of Landmine Explosion Using LS-Dyna3d Software: Benchmark Work of Simulation of Explosion in Soil and Air*: DSTO Aeronautical and Maritime Research Laboratory.

Wang, Z., Hao, H., & Lu, Y. (2004). *A three-phase soil model for simulating stress wave propagation due to blast loading*. International Journal for Numerical and Analytical Methods in Geomechanics, 28(1), 33-56.

Wang, Z., Lu, Y., Hao, H., & Chong, K. (2005). *A full coupled numerical analysis approach for buried structures subjected to subsurface blast*. Computers & Structures, 83(4-5), 339-356.

Wen, D., Poh, J., & Ng, Y. W. (2004). *Design considerations for bored tunnels at close proximity*. Tunnelling and Underground Space Technology, 19(4–5), 468-469. doi: http://dx.doi.org/10.1016/j.tust.2004.02.072

Whittaker, J. P. (1987). *Centrifugal and numerical modeling of buried structures*. Volume 3. A centrifuge study of the behavior of buried conduits under airblast loads. Final report: Colorado Univ., Boulder (USA). Dept. of Civil, Environmental, and Architectural Engineering.

Xu, J.-x., & Liu, X.-l. (2008). *Analysis of structural response under blast loads using the coupled SPH-FEM approach*. Journal of Zhejiang University - Science A, 9(9), 1184-1192.

Yang, Y., Xie, X., & Wang, R. (2010). *Numerical simulation of dynamic response of operating metro tunnel induced by ground explosion*. Journal of Rock Mechanics and Geotechnical Engineering, 2(4), 373-384.

Yankelevsky, D. Z., Karinski, Y. S., & Feldgun, V. R. (2011). *Re-examination of the shock wave's peak pressure attenuation in soils*. International Journal of Impact Engineering, 38(11), 864 - 881.

Zhongqi, W., Yong, L., & Hong, H. (2004). *Numerical Investigation of Effects of Water Saturation on Blast Wave Propagation in Soil Mass*. Journal of Engineering Mechanics, 130(5), 551-561.

APPENDIX A

Controlled single concrete element simulation

This study uses a single element of a concrete, as shown in Figure A.1(a), to verify the output of crack width measurement and its unit in LS-DYNA which did not describe the unit of the crack width output in its technical manual. A consistent unit system is used in this study: mass (g), length (mm), time (ms), force (N) and stress (MPa). As described by Schwer (2011), a similar study is conducted with his material properties. The two parts of the element are allowed to move apart due to the prescribed displacement, as illustrated in Figure A.1(b). When the displacement exceeds the crack width (w) at failure of 0.127mm, the failure occurs on the element.

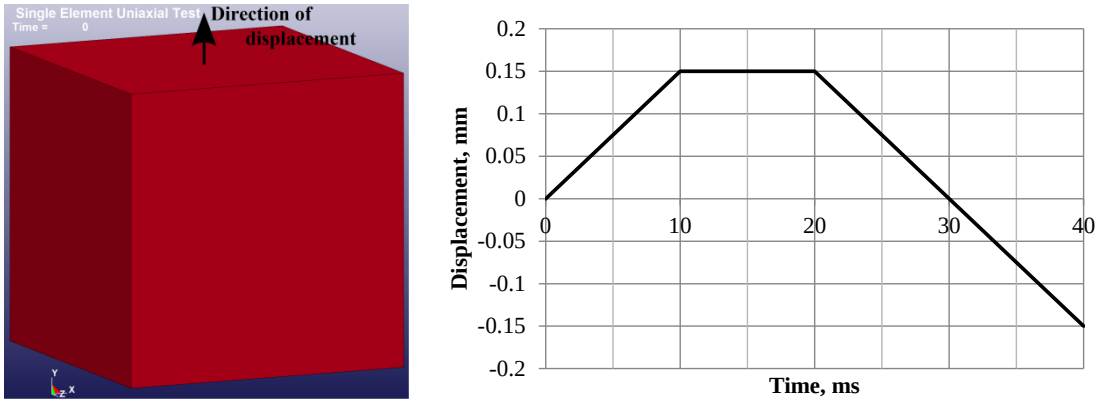

(a) A single solid element (b) Prescribed axial displacement (Schwer, 2011)

Figure A.1: A single element uniaxial test

Figure A.2 shows the simulation results. As the displacement increased in the tension portion, a single horizontal crack appeared perpendicular to the displacement in the element at 9.05ms and it satisfied the crack width displacement criterion, i.e. w = 0.127mm. As the displacement was reversed, closing of the horizontal crack occurred immediately after 30ms in the compression portion and it allowed to resist the compression. Consequently, two orthogonal cracks formed at 30.1ms when the element reached its unconfined compressive strength.

The maximum crack width of the first crack is consistent with unit system as both the prescribed displacement and the maximum crack width were nearly the same. The

orthogonal tensile crack width was very small in micrometres. This finding demonstrates that the crack width output unit in LS-Dyna is consistent with the adopted unit system. For example, if the input unit for the length is cm, the output crack width would be the same in cm.

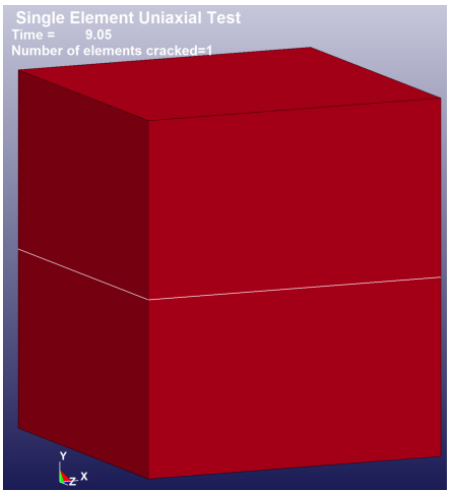

(a) Single tensile crack

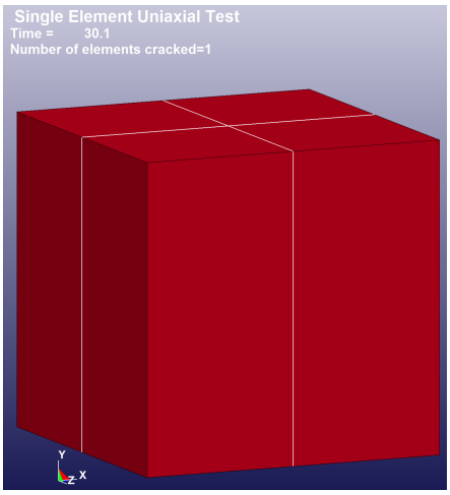

(b) Double orthogonal cracks

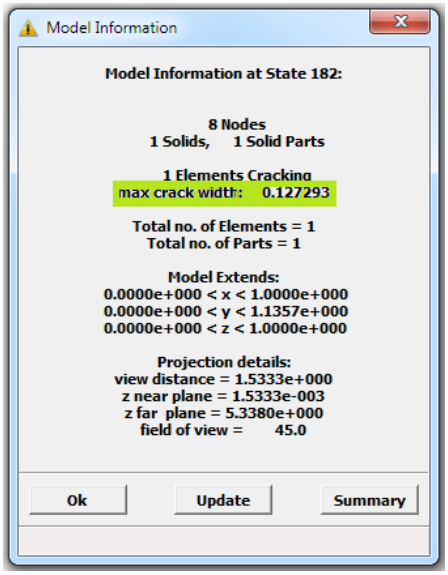

(d) The maximum crack width= 0.127mm

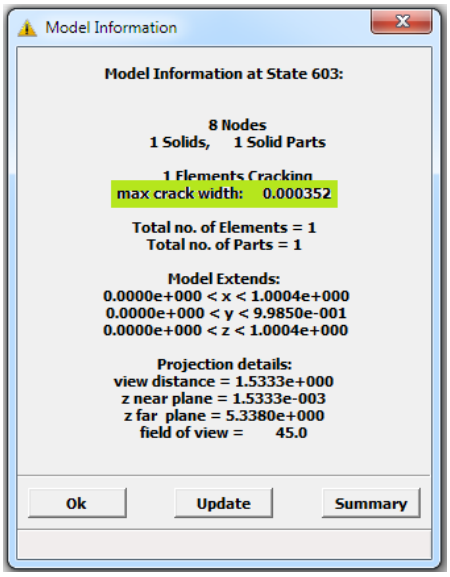

(c) The maximum crack width= 0.352μm

Figure A.2: Crack formations and corresponding maximum crack widths

APPENDIX B

Input parameters of concrete material model

B. 1 Concrete Grade 60

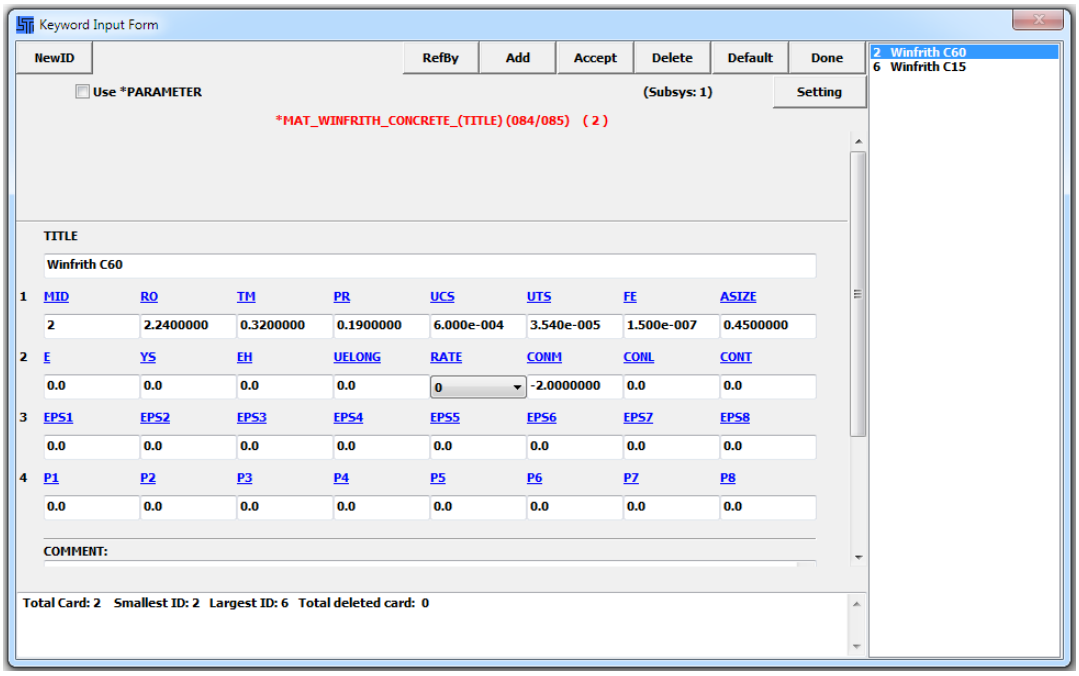

B. 2 Concrete Grade 15

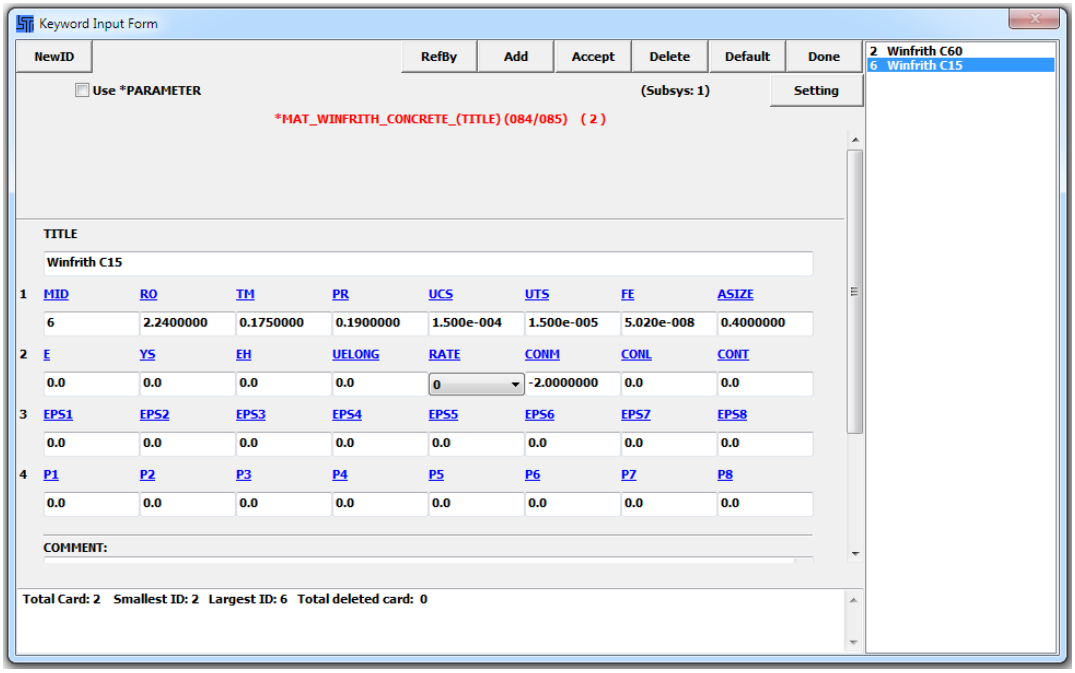

B. 3 Polyurethane foam

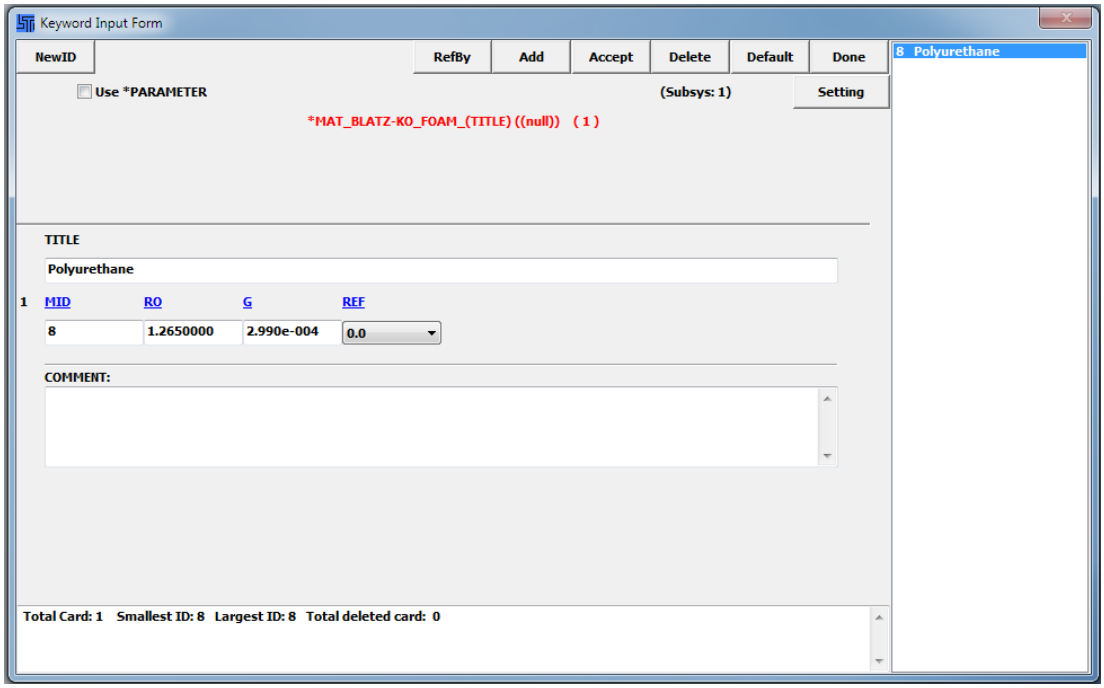

Unit system: Mass (g), Length (cm), Time (μs) and Stress (Mbar)